The Synthesis, Characteristics, and Application of Hierarchical Porous Materials in Carbon Dioxide Reduction Reactions

Guan, Ze Long; Wang, Yi Da; Wang, Zhao; Hong, Ying; Liu, Shu Lin; Luo, Hao Wen; Liu, Xian Lin; Su, Bao Lian

Published in:
Catalysts

DOI:
10.3390/catal14120936

Publication date:
2024

Document Version
Publisher's PDF, also known as Version of record

catalysts

MDPI

Review

The Synthesis, Characteristics, and Application of Hierarchical Porous Materials in Carbon Dioxide Reduction Reactions

Ze-Long Guan [1,†], Yi-Da Wang [1,†], Zhao Wang [1,*], Ying Hong [1], Shu-Lin Liu [1], Hao-Wen Luo [1], Xian-Lin Liu [1] and Bao-Lian Su [1,2]

[1] The State Key Laboratory of Advanced Technology for Material Synthesis and Processing, Wuhan University of Technology, Wuhan 430070, China; bao-lian.su@unamur.be (B.-L.S.)
[2] Laboratory of Inorganic Materials Chemistry (CMI), University of Namur, 61 Rue de Bruxelles, B-5000 Namur, Belgium
* Correspondence: zhao.wang@whut.edu.cn
† These authors contributed equally to this work.

Abstract: The reduction of carbon dioxide to valuable chemical products could favor the establishment of a sustainable carbon cycle, which has attracted much attention in recent years. Developing efficient catalysts plays a vital role in the carbon dioxide reduction reaction (CO_2RR) process, but with great challenges in achieving a uniform distribution of catalytic active sites and rapid mass transfer properties. Hierarchical porous materials with a porous hierarchy show great promise for application in CO_2RRs owing to the high specific surface area and superior porous connection. Plenty of breakthroughs in recent CO_2RR studies have been recently achieved regarding hierarchical porous materials, indicating that a summary of hierarchical porous materials for carbon dioxide reduction reactions is highly desired and significant. In this paper, we summarize the recent breakthroughs of hierarchical porous materials in CO_2RRs, including classical synthesis methods, advanced characterization technologies, and novel CO_2RR strategies. Moreover, by highlighting several significant works, the advantages of hierarchical porous materials for CO_2RRs are analyzed and revealed. Additionally, a perspective on hierarchical porous materials for CO_2RRs (e.g., challenges, potential catalysts, promising strategies, etc.) for future study is also presented. It can be anticipated that this comprehensive review will provide valuable insights for further developing efficient alternative hierarchical porous catalysts for CO_2 reduction reactions.

Keywords: CO_2RR; hierarchical porous materials; surfactant templating; supercritical fluid; catalytic hydrogenation; biomass carbon materials; electrochemistry

Citation: Guan, Z.-L.; Wang, Y.-D.; Wang, Z.; Hong, Y.; Liu, S.-L.; Luo, H.-W.; Liu, X.-L.; Su, B.-L. The Synthesis, Characteristics, and Application of Hierarchical Porous Materials in Carbon Dioxide Reduction Reactions. *Catalysts* **2024**, *14*, 936. https://doi.org/10.3390/catal14120936

Academic Editor: Ali Seifitokaldani

Received: 7 November 2024
Revised: 11 December 2024
Accepted: 14 December 2024
Published: 18 December 2024

1. Introduction

The excessive consumption of fossil fuels has contributed to a sharp rise in atmospheric CO_2 levels, leading to severe environmental issues [1]. The average concentration of atmospheric CO_2 has shown an extraordinary increase, ranging from 172 to 300 ppm before the latest industrial age to 405 ppm in 2021 [2]. Given the status of global warming, it is of vital importance to reduce atmospheric CO_2 levels [3].

The main industrial approaches to decrease CO_2 emissions can be divided into clean energy replacement, carbon capture–storage (CCS), and carbon capture and utilization (CCU) [4]. In particular, the industry is now trying to use clean energy, instead of the classical fossil energy, to reduce carbon emissions. Jiwei Zhou and his colleagues [5] achieved the application of 100% ammonia in ceramic roller kilns by implementing swirling combustion and gas-stage combustion technologies. The combustion efficiency of ammonia reached 99.99%, and the emissions were primarily water and nitrogen, essentially achieving zero carbon emissions. Despite it is promising clean energy, the price of ammonia is too high to be employed in high quantities in the industry. In 2021, the export price of ammonia approaches USD 900 per ton. Norway offers the cheapest price globally at around USD

874 per ton, which is still 15% higher than that of fossil fuels [6]. CCS is a technology that comprises the separation of CO_2 from CO_2 emission-intensive industrial sites (chemical plants, coal gasification, cement plants, etc.), followed by transportation and storage. The technology can be used by large stationary point sources, such as fossil fuel-fired power plants, petroleum refineries, steel mills, and so on. According to the project of Texas Clean Energy (a CCS project located in Texas, USA), the rates of carbon captured can be as high as 85–95% owing to the CO_2 adsorbents, which maintain an extraordinary gas adsorption performance at temperatures ranging from −15 °C to 500 °C. The cost of some components for this project amounted to USD 754 million, while the operational cost of the CCS components was USD 8.2 per megawatt-hour. Additionally, there is a risk of leakage from carbon dioxide storage tanks, which, if it occurs, could have adverse environmental impacts on local areas. Therefore, the large-scale application of CCS is unpractical due to its high costs and technical risks. In contrast, carbon capture and application (CCU), which is based on carbon dioxide reduction reactions (CO_2RRs) to produce valuable chemicals, is a viable strategy for advancing a green economy. Captured CO_2 can be directly carried on flue gas from the industry. Its subsequent utilization refers to the deployment of the captured CO_2 for the synthesis of valuable chemicals. Converting CO_2 into valuable chemicals is of great interest to the industry because of its high economic benefits. By July 2018, there were 37 large-scale CCU facilities all over the world [7]. Chemicals converted from CO_2 include methane, methanol, ethanol, ethylene, etc.

However, CO_2 is a chemically inert molecule, and its activation and catalytic conversion normally happen in difficult conditions, normally by the thermocatalytic process under high temperatures of 277–500 °C and high pressure of 3–10 MPa, which can lead to enormous energy losses [8,9]. For example, Kaihang Sun [10] utilized In_2O_3 as a thermocatalyst to conduct a CO_2RR under the reaction conditions of 330 °C and 4 MPa. The resultant methanol production rate achieved was 3.69 $mol \cdot h^{-1} \cdot kg_{cat}{}^{-1}$. The exploration of alternative sustainable catalytic strategies is highly desired. Specifically, photocatalytic CO_2 reduction reactions are typically conducted under ambient conditions, utilizing solar energy as the external energy supply, thereby exhibiting exceptional energy sustainability. However, it was found that photocatalytic CO_2RRs exhibit the characteristics of an inefficient utilization of light energy (less than 10%) by photocatalysts and instability in catalytic performance (less than 20 h) [11]. Recently, Xiaokun Wang [12] prepared a Ni-loaded metal–organic framework (MOF) material for photocatalytic CO_2RRs, demonstrating an exceptionally high selectivity value toward CO of 97.7%. However, a dramatic catalyst deactivation was observed after continuous illumination for 12 h. In addition, electrocatalytic CO_2RRs show great promise owing to their mild reaction conditions and high Faradaic efficiency. Chun-jun Chen and his team [13] applied N, P-co-doped carbon aerogels in CO_2 reduction reactions (CO_2RRs), achieving a remarkable Faradaic efficiency of 99.1% for CO in a carbon dioxide-saturated PF_6/MeCN electrolyte. Electrocatalytic carbon dioxide reductions can achieve a high carbon dioxide conversion (>85%) at low reduction potentials (<−3.0 V). Qing-gong Zhu and colleagues [14] significantly enhanced the carbon dioxide conversion rate on the surfaces of Sn and Pb electrodes by mixing ionic liquids, acetonitrile, and water. At a reduction potential of −2.2 V, they achieved a carbon dioxide conversion rate exceeding 90%. Zhu et al. found that the solution system influences the solubility and mass transfer of carbon dioxide, posing a certain hindrance to the adsorption of CO_2 onto the active sites of the catalyst surface. However, great challenges remain in achieving properties such as the uniform distribution of catalytic active sites and the fast mass transfer of the catalysts [15].

Conventional electrocatalytic CO_2RR materials include metal/metal oxides (i.e., Cu, Ru, Ir, Rh, TiO_2, SnO_2, and CeO_2), metal chalcogenides (i.e., ZnTe, SnS_2, and CdS), carbon nitride, chalcocite materials, and so on [16]. Kun Sun and colleagues [17] employed Au nanoparticles as a catalytic agent to attain a remarkable CO_2 conversion efficiency exceeding 80% at a reduction potential of −0.7 V. However, it is noteworthy that, under these conditions, the mass activity of the catalyst amounted to approximately 4.5 mA/mg.

Additionally, Sun conducted a comparative CO_2 reduction reaction (CO_2RR) test utilizing Au foil under identical experimental parameters. This test revealed a CO_2 conversion rate of merely 70%, accompanied by a mass activity that was half of that observed for the gold nanoparticles. According to Sun's perspective, neither the nano-sized Au particles nor the Au foil demonstrated superior performance in terms of mass activity. This observation is also correlated with their electrochemically active surface area and the electronic structure of the metal. Due to the limitation of the electrochemically active area, the catalytic hydrogenation performance of conventional catalysts is limited. Hierarchical porous materials possess a high specific surface area, which can offer abundant active sites for CO_2RRs. Simultaneously, hierarchical porous materials have excellent substance adsorption and mass transfer capabilities that are used for gas adsorption and separation [18]. Advancements have been achieved in the research domain of carbon dioxide reduction reactions utilizing hierarchical porous materials [19], including metal-incorporated porous metal–organic frameworks (MOFs) and metal-based zeolite materials. Qilong Wu [20] successfully encapsulated potassium nitrate and zinc oxide nanoparticles in situ followed by pyrolysis to obtain a zinc-loaded hierarchical porous carbon material. This material boasts an abundant pore structure and a significant specific surface area (S_{BET} = 2208 cm^2/g). Due to the extensive introduction of pore cavities, the surface of the Zn-loaded porous carbon material is covered with numerous surface defects, providing ample catalytic active sites for CO_2 reduction reactions (CO_2RRs). At a reduction potential of −0.5 V, a near 99% Faradaic efficiency was achieved. Considering the lack of a timely review of the technologies for hierarchical porous materials in CO_2RRs, these technologies must be summarized to obtain a comprehensive understanding [21].

In this paper, this paper provides a concise overview of the synthesis method and the applications of hierarchical porous materials in CO_2RRs. Section 2 delves into the mechanism of carbon dioxide reduction reactions. Section 3 introduces various synthesis techniques employed in the creation of hierarchical porous materials with diverse chemical compositions. The subsequent section mainly outlines the specific applications of hierarchical porous materials in electrocatalytic CO_2RRs. At the end of this review, a perspective on hierarchical porous materials in CO_2RRs is provided for future study. It is our aspiration that this review will serve as a valuable resource for individuals new to or intrigued by this field, offering essential insights into hierarchical porous materials.

2. Mechanism of CO_2 Reduction Reaction

The reaction mechanism of carbon dioxide varies between thermocatalytic and photocatalytic–electrocatalytic processes. In Figure 1A, the thermocatalytic reduction of carbon dioxide to formate intermediates is illustrated. Initially, it can be observed the dissociation of hydrogen with the simultaneous adsorption of carbon dioxide molecules on the catalyst surface [22]. Research has revealed the existence of two forms of CO molecule adsorption on the catalyst surface: top adsorption and bridge adsorption. These two forms remain distinct and do not interchange with changes in the applied current. Top adsorption exhibits a higher likelihood of desorbing to generate CO gas molecules compared to bridge adsorption [23]. Based on these two adsorption modes, active hydrogen atoms bind to the carbon dioxide molecules, resulting in the formation of intermediates such as *COOH (carboxyl) and HCOO* (formate). Subsequently, the active hydrogen atoms further interact with the intermediates, leading to desorption and the formation of formate products.

Oxide layers on metals like Sn and In play a critical role in the reduction of carbon dioxide to formate. As it is illustrated in Figure 1B [22], oxygen forms an oxide layer on the metal surface, acquiring electrons and protons to generate -OH groups in the adsorbed state. Upon the combination of a CO_2 molecule with the hydroxyl group in the adsorbed state, a carbonate intermediate emerges, further evolving into *OCHO or *COOH species. Drawing insights from fundamental electrochemical analyses and Density Functional Theory (DFT) calculations, the research team inferred that the binding energy of *OCHO to the electrode serves as a metric to gauge the selectivity of formate productions. In contrast to metals

like Sn, the formation of carbonate intermediates does not manifest on the surfaces of Pb and Bi metals during CO_2 reduction. Consequently, Pander et al. postulated that, on the Pb surface, the formate product arises from the interaction of *H with CO_2, with DFT computations highlighting the enhanced favorability of the *OCHO intermediate for formate synthesis. Through DFT simulations encompassing 27 metal surfaces, YOO et al. posited that *OCHO intermediates exhibit a greater favorability for generating formate products compared to *COOH intermediates. This preference stems from the robust scaling correlation between *COOH and *H, underscoring the challenge of reducing *COOH to formate products amid hydrogen-evolution side reactions (HERs) on metal surfaces [24].

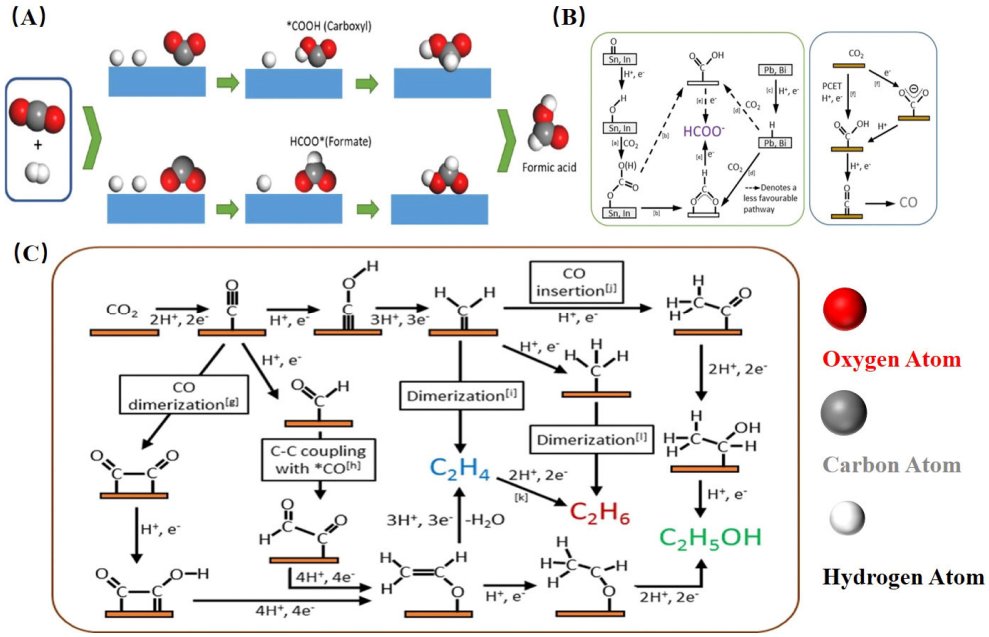

Figure 1. (**A**) Mechanism diagram of thermocatalytic carbon dioxide reduction. In (**A**), the red balls represent oxygen atoms, the gray balls represent carbon atoms, and the white balls represent hydrogen atoms. (**B**) Mechanism of electron participation in catalytic carbon dioxide reduction at the surface of Sn, In, Pb, and Bi metals. (**C**) Mechanism diagram for the preparation of multi-carbon products by carbon dioxide reduction under carbon–carbon bond coupling conditions. Reprinted with permission from [22].

In hierarchical porous structures, CO_2 reduction mechanisms can be enhanced by improving the distribution of catalytic active sites and facilitating rapid mass transfer. The unique characteristics of porous materials, such as an increased surface area and tailored pore sizes, allow for the better adsorption of CO_2 and more efficient reaction kinetics. These structures can optimize the interaction between CO_2 and catalysts, thereby improving the overall efficiency of the reduction process while addressing the inherent challenges of CO_2 activation and conversion [25–38].

In hierarchical porous materials, the interplay between different pore structures significantly influences the mass transfer of carbon dioxide. Macroporous and mesoporous structures primarily play a crucial role in regulating the mass transfer rate. They facilitate the movement of carbon dioxide, allowing it to travel more freely through larger voids and transitional spaces. This enhanced transport can lead to localized increases in carbon dioxide concentration, which in turn drives more molecules to diffuse toward the inner surfaces of the catalyst. On the other hand, the presence of microporous structures offers high specific surface areas and an abundance of active sites for catalytic reactions. While these smaller pores might limit the direct flow of carbon dioxide, they provide the essential environments for reactions to occur once the gas has diffused into these regions. Thus, the combination of macro- and mesopores effectively channel carbon dioxide toward the

micropores, optimizing the overall efficiency of the material in carbon dioxide capture and conversion processes. The hierarchical design ensures that the mass transfer dynamics are balanced, enabling better performance in applications to reduce carbon emissions. Chen Jia et al. [29] prepared a single-atom Fe-N-C catalyst with large mesopores and micropores and studied the effect of mass transfer on catalytic performance in CO_2RR. Chen found that, in the limited mass transfer region, the mass transfer of highly ordered layered porous Fe-N-C was enhanced, and the single atom iron anchored on the porous structure exhibited an excellent CO_2RR catalytic activity (FE_{CO} = 96%, Jco = -19 mA$\times$cm^{-2}). They found that, as the pore size increased, the number of carbon dioxide molecules gradually increased by comparing the concentration of carbon dioxide in the pores. When the pore size is 50 nm, the density of carbon dioxide molecules is the highest, but the migration rate is the lowest. The strong diffusion ability of carbon dioxide toward the inner surface of the catalyst is attributed to the larger mesopores, which create a favorable environment with high local carbon dioxide concentration for the conversion of carbon dioxide to CO. Jiao et al. [26] developed a nanoporous silver catalyst through the selective etching of Ag-Al under acidic conditions and utilized it for CO_2 reduction reactions (CO_2RRs). At a reduction potential of -0.49 V, this nanoporous silver catalyst demonstrated an impressive Faradaic efficiency exceeding 92%, coupled with a current density that was 3000 times greater than that of standard polycrystalline silver catalysts. This remarkable performance can be attributed to the electrochemically active area of the nanoporous silver catalyst, which is 300 times larger than that of its polycrystalline counterpart, and its inherent catalytic active sites, which are 20 times more than those found in polycrystalline silver catalysts. The findings highlight that the development of porous structures in metal-based CO_2 reduction reaction (CO_2RR) electrocatalysts significantly enhances their catalytic performance. This is expected, as the increased porosity contributes to a larger surface area and a greater density of accessible coordination unsaturated sites (like edge and step sites), along with structural defects (such as vacancies and grain boundaries). These features can provide active catalytic sites, making them effective for carbon dioxide electro-reduction [39–42]. At present, hierarchical porous materials have great application prospects in CO_2RRs. The preparation method is crucial for reasonably designing a hierarchical porous catalyst.

3. Synthesis Methods of Hierarchical Porous Materials

Previous research on hierarchical porous materials has focused on exploring various synthesis strategies. Examples of these strategies include the template method, sol–gel method, hard template method, and zeolitization method, among others [43]. These methods can be broadly categorized into basic techniques (such as surfactant templating, replication, and sol–gel), chemical methods (including emulsion templating, phase separation, zeolitization processes, and self-assembly), and physical–chemical methods (such as supercritical fluids, freeze-drying, and selective leaching) [44]. Researchers often combine two or more strategies to tailor materials with distinct characteristics. For instance, the template method and sol–gel method from the basic techniques are frequently used in conjunction with other methods [19,45–47]. One common approach involves combining the template method with the sol–gel method, where template molecules are initially utilized to establish the pore structure, followed by the filling or curing of the material within the template pores using the sol–gel method to create a hierarchical porous structure.

Another example is the integration of the template method with the self-assembly method, where template molecules are first employed to create the pore structure, followed by the formation of a layered structure within the void spaces using the self-assembly method, and ultimately solidifying the structure through subsequent processing steps. These combined methodologies offer a diverse array of options. By employing a systematic design and precise control of the synthesis steps, it becomes possible to adjust the pore structure, size, and connectivity of layered porous materials to achieve multi-functionality, such as catalytic, adsorptive, and transport properties.

3.1. Basic Methods

3.1.1. Surfactant Templating

Surfactant templating (ST) represents a fundamental method employed in the creation of porous materials through the self-assembly behavior of surfactant molecules in a solution, leading to the formation of organized micellar structures. As shown in Figure 2, these structures serve as templates around which the material is deposited, resulting in the eventual development of porous architectures [48]. This technique is primarily utilized for fabricating porous materials with mesoporous structures, enabling the precise regulation of mesoporosity and the mesoporous size while preserving the materials' inherent properties, such as acidity, crystallinity, and thermal stability. The interaction of surfactants within the solvent plays a pivotal role in the generation of porous structures [48].

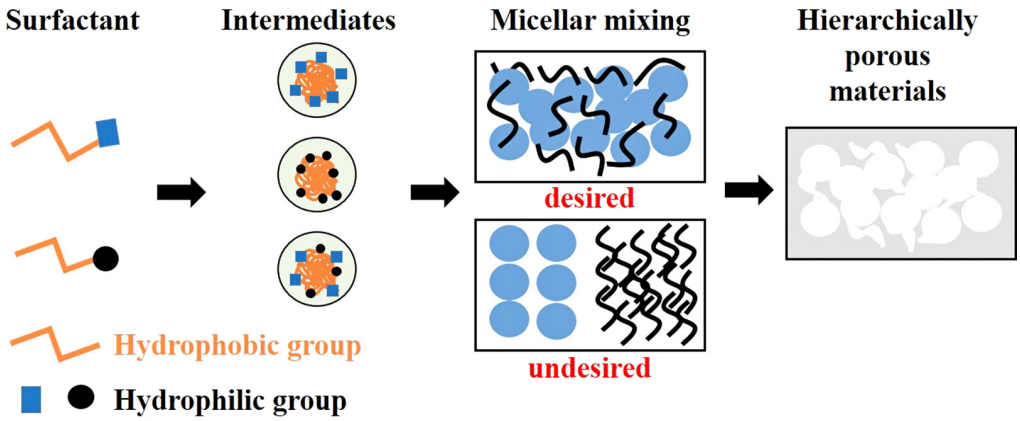

Figure 2. Mechanism diagram of the surfactant template method.

In solution systems, surfactants possess hydrophilic and hydrophobic ends within their structure, a characteristic determined by the functional groups present at their terminal ends and their overall molecular configuration. Typically, two distinct types of surfactants are dissolved in an aqueous medium, leading to the formation of two different micelles. These micelles interact with each other via cross-linking and other bonding mechanisms to create a layered porous intermediate structure. The extent of cross-linking between the micelles is influenced by factors such as temperature, the composition of the solution system, the inherent structure of the surfactant, and the critical micelle concentration of the surfactant in the aqueous medium [49]. Once the surfactants have formed micelles, several additional steps are necessary to facilitate the development of layered porous materials. Initially, precursors and templates of similar polarity coalesce around the micelles, followed by the removal of all templates and surfactant molecules through processes such as high-temperature calcination to yield a hierarchical porous structure.

Ke Li et al. [50] successfully constructed zinc-based metal–organic framework materials with uniform mesoporous channels and crystalline microporous frameworks using amphoteric surfactants as templates, i.e., co-propyl betaine (CAPB) as well as oleamidopropyl betaine (OAPB), in an aqueous system. Li's team synthesized an initial mesoUiO-66-NH_2 sample as well as samples made with CAPB and OAPB as templates in an aqueous system at 60 °C and compared their morphological pore sizes. As shown in Figure 3D, the isothermal adsorption curves are of types I and IV, proving the existence of micropores and mesopores in the material structure, respectively. According to Figure 3B, the average distribution values of the mesopores of the samples made from CAPB and OAPB as templates are 2.8 nm and 3.4 nm, respectively. Representative transmission electron microscopy images of the synthesized meso-MOFs are shown in Figure 3C, and for the CAPB-template mesoUiO-66-NH_2, it can be observed, in Figure 3C(a,b), a homogeneous mesopore and a disordered worm-like arrangement. The magnified images show that the cylindrical mesopores have a regular distribution of diameters, although they lack a long-

term ordered arrangement. For the sample with OAPB as the template, hexagonal-ordered mesopores are observed in Figure 3C(c,d). The samples show a honeycomb arrangement and well-orientated parallel pore channels when observed parallelly and perpendicularly to the channel orientation, respectively.

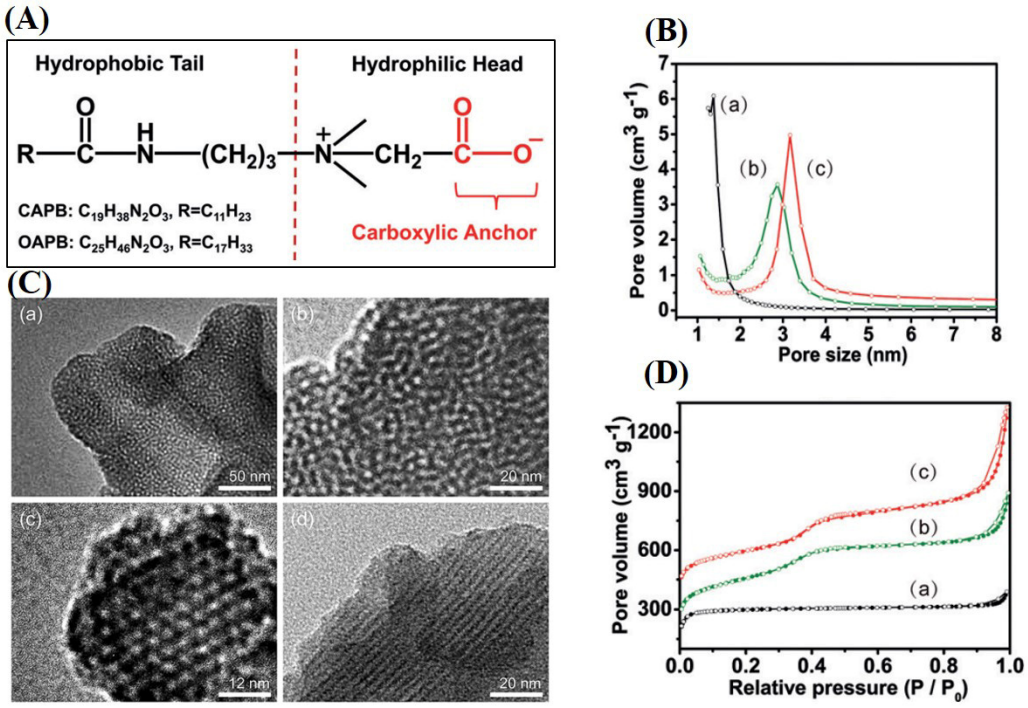

Figure 3. (**A**) Chemical structure of the applied amphoteric surfactants, CAPB and OAPB, (**B**) and (**D**) the corresponding BJH pore size distribution profiles and N_2 sorption isotherms of the pristine UiO-66-NH_2 (a) and the mesoUiO-66-NH_2 synthesized under aqueous solution with CAPB (b) or OAPB (c) as a template. (**C**) Typical TEM images of the as-synthesized mesoUiO-66-NH_2 templates with the surfactants CAPB (**a**,**b**) and OAPB (**c**,**d**). Reprinted with permission from [50].

Ningning He et al. [51] introduced two amphoteric surfactants, namely dodecyltrimethylammonium bromide (DTAB) and octadecyltrimethylammonium bromide (OTAB), as templates to synthesize COF materials with hierarchical microporous/mesoporous structures, named OHMMCOF-DTAB/OHMMCOF-OTAB. As shown in Figure 4A, the key step of the synthesis lies in dispersing DTAB/OTAB in an aqueous solution so that it self-assembles into spherical micelles at the hydrophilic end. With the increase in the temperature, the spherical micelles further self-assemble into columnar micelles, and the addition of DABA promotes the formation of micelles at the peripheral hydrophilic end through ion exchange, resulting in the formation of DABA@columnar micelles. Subsequently, the amino group condenses with the added aldehyde to form COFs. As shown in Figure 4C, the lower BET surface area of the three COFs may be due to the blockage of the inner pores of the COFs by sulfonate ions or long-chain alkyl quaternary ions. Whereas the variation in pore size is reflected in the OHMMCOF-OTAB samples, this may be due to the presence of a large number of ordered aligned templates in the structure, leading to the pore extrusion of the covalent organic framework. Clear lattice stripes with a spacing of 0.34 nm can be observed in the high-resolution transmission electron microscopy images of the three COFs, which are assigned to the (001) lattice planes, further demonstrating their high crystallinity.

Jun Wang et al. [52] synthesized methylpyrrolidinium bromide using ionic liquid surfactants, namely N-hexadecyl-N-methylpiperidinium bromide, N-hexadecyl-N-methylpiperidinium bromide, and N-hexadecyl-N, and then employed a hydrothermal method in an alkaline solution environment to prepare silica with a controllable mesoporous morphology. As depicted in Figure 5A, ionic liquid surfactant (ILS) molecules form

micelles in an aqueous medium, leading to the formation of an intermediate product with a porous structure after undergoing a hydrothermal process at 373 K for 24 h. Subsequently, the resulting product is subjected to calcination at 823 K for 6 h to eliminate the active agent template, thereby yielding a material with a hierarchical porous structure. The silica structures synthesized from the three ILSs as templates were characterized by XRD, and it is visible that there is a large signal peak at 2.28° for MS-P, and three low-signal peaks at 3.93°, 4.54°, and 5.98°, which are associated with the characteristic reflections of the hexagonal structure with a space group of p6mm (100), (110), (200), and (210). There are also four diffraction peaks at 2θ of 2.13°, 3.71°, 4.26°, and 5.66°, indicating that MS-M also has a two-dimensional hexagonal structure. The XRD spectrum of MS-B has only one signal at 1.72°, indicating that the mesoporous structure has a lower-ordered structure. This may be related to the size of the polar head group of the ionic liquid. The research team performed N_2 adsorption and desorption tests on the samples, revealing that the adsorption isotherms corresponded to type IV, indicating the presence of a mesoporous structure characterized by a pore size distribution ranging from 2 to 4 nm.

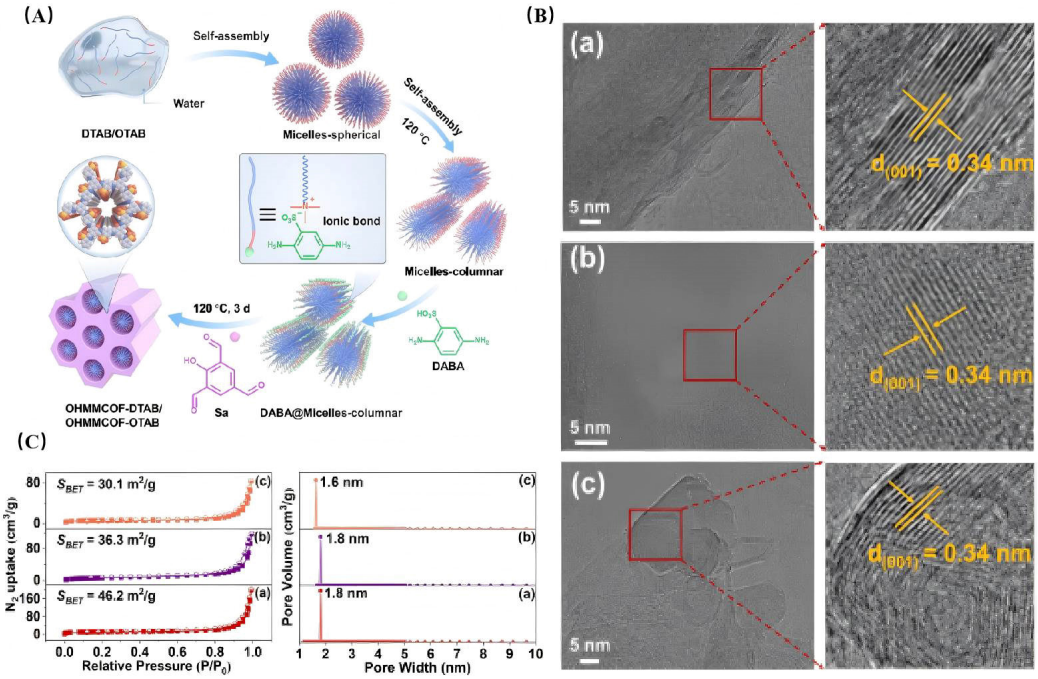

Figure 4. (**A**) Synthesis of OHMMCOF-DTAB/OHMMCOF-OTAB. (**B**) HRTEM images. (**C**) Nitrogen adsorption-desorption isotherms and the corresponding pore size distributions. For all pictures: (**a**) MPCOF (**b**) OHMMCOF-DTAB, and (**c**) OHMMCOF-OTAB. Reprinted with permission from [51].

The surfactant templating approach allows for a predictable design of the pore structure and facilitates the preparation of hierarchical porous materials with uniform pore diameters and a highly ordered structure. Porous materials with specific pore sizes can be prepared by selecting combinations of different surfactants. For example, Li et al. [53] synthesized layered porous carbon microspheres with a maze structure using surfactants such as co-propyl betaine (CAPB) and sodium chloride (NaCl). The distribution of macropores ranges from 10 nm to 45 nm, while the uniform distribution of mesopores is around 3.9 nm. Nevertheless, a significant challenge associated with this method is the difficulty in effectively removing the surfactant template, which subsequently impacts the material properties [53–59].

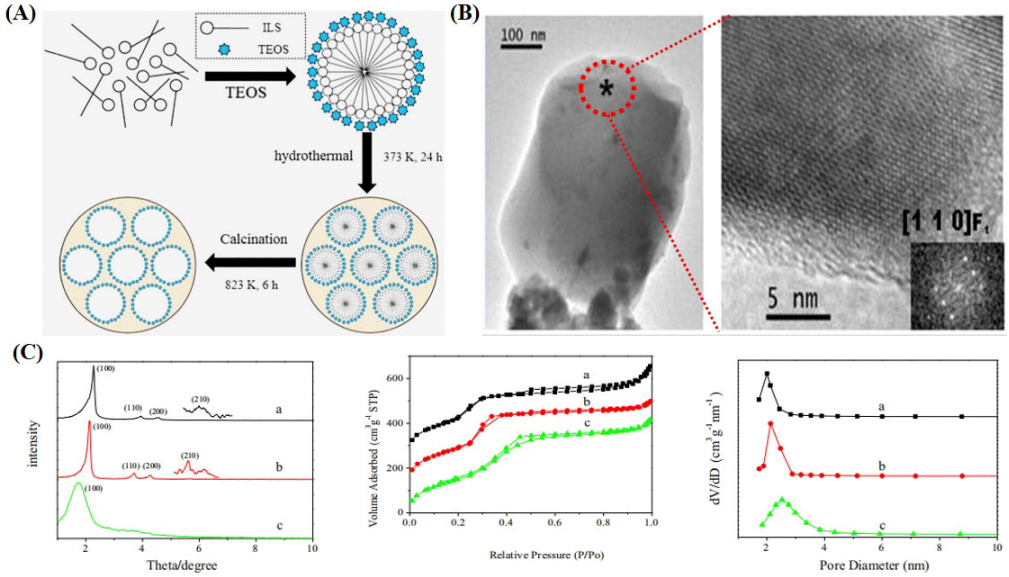

Figure 5. (**A**) The formation mechanism of mesoporous silica using surfactant as a template. (**B**) TEM image of the mesoporous silica. (**C**) XRD patterns, N_2 adsorption–desorption isotherms, and corresponding pore size distribution of (a) MS-P, (b) MS-M, and (c) MS-B (MS-X, the name of samples). Reprinted with permission from [52].

3.1.2. Replication

The template replication method, regarded as a classic approach, has garnered significant attention and finds application across diverse fields. With these methods, there are three main classifications: soft template methods, hard template methods, and biological template methods. In the soft template method, soluble or melt-able materials like polymers, liquid crystals, and organic colloids possessing self-assembly capabilities are commonly utilized as templates for synthesizing porous materials. Contrastingly, the hard template method employs solid materials, such as polymer particles, glass fibers, and oxide particles, as templates. In the bio-templating approach, living organisms like cells, bacteria, and plant tissues serve as templates. Initially, a desired pore structure is crafted within the template, following which the target material is introduced into the pores through filling, impregnation, or deposition techniques. Subsequently, the template material is eliminated through dissolution, heat treatment, or chemical reactions, leaving the porous material behind [60–62].

For instance, as previously mentioned, Rui et al. [63] successfully prepared nitrogen-doped hierarchical porous carbon materials utilizing natural banana peels as precursors. The current synthesis methods typically involve hydrothermal, solvothermal, or ionothermal processes, characterized by high energy consumption, elevated costs, and low efficiency. This study is centered on exploring the synthesis of mercerized zeolite (MOR zeolite) through the ice template method. This method offers a high yield, enhanced crystallinity, reduced water content, significant pressure during reduction, and straightforward setup. It also harbors substantial potential for the industrial-scale production of MOR zeolite. The ice template method, also known as ice casting or ice-induced self-assembly, presents several advantages in porous structure fabrication, including versatility, cost-effectiveness, and environmental friendliness.

Jingguo Jia et al. [64] synthesized a porous boron nitride (p-BN) material using boric acid and melamine as raw materials and used it as a template to grow modified HKUST-1 (a metal–organic framework material of Cu) nanocrystals on the surface of the porous boron nitride material by the in situ growth method and characterized and tested its microporous mesoporous volume surface area. As shown in Figure 6B, the isothermal adsorption curve of the pure p-BN material is of type IV, indicating the existence of microporous and mesoporous structures in the material, while the isothermal adsorption curve of the pure

HKUST-1 sample is of type I. The small hysteresis loops may originate from the pores generated by the accumulation of HKUST-1 nanoparticles. The isothermal adsorption curves of all p-BN@HKUST-1 samples were similar to those of pure HKUST-1, i.e., the adsorption capacity increased sharply and reached a plateau at lower relative pressures, which indicated that the material was rich in micropores. In addition, the H4-type hysteresis curve suggests the existence of narrow slit voids in the hybridized material, which may arise between p-BN and HKUST-1. As it can be observed in Figure 6C, the increase in HKUST-1 nanoparticles with the increase in the number of in situ growth makes the volume of micropores of the hybridized material increase gradually, while the volume of mesopores decreases first and then increases. This may be because the precursors or oligomers of HKUST-1 nanoparticles are filled into the mesopores during the first or second growth process, while the mesopore volume increases with the accumulation of HKUST-1 nanoparticles during the third growth process. In SEM and TEM images, it is difficult to observe the mesopore structure, but the characterization of the texture demonstrates that the mesopore structure is preserved.

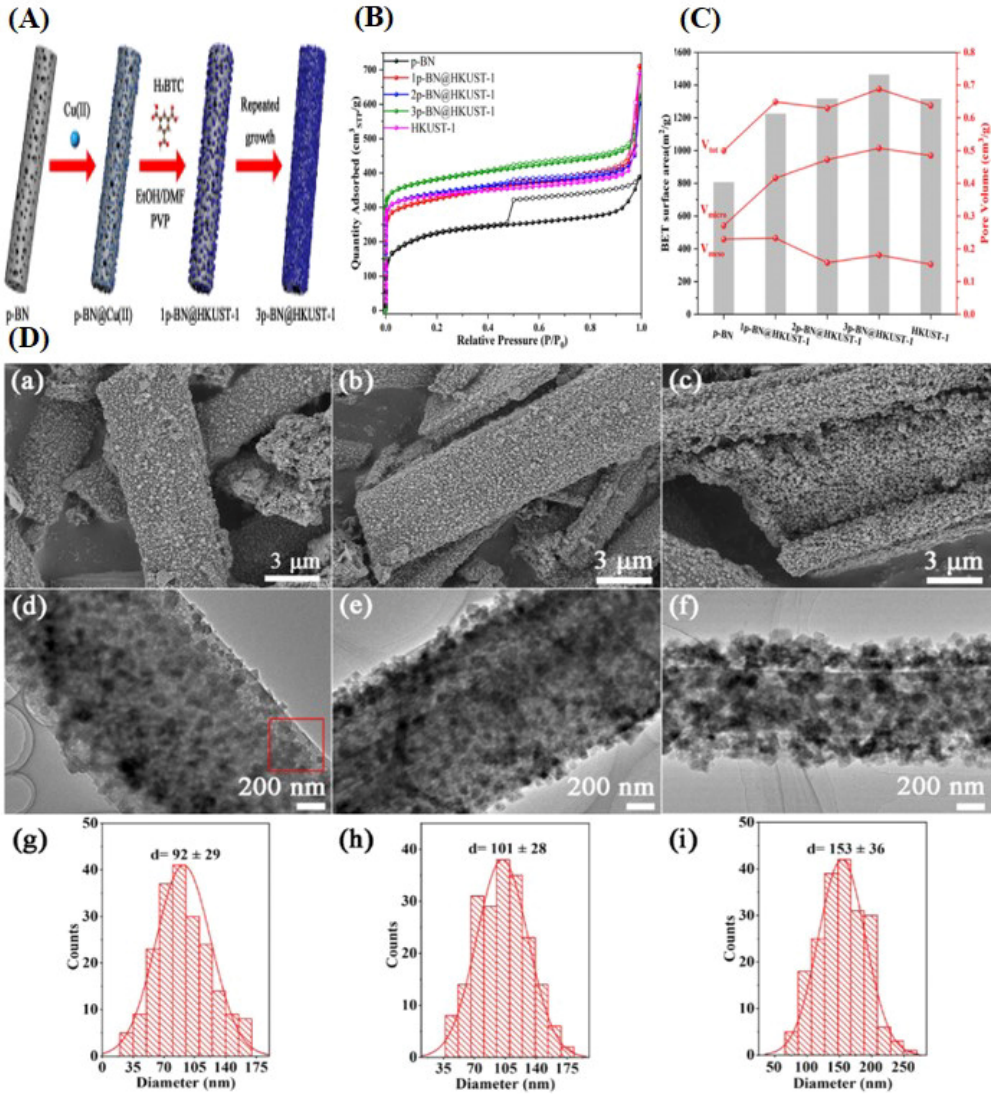

Figure 6. (**A**) Schematic of the preparation of p-BN@HKUST-1 hybrid materials; (**B**) N_2 adsorption–desorption isotherms. (**C**) Corresponding bar plots showing the BET surface areas (S_{BET}), total pore volumes (V_{tot}) and mesopore (V_{meso}) and microspore volumes (V_{micro}) of pristine p-BN, pure HKUST-1, and p-BN@HKUST-1 hybrid materials with different cycle numbers of the growth process. (**D**) SEM images and TEM images of p-BN@HKUST-1 hybrid materials with different cycle numbers

of growth process: (**a**,**d**) 1p-BN@HKUST-1; (**b**,**e**) 2p-BN@HKUST-1; and (**c**,**f**) 3p-BN@HKUST-1. (**g**–**i**) Pore size distribution of all samples. Reprinted with permission from [64].

Luis Estevez et al. [65] synthesized two-layered porous carbon materials, HPC-1-Act and HPC-2-Act (HPC, hierarchical porous carbon; Act, activated), using the template method. Both samples used silica templates to form mesopores. Luis combined ice templates with hard silica templates, which allows for a higher silica-to-carbon precursor ratio. As this ratio increases, the well-dispersed colloidal silica forms local aggregates and forms pores that are larger than the size of colloidal silica. HPC-1-Act, which has a 1:2 ratio of carbon precursor to silica template, HPC-2-Act, which has a 2:1 ratio of carbon precursor to silica, and an over-activated sample, HPC-1-OA, are present, and the three samples are compared in terms of morphology and structure. In Figure 7(A1,B1,C1), it can be observed that, comparing the HPC-1-Act and HPC-1-OA samples, there is an over-activation of the small mesopores, merging to form large pores, while the increase in the ratio of the carbon precursor creates larger pores. The observation of the TEM images of the three samples reveals that the microporous structure of the materials was preserved when the ratio of precursor to template was tuned. The isothermal adsorption curves of all three samples were of type IV (Figure 7D), indicating that microporous and mesoporous structures exist within the materials. Observing the pore size distribution (Figure 7E), it can be observed that, in the HPC-1-type sample, the pore size fraction is mainly concentrated around 80 nm, while the pore size distribution of the HPC-2-type sample is about 10 times smaller than that of the former one, which is also in agreement with the results of the porous density, as reflected in the transmission electron microscopy images.

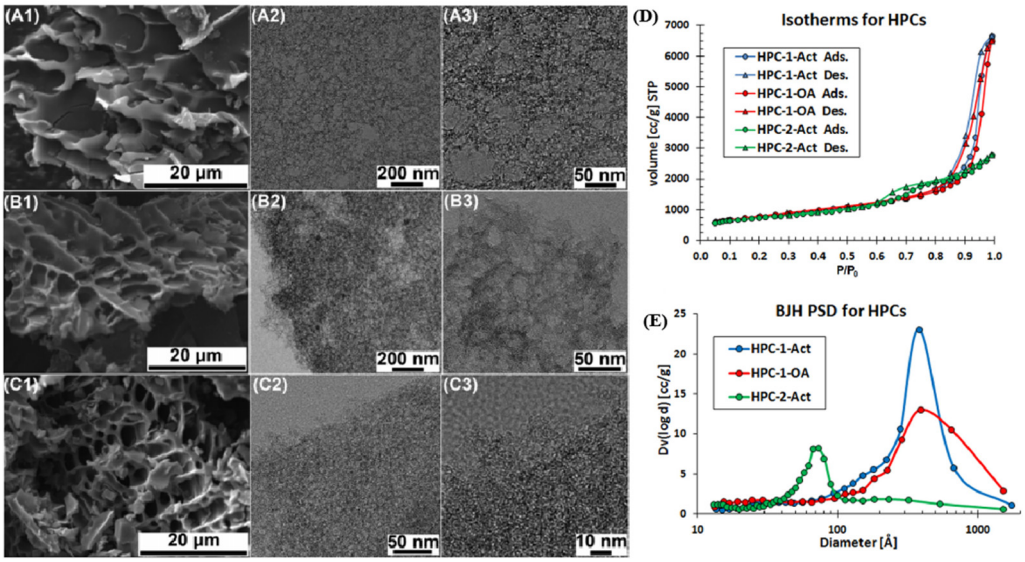

Figure 7. (**1**) SEM, (**2**) TEM, and (**3**) higher-magnification TEM for (**A**) HPC-1-Act, (**B**) HPC-1-OA, and (**C**) HPC-2-Act. (**D**) N_2 sorption isotherms for all the HPCs. (**E**) BJH pore size distribution for all the HPCs. Reprinted with permission from [65].

Bio-templates, as primitive materials in nature, have also been applied to make layered porous carbon materials. Zejun Luo et al. [66] synthesized three-dimensional interconnected layered porous carbon materials using a heavy fraction of bio-oil (HB) as well as crayfish shells (CSs) in combination with different activation temperatures of sodium hydroxide. Luo's team converted lobster shells into lobster shell templates after oxidative digmentation, alkaline deproteinization, and purification steps, as shown in Figure 8A; bio-heavy oil was added to the methanol solution along with crayfish shells to raise the temperature and heat to carry out the carbonization of the material, followed by the addition of an acidic solution to remove the template to obtain a crude sample. Finally, activation was carried out at three different temperatures (700/800/900 °C) to obtain the final product.

The obtained products were named CSB-700, CSB-800, and CSB-900, and another sample, HB-800, without the addition of a lobster shell template was synthesized to compare the morphology and pore size structure characteristics.

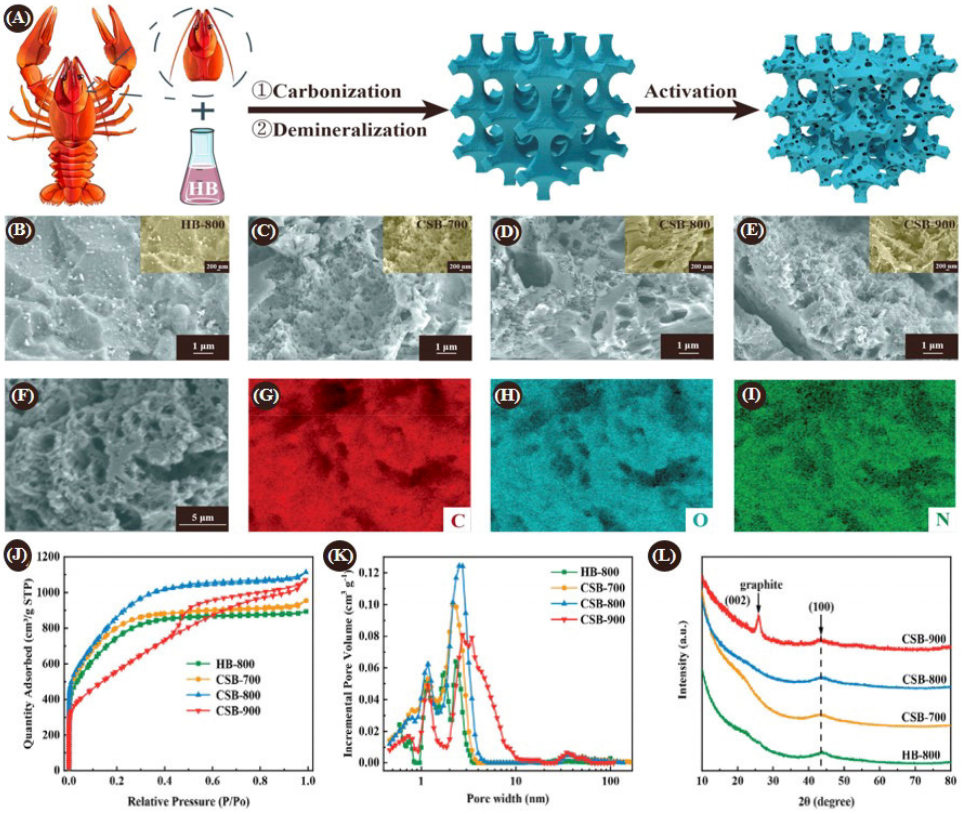

Figure 8. (**A**) Schematic illustration of the synthesis of HPCs from HB via a biological template strategy at different NaOH activation temperatures; FESEM images of (**B**) HB-800, (**C**) CSB-700, (**D**) CSB-800, and (**E**) CSB-900; (**F**–**I**) FESEM image and corresponding EDS mappings of CSB-800; (**J**) N_2 adsorption-desorption isotherms; (**K**) corresponding pore distribution (PSD); and (**L**) XRD pattern. Reprinted with permission from [66].

In Figure 8B–E, it can be seen that the CSB-*n* (*n* = 700,800,900) samples have an obvious layered porous structure compared to the HB-800 sample. This is due to the addition of the CS template during the carbonization process, which provides it a rich hierarchical porous structure and full contact with the etchant during the activation etching stage. Three-dimensional layered porous carbon materials applied in electrochemistry can provide a near-flux migration of electrolyte ions, minimizing the diffusion distance and diffusion resistance. In addition, the pore size increases and then decreases with the increase in the temperature due to the activation function of sodium hydroxide with the increase in the temperature. However, at the peak activation temperature, some micropores or mesopores are destroyed to form mesopores or macropores with larger pore sizes, respectively. The isothermal adsorption curves of all carbon materials are of type IV, with a significant increase in the n_2 adsorption volume at $P/P_0 < 0.01$, and a significant hysteresis loop at $0.4 < P/P_0 < 0.95$, which suggests that there is a large number of micropores and mesopores in the materials. According to the pore size distribution graph, it can be learned that the pore size distribution of HB-800 is around 2.04 nm, of CSB-700 is at 2.03 nm, of CSB-800 is at 2.15 nm, and of CSB-900 is at 3.06 nm.

This paper centers on the replication synthesis of hierarchical porous carbon materials, while also recognizing the potential of the templating approach for producing other hierarchical porous materials. For example, silica can be utilized as a macroporous silicon scaffold in the development of metal-incorporated porous silicon thin-film materials. In this process,

the metallic component contributes to forming a micro- or mesoporous structural backbone, enhancing the overall properties of the resulting material. This versatility of the templating technique opens up possibilities for creating advanced materials with tailored porosity and functional characteristics for various applications. The new pore structure obtained through the post-processing of the template can be combined with the intrinsic pore structure of the template to form a layered porous structure. This approach is suitable for preparing various types of layered porous carbon materials, including macroporous-mesoporous (50–100 nm, 2–50 nm), macroporous–microporous (50–100 nm, <2 nm), and mesoporous–microporous (2–50 nm, <2 nm) configurations [60–62,67–74].

3.1.3. Sol–Gel

The sol–gel method stands as one of the most prevalent techniques utilized in material preparation and synthesis. As shown in Figure 9, a precursor solution is formulated to create a colloid or suspension containing colloidal particles. Subsequently, the solvent is eliminated through evaporation, resulting in the formation of a gel with a distinct structure. This gel is then subjected to a low-temperature heat treatment to yield the desired materials, such as thin films, powders, porous materials, and zeolites. Typically, the precursor solution comprises a solution of metal salts or metal–organic compounds, leading to the hydroxylation of metal alkoxides and salts, thereby forming X-OH colloids (where X represents a metal ion).

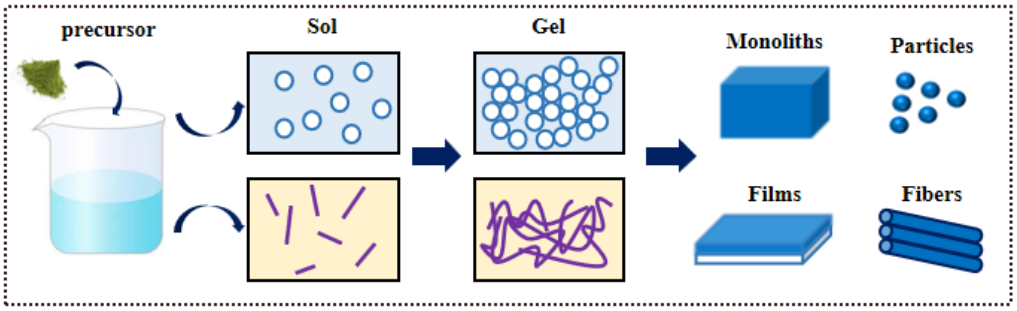

Figure 9. Schematic of the process and products of the sol–gel method.

The process of cross-linking and aging to obtain colloids under specific conditions, known as desolventization, allows for the creation of gels with unique structures [75]. Unlike conventional high-temperature sintering methods, the sol–gel method is conducted at lower temperatures, preventing phase changes or the loss of volatile components in the material. Through the adjustment of precursor solution composition, concentration, and treatment parameters, the material properties can be tailored, ensuring the uniform mixing of sol and continuous gel coalescence. This results in materials with a well-defined chemical structure and diverse pore size morphology.

Pei-Wen Xiao [76] and colleagues synthesized core–shell-structured porous carbon–silica (CS) materials with a uniform structure and morphology using the sol–gel method. As illustrated in Figure 10, Xiao et al. employed a commercial triblock copolymer of ethylene glycol/propanol/ethylene glycol and in situ-formed pyrrole formaldehyde polymer as co-templates, with pyrrole formaldehyde polymer serving as a precursor and tetraethylorthosilicate (TEOS) as the silicon–shell precursor. The feedstock was calcined at 600 °C under nitrogen stream protection to produce the spherical core–shell-structured material CS-PFS. CS-PFS exhibited porosity, with a BET-specific surface area of 410 $m^2 \cdot g^{-1}$ and a pore volume of 0.53 $cm^3 \cdot g^{-1}$. Furthermore, by calcining CS-PFS-Raw (or CS-PFS) or etching CS-PFS with HF, it is possible to obtain pure silica shells or nitrogen-doped carbon materials. The XPS analysis revealed a high nitrogen content in CS-PFS, reaching up to 9.9% (atomic ratio). The nitrogen species present in the materials are predominantly pyridine-n and pyridine-n/pyrrolen, significantly impacting the CO_2 adsorption capacity. Additionally, the CS-PF materials exhibited a favorable selectivity for CO_2/N_2 and CO_2/CH_4 adsorption.

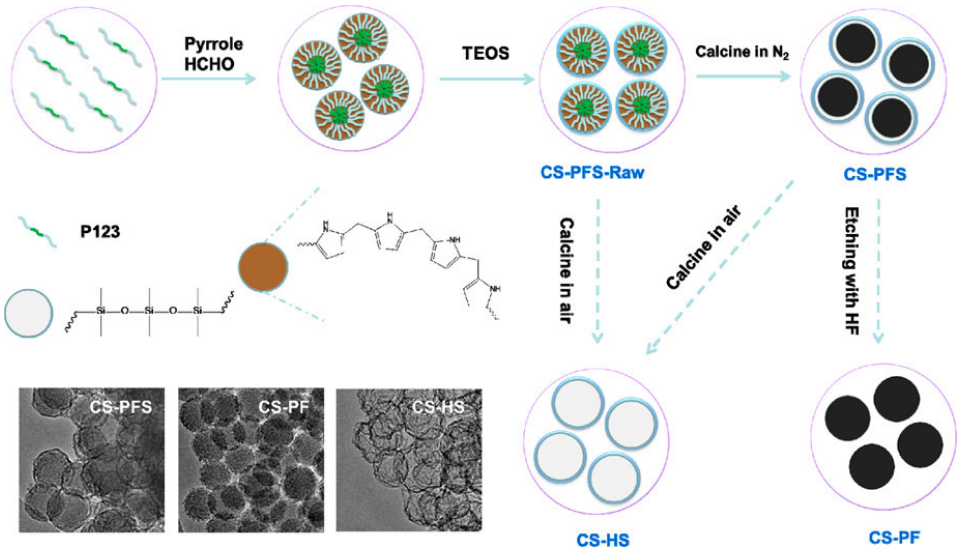

Figure 10. Synthesis Approach and SEM images of Core-Shell Structured Nitrogen-Doped Carbon@Silica (CS-PFS). Reprinted with permission from [76].

Jinhao Li [77] and his team synthesized double-doped boron and nitrogen-layered porous carbon materials by the template-free hydrothermal method using boric acid as the boron source, ethylenediamine as the nitrogen source, dimethylformamide (DMF), 3,3′,4,4′-xylenol tetracarboxylic dianhydride (BTDA) and biphenol (BZD) as the solvents, and diahydride and diamine monomers. Nitrogen-layered porous carbon materials. The sample of B-doped prepared porous carbon material was named BHC-1, the sample obtained by replacing the diamine monomer BZD with pPDA was denoted as BHC-2, and the sample of heteroatom-free porous carbon material prepared without the addition of boric acid and ethylenediamine monomers was denoted as HC. The microstructures of the prepared porous materials are demonstrated in the transmission electron microscopy images in Figure 11A–D, where the microstructures of the materials after re-doping can be observed. The boron and nitrogen elements allowed the material to retain a rich pore structure. Moreover, it can be observed in the HRTEM images that the material shows an amorphous structure without a regular lattice, which is favorable for the adsorption and trapping of gases such as CO_2. The disorder of the material also changed when the diamine monomer was converted from BZD to pPDA, indicating that the diamine monomer played an effective role in regulating the overall structure and pore structure. In Figure 11E, all samples are analyzed by XRD and all samples have two distinct peaks at 23–28° as well as at 42–44°, caused by stacked carbon layers (002) and ordered hexagonal graphite structure (100), respectively. This is a typical feature of amorphous graphite materials, and this result is also consistent with the HRTEM test results. A closer look reveals that the (002) crystal plane of the boron/nitrogen-co-doped carbon material is wider than that of HC, and the diffraction peak intensity is also significantly higher. This result indicates that the disorder and graphitization of the layered porous carbon materials are somewhat improved after heteroatom doping. Nitrogen adsorption and desorption tests were carried out on all the samples, and the results show that the isothermal adsorption curves of the HC samples are characterized by a combination of Type-I and type-IV as well as H4-type hysteresis loops, which proved the existence of micropores and mesopores. In contrast, the isothermal adsorption curves of the BHC-1 sample after the addition of boric acid conformed to the characteristics of type II and type IV, indicating the presence of mesoporous and macroporous structures in the material. When the diamine monomer was replaced with pPDA, the isothermal adsorption curve of BHC-2 showed to be of type I, but its characteristics were not obvious, which also indicated that the material contained only a small amount of pores. These results are also consistent with the pore size distribution results shown.

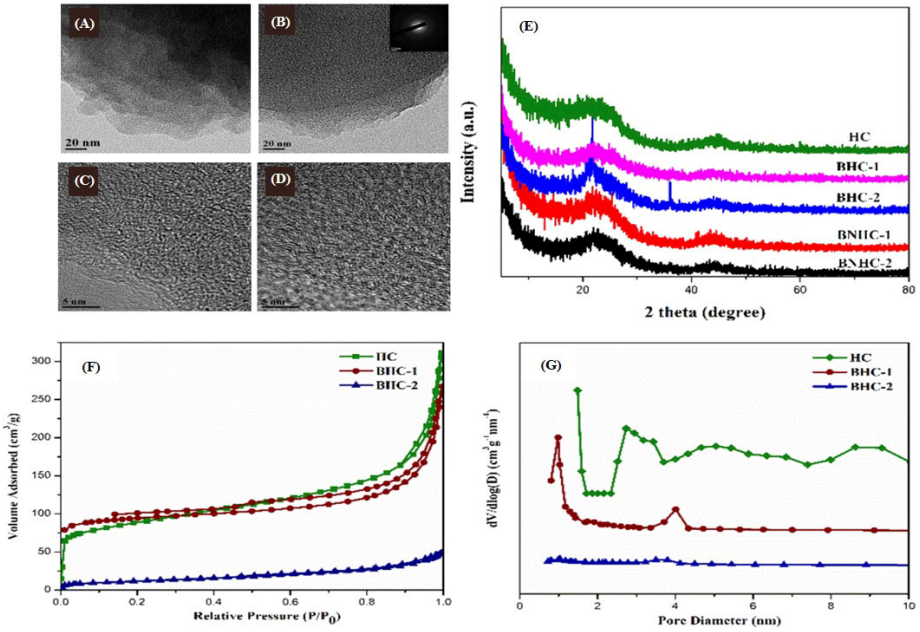

Figure 11. TEM images of (**A**) HC and (**B**) BNHC-1. HRTEM images of (**C**) BNHC-1 and (**D**) BNHC-2. (**E**) XRD pattern; (**F**) N_2 adsorption–desorption isotherms; and (**G**) pore size distributions. Reprinted with permission from [77].

Huichao Chen et al. developed porous calcium adsorbents and investigated the effect of steam on the reactivity of the synthetic adsorbents in a carbonation-calcination atmosphere based on an orthogonal design by doping metal oxides via the sol–gel method. Figure 12A shows the carbonation–calcination reaction system, including the carbonation reactor and calcination reactor. Steam is generated from the steam reactor and forms a gas mixture with CO_2, N_2, and O_2. The sample is then moved between the various reactors. The carbon dioxide capture performance of the synthesized adsorbent at different carbonation temperatures is shown in Figure 12B,C, where the carbonation conversion increases rapidly as the temperature is increased from 600 °C to 675 °C, but decreases slightly with further increases in the temperature, which indicates that the increase in the temperature affects the carbonation of the synthesized adsorbent well, with a relative increase in the sintering resistance. The adsorbents CaO-MgO and CaO-MnO_2 showed a lower decay of carbonation conversion after several cycles. The SEM testing of these two samples (Figure 12D,E) reveals that the samples have small particles with smooth surfaces, and the stacking of particles with particles forms obvious macroporous pores, and this is consistent with the results of the pore size distribution, which shows that the samples have both macroporous and microporous pore structures.

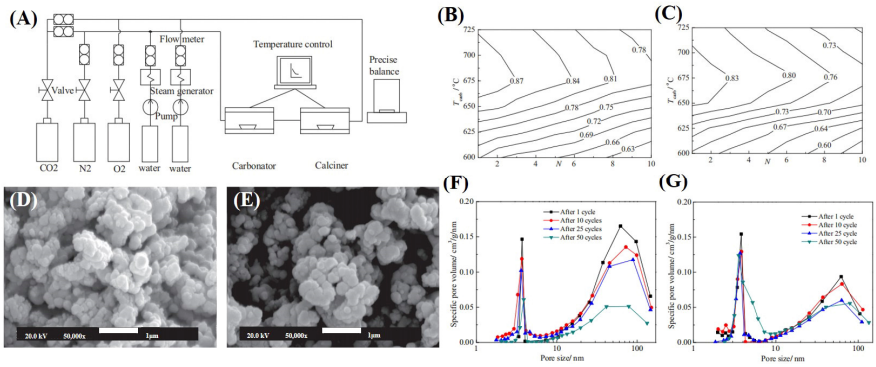

Figure 12. (**A**) Schematic carbonation/calcination reaction system. Effect of the carbonation temperature on the CO_2 capture performance of the synthesized sorbents: (**B**) CaO-MgO and (**C**) CaO-MnO_2.

SEM images of (**D**) CaO-MgO and (**E**) CaO-MnO_2. Pore size distribution of (**F**) CaO-MgO and (**G**) CaO-MnO_2. Reprinted with permission from [78].

Sol–gel methods are widely utilized for synthesizing porous materials that exhibit unique physical and chemical properties. This technique allows for the creation of organic/inorganic hybrid interfaces, which are specifically tailored to enhance the material performance. Through the precise control of the sol–gel process, it is possible to develop organic–inorganic composite porous materials and nanoporous materials that cater to various applications. The sol–gel process involves the transition from a liquid (sol) to a solid (gel) phase, facilitating the incorporation of different elements and compounds at the molecular level. This leads to the formation of materials with tailored porosity, surface area, and functional properties. The sol–gel method is frequently combined with techniques such as freeze-drying and phase separation to create porous materials, including porous aerogels. These methods yield pore structures that typically range from 2 nm to 100 nm, resulting in materials with a highly uniform element distribution. This uniformity makes them particularly suitable for fabricating macroporous and mesoporous materials. The integration of these methods enhances the properties of the resulting materials, making them desirable for various applications, such as insulation, catalysis, and environmental remediation. This method has successfully controlled the design of hierarchical functional 0D, 1D, 2D, and 3D materials, such as particles, fibers, films, and monomers. Using various synthesis strategies, nanostructured materials can be produced through the sol–gel process, and precise definitions and local functions can be integrated into specific locations to maximize their properties and interactions with other functions [75,79–89]. Table 1 summarizes basic methods for preparing hierarchical pore materials.

Table 1. Basic methods.

Method	Structure	FE (%)/Yield (μmol/g)	V_p (cm^3/g)	S_{BET} (m^2/g)	Ref.
Surfactant templating	Meso–micro	-	0.12	46.2	[51]
Surfactant templating	Meso–micro	42.2 μmol/g	0.30	76.0	[55]
Surfactant templating	Meso–micro	360.0 μmol/g	0.05	25.0	[59]
Replication	Macro–meso–micro	81.1%	0.15	270.2	[60]
Replication	Macro–meso–micro	79%	0.54	888.9	[70]
Replication	Macro–meso–micro	-	0.25	913.0	[71]
Replication	Macro–meso–micro	-	0.80	1175.0	[74]
Sol–gel	Meso–micro	-	0.99	1122	[80]
Sol–gel	Meso–micro	-	0.35	188	[82]
Sol–gel	Meso–micro	96.6%	0.92	816	[84]
Sol–gel	Macro–meso–micro	81.1%	-	269	[86]

3.2. Chemical Technology

3.2.1. Emulsion Templating

The emulsion template method is a widely used approach for crafting porous materials, relying on the creation of a stable emulsion system and meticulous control over the porous structure formation through the interplay of dispersed and continuous phases within the emulsion [90,91]. Figure 13 can simply describe the basic principle of preparing hierarchical porous materials by emulsion template method. This interaction stands as the linchpin of the emulsion template method. The method unfolds in several sequential steps: (i) Selection of a suitable emulsifier enabling the formation of a stable emulsion system during the emulsification of dispersed and continuous phases. (ii) Dissolution or suspension of the desired dispersed phase in an appropriate solvent, followed by the addition of the emulsifier. Through proper ultra-sonication or stirring, the dispersed phase is evenly dispersed in the

continuous phase to form an emulsion. (iii) Introduction of precursors or reactants into the emulsion, triggering the desired chemical reaction. (iv) Adoption of methods to solidify the dispersed phase based on the reaction type and precursor characteristics, such as regulating reaction time, temperature, or incorporating cross-linking agents. (v) Removal of the dispersed phase or emulsifier from the emulsion through sintering, dissolution, or other chemical processes, leaving behind a porous material structure with voids and pores. (vi) Implementation of activation or surface modification to further fine-tune the material's structure and properties. By altering emulsifiers, precursors, and processing conditions, diverse porous materials with varying pore distributions and morphologies can be fabricated.

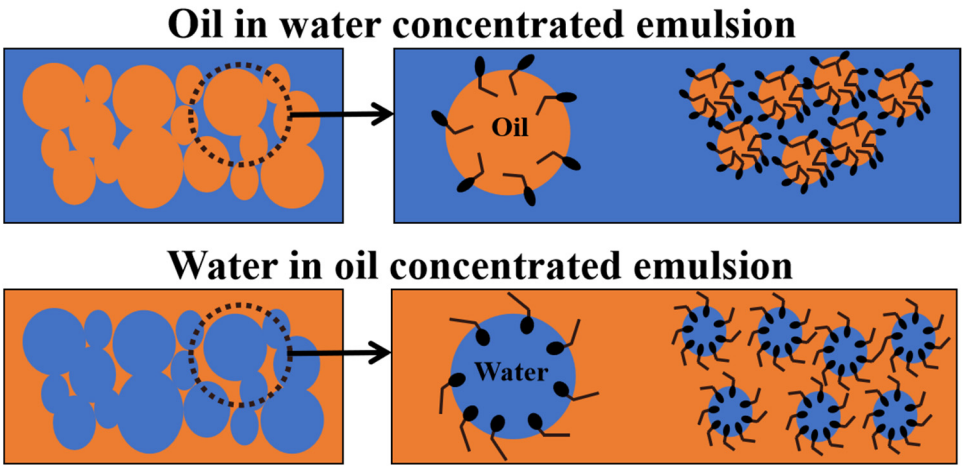

Figure 13. The mechanism diagram of emulsion mixing.

Sungyu Choi and colleagues [92] engineered multiscale porous catalyst layers featuring macropores and mesopores through the one-step emulsion templating technique. In this process, the highly inwardly oriented emulsion Nafion ionomer served as the emulsion template, with aqueous- and oil-phase solutions homogeneously mixed before uniformly coating the desired substrate with the resulting emulsion. Subsequently, the crafted catalyst layer underwent freeze-drying at 0 °C to establish a layered porous structure, followed by heat treatment under specific pressure to eliminate the excess template and yield the final catalyst layer (CL). Throughout the emulsion-drying phase, the emergence of macropores in the material structure was observed as the liquid removal commenced. The mesoporous structure of the catalyst, attributed to the Nafion ionomer, persisted during the drying process, contributing to a hierarchical porous configuration alongside the developed macropores. These macropores play a crucial role in enhancing the catalyst layer's mass transfer efficiency and water removal capability, ultimately boosting substance transport within the synthesized catalyst layer. Furthermore, low-temperature scanning electron microscopy unveiled oil-phase particles exceeding 10 μm in size, with detailed observations indicating the encasement of the oil phase by the water phase. This observation suggests a broad size distribution within the oil phase, as depicted in the magnified images.

Figure 14B and e depict scanning electron microscopy tests conducted on emulsified slurries at low temperatures, whereas images c and f, as well as e and f, showcase the surface and cross-sectional morphologies of the catalyst layers fabricated using the emulsion template method and the conventional spraying method, respectively. A notable observation is that the catalyst layer produced via the conventional method exhibits a well-defined mesoporous structure. In contrast, the catalyst layer generated through the emulsion template method not only features the mesoporous framework of the ionomer condensate but also presents numerous macropores within the mesoporous matrix. When measuring the porosity and pore size distribution of catalyst layers prepared through the traditional method and the emulsion template method using the mercury intrusion porosimetry technique, it was observed that the intermediate pores in the catalyst layer

produced via the emulsion template method were predominantly clustered around 15 nm, with some pores ranging from sub-micrometer to several micrometers in size. In contrast, the average size of the intermediate pores in the conventionally prepared sample was 24 nm, indicating that the catalyst layer synthesized through the emulsion template method boasts a larger framework and superior mass transfer capabilities compared to the conventional counterpart.

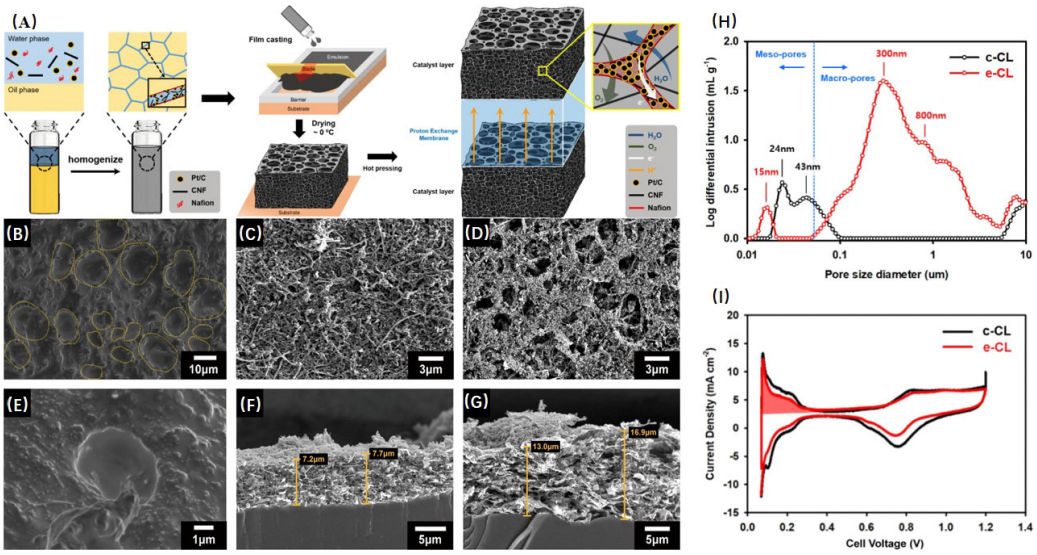

Figure 14. (**A**) Scheme of the emulsion-templated fabrication process and structural features of the resulting CL. (**B**) Cryo-SEM image and (**E**) magnified cryo-SEM image for the e-CL slurry. SEM images of the c-CL ((**C**) surface and (**F**) cross-section) and the e-CL ((**D**) surface and (**G**) cross-section). (**H**) Pore distribution of the c-CL and the e-CL measured by mercury intrusion porosimetry. (I) CV voltammetry curves of the c-CL and the e-CL at 65 °C and RH of 100%. Reprinted with permission from [92].

Ji Han et al. [93] used a hard emulsion-induced interfacial super-assembly strategy to prepare two-dimensional freestanding UiO-66-NH_2 hierarchical porous nanosheets. This strategy relies on the careful design and construction of a 2D sheet-like F127/n-octadecanol "hard" template emulsion, which transforms n-octadecanol from molten droplets to molecular crystals as the temperature drops below the melting/freezing point in protein water emulsions. As shown in Figure 15A, the discrete non-homogeneous nucleation of mesoporous MOF nanocrystals on the 'hard' emulsion template, followed by super-assembly in a loose form over time, is a key factor in the formation of the two-dimensional hierarchical porous nanosheets. In Figure 15B, it can be observed that the prepared 2D UiO-66-NH_2 HPNSs (hierarchical porous nanosheets; UiO-66-NH_2 is the sample name) have a well-defined lamellar morphology, and the average diameter of the MOF nanosheets is ~1.5 μm. A close-up observation of a single UiO-66-NH_2 HPNS reveals the interstitial mesopores on its surface (Figure 15C). In addition, Figure 15D is an SEM image at high magnification, which further reveals a large number of imperfectly interconnected irregular mesoporous MOF nanobodies forming a slit-like porous structure among them. The thickness of the 2D UiO-66-NH_2 HPNS can be found to be ~28 nm in Figure 15E AFM image. The further characterization of the nanosheets using TEM shows that a large number of uniform small mesopores and slit-like large mesopores are present throughout the MOF nanosheets, as shown in Figure 15F. In the MOF nanotubes, the diameter of the uniform small particle pores is about ~8 nm. The crystal structure and phase purity of the prepared 2D UiO-66-NH_2 HPNSs were investigated using XRD analysis. As shown in Figure 15I, the strong diffraction peaks of the 2D UiO-66-NH_2 HPNSs are in good agreement with those of the UiO-66-NH_2 MicroCs, indicating that the two samples have the same crystal structure. Observing the isothermal adsorption curve

of the UiO-66-NH_2 HPNS sample (Figure 15J) reveals that it has a gradual absorption of nitrogen and a hysteresis curve, which also indicates that there is a mesoporous structure in the material, and its pore size distribution values are mainly at 9 nm and 27 nm.

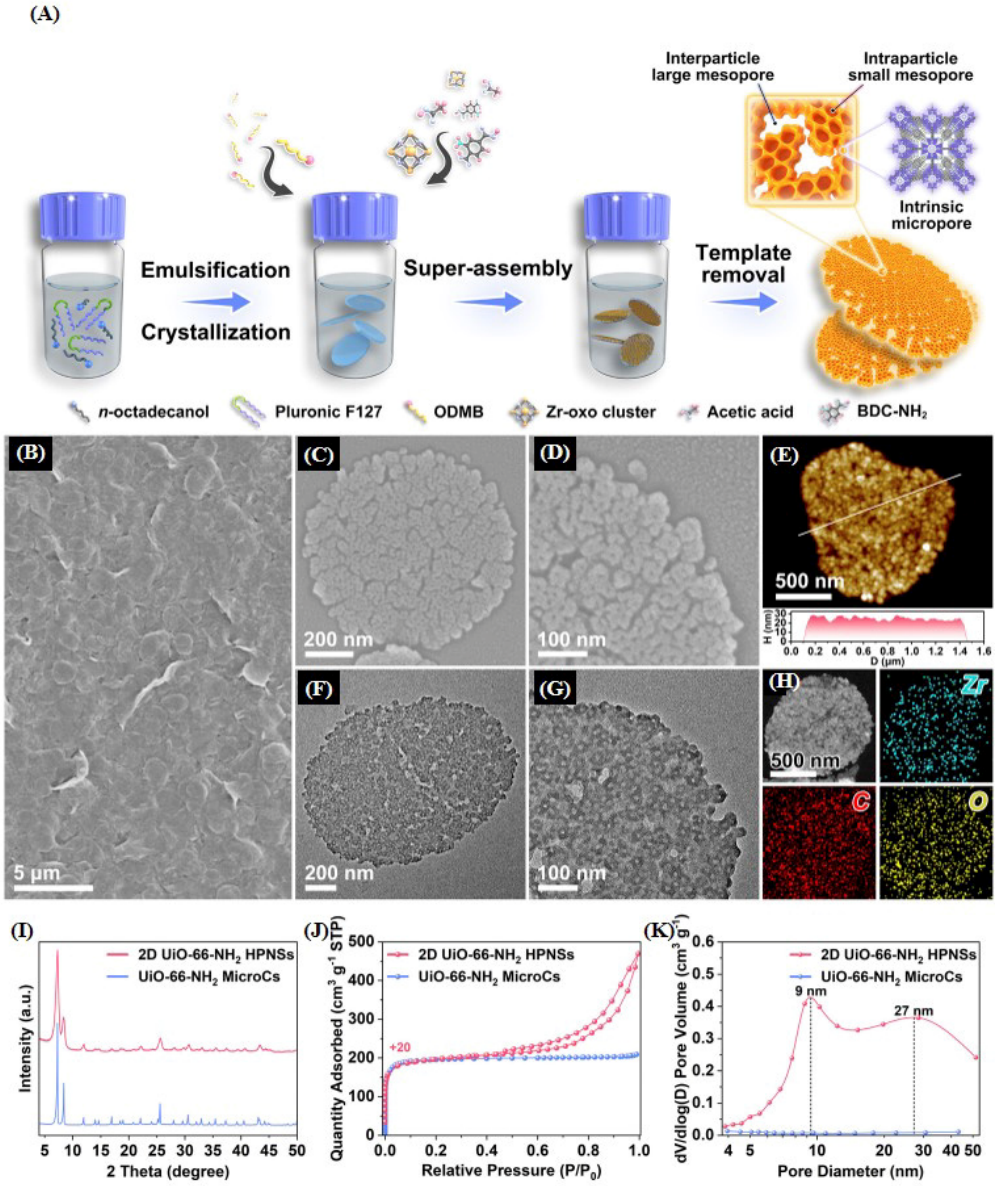

Figure 15. Morphological and structural characterizations of the 2D UiO-66-NH_2 HPNSs. (**A**) Schematic illustration of the synthetic protocol of the 2D UiO-66-NH_2 HPNSs in the F127/n-octadecanol "hard" emulsion system. (**B**–**D**) SEM images, (**E**) AFM image and corresponding height information, (**F**,**G**) TEM images, as well as (**H**) scanning transmission electron microscopy (STEM) image and elemental mappings of the 2D UiO-66-NH_2 HPNS sample. (**I**) XRD patterns, (**J**) N_2 sorption isotherms, and (**K**) BJH pore size distributions of the 2D UiO-66-NH_2 HPNSs and UiO-66-NH_2 MicroCs. Reprinted with permission from [93].

In a study by Zhipeng Wen and colleagues, a multi-template porous superhydrophobic material was crafted utilizing the multi-template high internal-phase emulsion template method. The findings demonstrated that the material exhibited a water contact angle of 143° and an oil contact angle close to 0°, showcasing superhydrophobic and super-oleophilic properties. These characteristics effectively facilitated the separation of submerged oil slicks and heavy oils [94].

As a versatile soft template technique, the emulsion template method finds diverse applications in crafting hierarchical porous functionalized materials, spanning from tissue scaffolds to drug delivery systems and environmental engineering materials. Porous materials prepared using the emulsion template method typically exhibit minimal shrinkage and enhanced structural integrity, making them less prone to breaking. The pore sizes produced through this method generally range from 10 nm to 100 nm. In concentrated lotion environments, however, this range can expand significantly, reaching from 10 nm up to 1000 nm, allowing for a greater versatility in applications that require specific porosity characteristics [95–101].

3.2.2. Phase Separation

The phase separation method is a widely employed technique in the industry for the fabrication of porous materials. This method is derived from the sol–gel process and involves separating the solution phase from the gel phase. By manipulating factors such as temperature control, solvent evaporation, or the addition of additives in the precursor substances and solvent mixture, phase separation can be induced. During this process, different components within the mixture segregate into distinct phases, leading to chemical cross-linking and the formation of layered porous structures with varying pore sizes [102]. These separated phases are then immobilized in the desired configuration through gelation or curing in the phase-separated state. To attain the desired hierarchical porous material, any residual template is eliminated through high-temperature sintering, dissolution, or other chemical reactions post-phase separation. The conventional approach for producing monolithic porous materials involves sol-gel processing combined with phase separation and subsequent thermal treatment, particularly developed within silica systems. In silica systems, phase separation is regulated by adjusting the hydrolysis and polymerization of precursors. Porous monomers are derived from alkoxysilanes, yielding co-continuous macroporous structures through sol–gel transitions that prevent the spinodal decomposition of the transient structure. The resulting silica monomers exhibit smooth, continuous macropores, serving as efficient pathways for mass transfer. Mesoporous structures can be incorporated either through the introduction of external materials into the macroporous framework or during the gelation or curing stages of the material.

Zhi Chen et al. [103] obtained porous carbon nanotubes by removing MoO_2 particles from MoO_2@C core-shell nanofibers synthesized by phase separation using single-needle electrostatic spinning. Figure 16A shows a simple schematic diagram of the synthesized carbon nanotubes, which were firstly synthesized by single-needle electrostatic spinning method using ammonium molybdate tetrahydrate (AMM) and poly (vinyl alcohol) (PVA), which were annealed at 850 °C under an argon atmosphere to form core-shell-structured nanofibers. Porous carbon nanotubes (CNTs) were then obtained by removing MoO_2 with hot nitric acid. In Figure 16B, it can be found that the MoO_2 particles were encapsulated by carbon shells, forming a core–shell structure. The porous carbon nanotubes after heating treatment for 24 h are shown in Figure 16C. As shown in the low-magnification SEM image (Figure 16D), the product has a porous structure. An amorphous and disordered carbon nanostructure is shown in Figure 16E (HRTEM). Figure 16F shows the Raman spectra of porous carbon nanotubes at 1350 and 1600 cm^{-1}, showing the D and G bands (sp2 carbon), respectively. The wide 2D band (=2800 cm^{-1}) indicates that the porous carbon nanotubes are well graphitized, which may play an important role in maintaining the integrity of the tested structures and effectively increasing the conductivity of the porous carbon nanotube electrode. In addition, the N_2 adsorption and desorption isothermal curves of the samples exhibited type-IV isothermal adsorption curves associated with the presence of micropores and mesopores.

Yuji Sato and colleagues [104] prepared five distinct precursor solutions from niobium chloride using phase separation and heat treatment following the sol-gel methodology. The process involved the thorough stirring of the solutions with additives at 0 °C, aging at 60 °C to induce gel formation, and subsequent drying at room temperature. The macroporous

size distribution, as well as the meso- and micropore size distributions, were assessed through mercury pressure and nitrogen adsorption-desorption techniques. It was observed in the Figure 17G that the specific surface area of the material decreased with the rise in the heat treatment temperatures due to crystal coarsening, as determined by the BJH and BET methods. Post-800 °C, no discernible characteristic peaks were identified in the BJH pore size distribution analysis. Even after heat treatment at 800 °C, the macroporous structure remained visibly intact under scanning electron microscopy. Further analysis using field emission scanning electron microscopy depicted a pore structure comprising crystal-to-crystal gaps within the material's framework. The nitrogen adsorption-desorption tests unveiled that the dried gel exhibited a microporous structure, which, however, vanished at 500 °C due to thickening. Samples treated within the range from 550 °C to 600 °C exhibited a mesoporous structure arising from the gaps between the crystals in the framework, with the pore size gradually increasing in tandem with the heat treatment temperature.

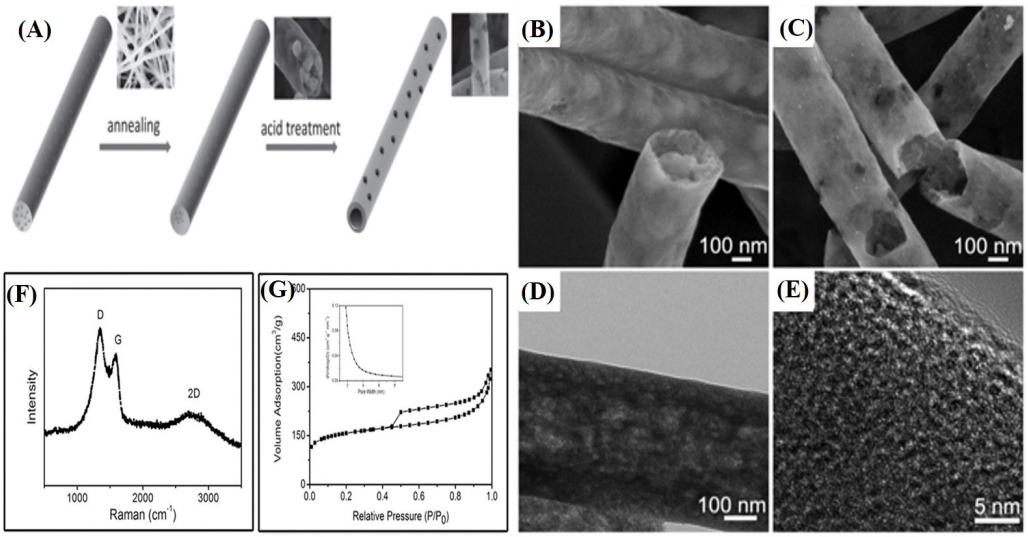

Figure 16. (**A**) Schematic illustration for preparing porous CNTs. (**B**) The image of MoO_2@C core@shell nanofibers annealing at 850 °C. (**C**) SEM images of porous CNTs with nitric acid heat treatment. (**D**,**E**) TEM and HRTEM images of porous CNTs. (**F**) Raman spectra of porous CNTs. (**G**) N_2 adsorption-desorption isotherms (inset is the pore size distribution). Reprinted with permission from [103].

Yu Lin et al. [105] employed the sol–gel and phase separation methods to synthesize nanoporous magnesium fluoride powders and fabricate magnesium fluoride coatings on polytetrafluoroethylene (PTFE) substrates featuring porous multidimensional structures. Initially, PEO was dissolved in anhydrous ethanol and deionized water by Lin et al., followed by the dissolution of $MgCl_2$–$6H_2O$ in water. The PEO solution was then mixed with the $MgCl_2$–$6H_2O$ solution to create a precursor solution. Subsequently, a specific amount of HF was introduced into the solution and stirred for one hour at 80 °C in a water bath under heating conditions to form a sol. After further stirring and the addition of a specific desiccant inhibitor, the sample was aged at 75 °C for a minimum of 3 h and subsequently dried in an oven at 60 °C for 48 h to yield a porous magnesium fluoride sample.

The sample underwent N_2 adsorption and desorption testing, along with BJH pore size distribution analysis, resulting in the acquisition of isothermal adsorption curves and pore size distribution graphs. In Figure 18G, it is evident that the isothermal adsorption curves of the samples exhibited type IV characteristics, indicating the presence of capillary condensation and porous adsorption in all three samples. Among these, S-MgF_2: 0.008‰ displayed the highest adsorption amount and pore count, while S-MgF_2: 0.028‰ exhibited the lowest values for both parameters. Notably, significant variations in the curves were observed in response to changes in the PEO content, underscoring the substantial impact of the PEO quantity on the phase separation structure. Pore size distribution illustrates

the pore size distribution curves of the three samples with varying PEO concentrations. In the S-MgF_2: 0.008‰ sample, a three-dimensional pore structure was evident, encompassing micropores, mesopores, and macropores, with an average pore size ranging from approximately 9.3 nm to 10.8 nm. Conversely, the S-MgF_2: 0.028‰ sample displayed an average pore size of 13.8 nm, indicating that the PEO content influences the degree of phase separation, consequently affecting the material's pore size variability.

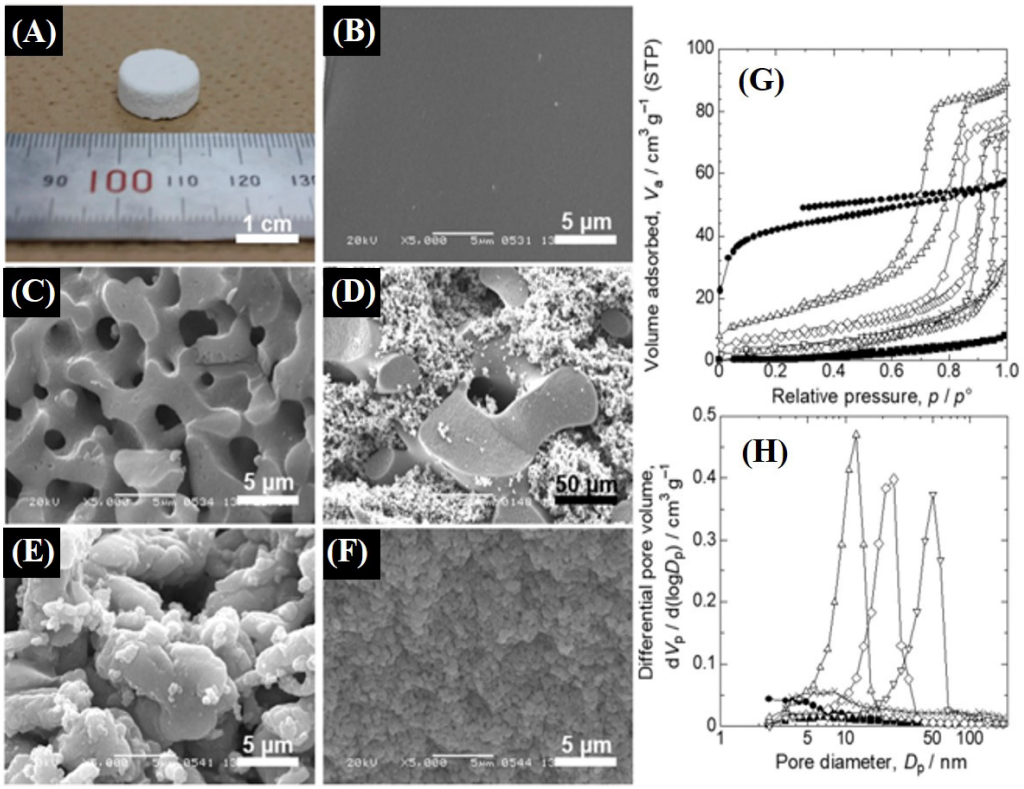

Figure 17. (**A**) Appearance of the resulting dried gel. SEM images of the samples prepared with varied starting compositions: (**B**) Nb-1, (**C**) Nb-2, (**D**) Nb-3, (**E**) Nb-4, and (**F**) Nb-5. (**G**,**H**) Nitrogen adsorption-desorption isotherms and differential BJH pore size distributions of the samples heat-treated at varied temperatures in air. Reprinted with permission from [104].

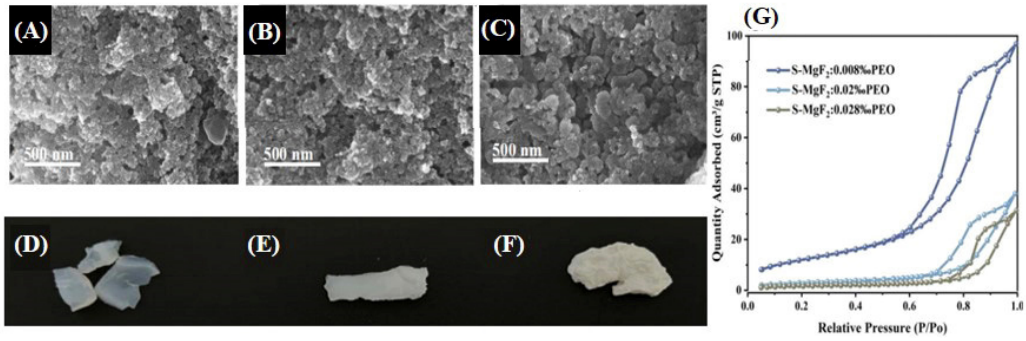

Figure 18. (**A**) S-MgF_2:0.008‰PEO. (**B**) S-MgF_2:0.02‰PEO. (**C**) S-MgF_2:0.028‰PEO. (**D**–**F**) Porous MgF_2 dry gel of (**D**) S-MgF_2:0.008‰PEO, (**E**) S-MgF_2:0.02‰PEO, and (**F**) S-MgF_2:0.028‰PEO. (**G**) Nitrogen adsorption-desorption isotherms with different amounts of phase separation inducer. Reprinted with permission from [105].

Phase separation, as a straightforward synthesis method, is often coupled with other techniques to generate hierarchical porous structures. During the phase separation process, materials inherently develop pores, and the simultaneous occurrence of the self-assembly

process of supramolecular templates and phase separation enables the production of macroporous–mesoporous materials embedded with highly ordered mesopores. During the phase separation process, pore structures are generated, with pore sizes ranging from 10 nm to 10 μm. This method is particularly effective for preparing macroporous, mesoporous, or macroporous structures. For example, in the surfactant template-induced phase separation process, highly ordered mesoporous macroporous skeleton materials can be obtained [106–113].

3.2.3. Zeolitization Process

Zeolitization is a widely employed technique for crafting synthetic layered zeolitized core–shell composites. Zeolites serve as precursors or templates, imparting porous materials with expansive specific surface areas, heightened adsorption capacities, robust acidity, exceptional thermal stability, and precisely defined pore sizes. Through meticulous control at the sol–gel interfacial juncture, the porous materials engendered by zeolites are categorized into three distinct core-shell configurations as shown in the Figure 19 [114].

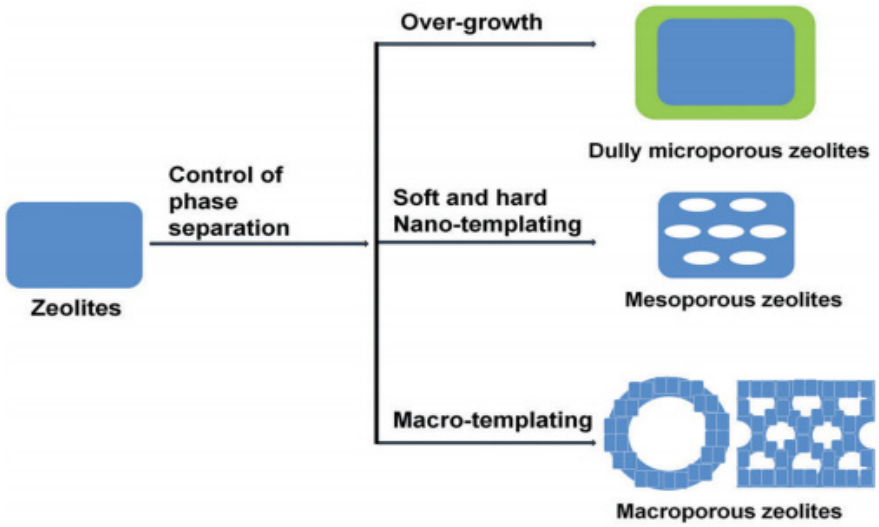

Figure 19. The zeolitization strategies for synthesizing zeolite with hierarchical structures. Reprinted with permission from [115].

In the first scenario, a solitary shell layer envelops the zeolite crystals, constituting a singular core–shell structure. Here, the zeolite crystals are encased by a uniform shell layer boasting elevated crystallinity and porosity. Alternatively, the multicore–shell structure features multiple concentric shell layers within the zeolite crystal, fostering pore connections between these layers and facilitating a stratified pore arrangement conducive to efficient mass transfer and separation processes.

Lastly, the hollow shell structure entails a hollow shell layer encircling the core of the zeolite crystal, creating a spacious internal void suitable for storage and substance transfer. During zeolitization, zeolites with distinct pore structures can be selectively employed for varying objectives. Crucially, the cross-linking of precursors within the zeolite template stands as a pivotal stage in the generation of layered porous architectures or other specialized configurations within zeolites.

Xuguang Liu and colleagues [116] utilized non-nano cubic hierarchical porous TS-1 zeolite (HTS-1), derived from the alkaline hydrothermal treatment of conventional ellipsoidal solid TS-1 (titanium silicate-1), as a crystalline seed for fabricating highly oriented films. The process involved dissolving tetraethyl silicate in deionized water and heating the solution in a water bath within a temperature range of 348–353 K for 1 h. Subsequently, $Ti(SO_4)_2$ was dissolved in hydrogen peroxide to generate a peroxo compound of titanium, which was then added to the previous solution and thoroughly mixed. The resulting homogeneous mixture was then heated in a PTFE-lined reactor at 393 K for 48 h.

The resulting product underwent centrifugation, washing, and drying before being calcined at 823 K for 5 h to yield layered porous non-nano cubic TS-1 zeolite crystal species. Through the alkaline hydrothermal treatment of TS-1 zeolite, hierarchical porous TS-1 zeolite (HTS-1) was produced. The gel mixture was then transferred into a reactor, where the crystalline species were horizontally immersed into the gel. The temperature was gradually increased to 393 K at a rate of 2 K/min and maintained for 48 h. Subsequently, the temperature was reduced to 303 K at a rate of 5 K/min and held for 3 h. Following this process, the samples underwent a nitrogen suction–desorption test to assess the pore structure and pore size distribution.

As illustrated in Figure 20G, the isothermal adsorption curves of HTS-1 and TS-1 exhibit hysteresis loops, indicative of capillary condensation within the material's structure and adsorption occurring in a layered pore configuration. The analysis of the pore size distribution graph reveals that, in traditional TS-1 materials, the pore sizes are predominantly micropores, with an average size ranging from 0.5 to 0.06 nm. In contrast, the HTS-1 material displays a combination of microporous and mesoporous structures, with pore sizes spanning from 2 to 50 nm.

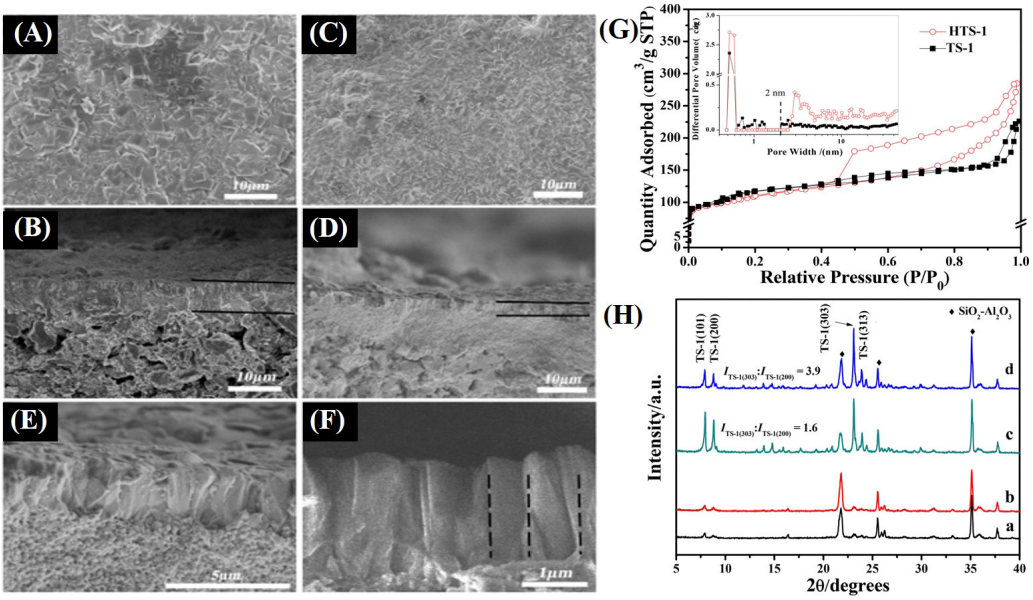

Figure 20. SEM images of the surface and cross-sectional view of the TS-1 (**A**,**B**) and HTS-1 (**C**–**F**) membranes. (**G**) N_2 isotherms of TS-1 and HTS-1 seed (inset is the pore size distribution). (**H**) XRD patterns of TS-1 (a), HTS-1 (b), TS-1 seed layer (c), and HTS-1 membrane (d). Reprinted with permission from [116].

According to the XRD test findings, the HTS-1 membrane has a significant orientation and forms a polycrystalline layer with a thickness of approximately 2–3 μm. In the CO_2/N_2 gas separation evaluation of the HTS-1 membrane, the separation factor was measured at 2.5, while the gas permeability of the HTS-1 membrane was found to be around four times higher than that of the TS-1 samples. This notable increase in gas permeability underscores the HTS-1 membrane's enhanced ability for CO_2 separation.

Compared to hard templates, utilizing soft templates to synthesize mesoporous zeolites through controlled phase separation is relatively straightforward. This is because soft templates can readily self-assemble with silicon-based species. The hydrophilization of the template polymer surface serves as an effective method to control the presence of phase separation. The boiling process effectively preserves the original pore size of zeolite templates, ensuring that the pore structure remains stable, even under high-temperature and -pressure conditions. When utilizing the petrochemical boiling method, the resulting porous materials exhibit a diverse range of pore sizes, extending from micropores (less than 2 nm) to mesopores (from 2 nm to 50 nm). This wide range of pore sizes makes

them particularly suitable for creating gas separation and adsorption materials that feature mesoporous-microporous composite structures [117–126].

3.2.4. Self-Assembly

Self-assembly has found extensive application in synthesizing hierarchical porous materials to create parallel perforated structures with microporous/mesoporous walls. This self-assembly process orchestrates the orderly arrangement of molecules within the material, facilitating the formation of a highly organized hierarchical structure and pore network. By fine-tuning the conditions and parameters of the self-assembly process, one can manipulate the material's pore structure, including pore size, distribution, and connectivity, to impart specific functionalities and applications to the material. The self-assembly process typically involves the following steps: (i) selecting raw materials possessing self-assembly characteristics, such as polymers or liquid crystal molecules; (ii) dissolving the initial raw materials in a suitable solvent to form a homogeneous solution, and then adjusting the pH, temperature, or concentration of the solution to induce the self-assembly process, resulting in the formation of a porous structure with a layered morphology; and (iii) introducing cross-linking agents to solidify and stabilize the porous structure.

Na Sheng and colleagues [127] utilized a solvent-free approach to thermally decompose solid dipropylammonium phosphate (DPA-H_3PO_4) at 200 °C, leading to the formation of DPA molecules without the use of mesoporous templates. This process triggered the self-assembly of solid DPA-H_3PO_4 into SAPO-11 molecular sieves characterized by a layered structure. Specifically, a mixture of Al_2O_3, P_2O_5, DPA, SiO_2, and H_2O in molar ratios of 1, 0.8, 0.24, 1.6, and 2.4, respectively, was milled at room temperature and subsequently heated at 200 °C in a stainless-steel autoclave lined with polytetrafluoroethylene. During the heating process, an amorphous phase formed after 4 h, and with further heating for 8 h, the DPA-H_3PO_4 molecules decomposed, releasing DPA gas and initiating the generation of mesopores within the material. It is noteworthy that the synthesis of SAPO-11 with a highly hierarchical porous structure was unsuccessful when water was introduced as a solvent into the system. This can be attributed to the significant decrease in the sample porosity as the molar ratio of water increased, as the DPA molecules tend to dissolve in the solvent rather than being released as a gas, hindering the formation of the desired pore structure. To delve deeper into the self-assembly mechanism of SAPO-11, the research team led by Na conducted an analysis utilizing XRD (Figure 21A), SEM (Figure 21B), and N_2 adsorption and desorption tests (Figure 21C). The XRD data revealed the emergence of characteristic crystal peaks in the curve after 6 h of heating, with the sample achieving full crystallization at 13 h, as evidenced by well-defined peaks.

Notably, there was little disparity between the curves at 13 h and 14 h of heating, indicating complete crystallization at the 13-h mark. The SEM imaging of the intermediate stages showcased a distinct mesoporous structure becoming prominent after 6 h of heating. The analysis of the N_2 isothermal adsorption curve (Figure 21C) highlighted a significant decrease in N_2 absorption below 6 h or above 13 h, with a less pronounced hysteresis loop, suggesting that mesopores primarily developed between the 6- to 13-h heating window. Catalytic evaluations for n-dodecane hydrogen isomerization demonstrated that the Pt catalyst supported on S-meso-SAPO-11—13 h exhibited a superior isomer selectivity compared to the Pt catalyst supported on conventional SAPO-11 (Pt/C-SAPO-11). This enhanced selectivity, coupled with the absence of mesoscale templates, presents a promising avenue for the cost-effective synthesis of hierarchical molecular sieves with potential applications in n-dodecane alkane hydrogen isomerization processes.

Xin Zhang [128] prepared porous photoluminescent cellulose fibers by the self-assembly of porous cellulose fibers constructed by the hydrolysis of microcrystalline nanocrystals (CNCs) via sulfuric acid to obtain cellulose nanocrystals (CNCs) and the compression of CNCs into a coagulation bath containing the silica precursor obtained by the hydrolysis of tetraethylorthosilicate, which were then combined with graphene carbon quantum dots (GQDs). As shown in Figure 22A, the coagulation bath is usually made of 15 wt.% sodium

hydroxide solution and ethanol, to which a certain amount of the silica precursor solution is added for homogenization, followed by injection of 10 mL of the CNC (3 wt.%) suspension into the coagulation bath via wet spinning, and the self-assembly of CNC fibers is formed by electrostatic repulsion and van der Waals forces. After 12 h of self-assembly, the alcohol-washed product yielded CNCs/SiO_2 composite fibers (CS), which were acid-washed to remove SiO_2 and washed and dried to yield porous cellulose fibers (C2). In Figure 22B,C, it can be observed that a small number of irregular SiO_2 particles are visible on the fiber surface after 3 h of self-assembly. With the increase in the self-assembly time, more SiO_2 particles were formed in the composite cellulose fibers and gradually approached a spherical shape (Figure 22D–F). Observing the surface morphology (Figure 22K), the surface consists of a porous network with a large number of macroporous structures. Figure 22H shows the isothermal adsorption curves of C2–400, and it can be seen that its isothermal adsorption curves are not closed or crossed, which indicates that the surface area of this sample is small, and is also consistent with the results of the surface morphology. Apparently, the isothermal adsorption curves of C2–600 and C2–800 (Figure 22I,J) are of type IV, where the capillary line condenses and the isotherm jumps upward when the relative pressure is more than 0.5, and there is a H3-type hysteresis loop, which may be due to the slit voids of the sample. The distribution values of the pore sizes of C2–400 are around 2 nm and 6.3 nm, and these micropores may be due to the injected CNC suspensions solidifying violently in the solidifying solution and the internal polymer condensing slowly due to double diffusion. The pore sizes of C2–600 and C2–800 are centrally distributed around 28.8 nm and 20 nm, respectively.

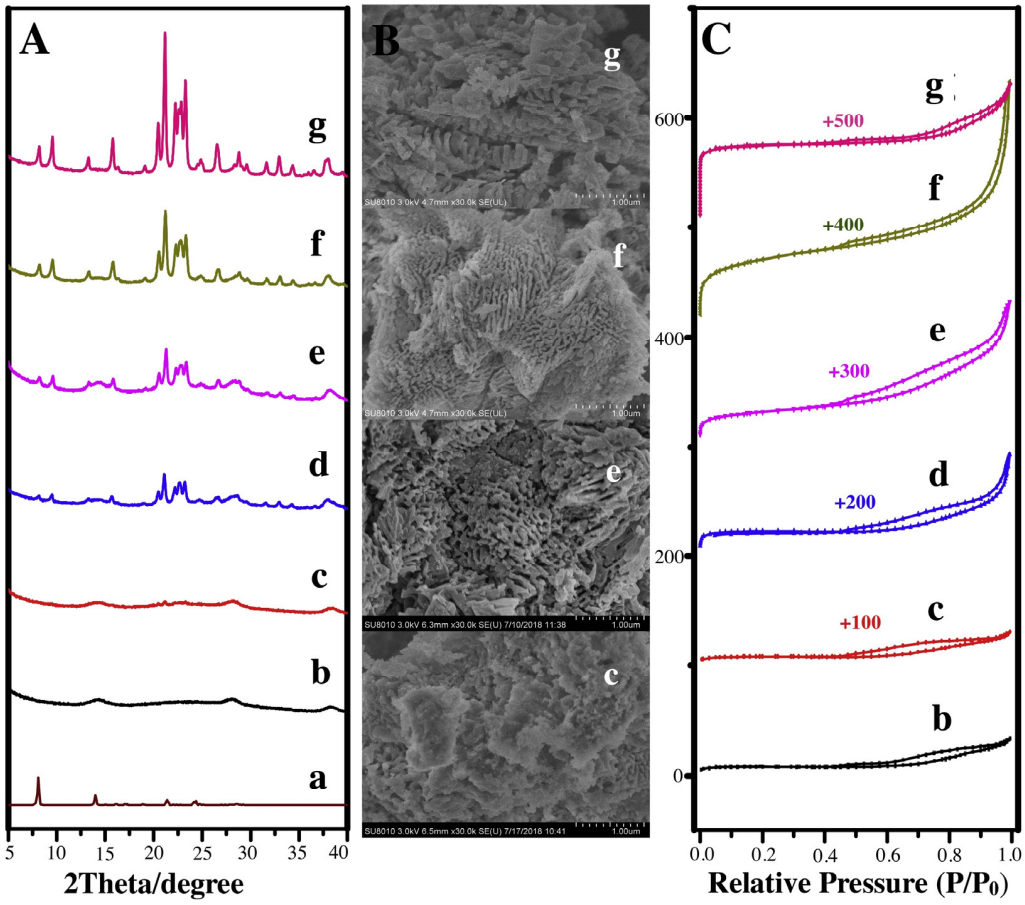

Figure 21. (**A**) XRD pattern. (**B**) SEM images. (**C**) N_2 sorption isotherms of the washed S-SAPO-11 samples crystallized at (a) 0 h, (b) 3 h, (c) 4 h, (d) 6 h, (e) 9 h, (f) 12 h, and (g) 14 h. Reprinted with permission from [127].

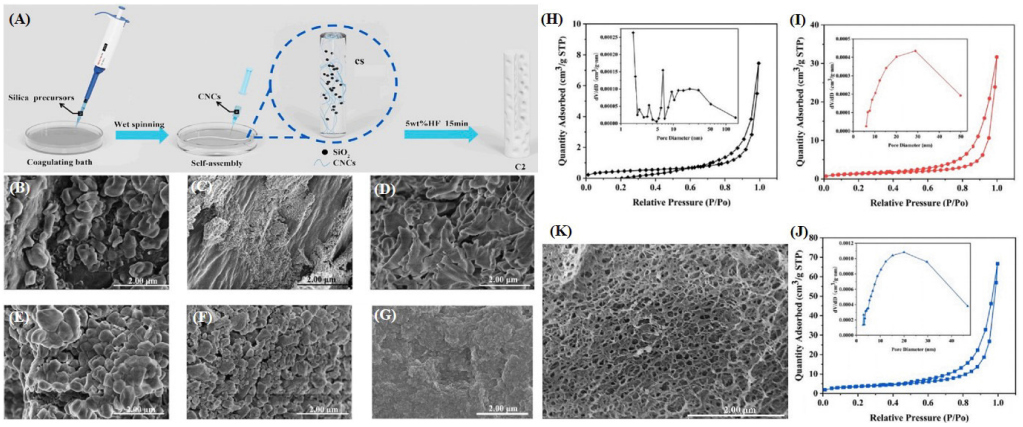

Figure 22. (**A**) Illustration of the preparation of mesoporous cellulose fibers by the self-assembly method. SEM images of the surface of the composite cellulose fibers obtained with the silicon precursor at an added amount of 800 μL after different self-assembly times in the coagulation bath: (**B**) 3 h under high magnification, (**C**) 3 h under low magnification, (**D**) 6 h, (**E**) 9 h, (**F**) 12 h, and (**G**) 18 h. N_2 adsorption-desorption isotherms and pore size distribution of three porous cellulose fibers: (**H**) C2–400, (**I**) C2–600, and (**J**) C2–800. (**K**) SEM image of the surface morphology. Reprinted with permission from [128].

Seongseop Kim [129] developed a polymer-polymer interfacial self-assembly strategy to synthesize hierarchical porous carbon nanosheets (HNCNSs) with microporous and mesoporous structures by combining the migratory behavior of immiscible-phase ternary polymers with the self-assembly of block copolymer (BCP) orientation. As shown in Figure 23I, Kim used excess homopolystyrene (hPS) and homopoly (methyl methacrylate) as the main phases; poly (ethylene oxide) -b-poly(styrene) (PEO-B-PS) as the structural director; phenol-formaldehyde (PF) and melamine-formaldehyde (MF) resins as the carbon and nitrogen precursors, respectively; and predehydroxysilylates (AS) sols as the porogen for micropores in tetrahydrofuran (THF). In order to study the polymer–polymer interfacial self-assembly, BCP/AS/PF-MF hybrids of 100 nm thickness were micro-cut and subjected to TEM tests, and the results are shown in Figure 23A. After solvent evaporation, the BCP-rich phase (dark region) was confined at the boundary between the hPS (gray region) and hPMMA (bright region) macroscopic domains to reduce the surface tension. After carbonization and the removal of AS species by sodium hydroxide etching, SEM images and TEM images show that the HNCNSs have an ultrathin 2D structure, which is built by a monolayer of ordered mesoporous structures (Figure 23B–D). In Figure 23E,F, it can be observed that the thickness of the HNCNSs in the AFM image is ~8.8 nm and the thickness of the overlapped HNCNSs is ~16 nm. The isothermal adsorption curves of the HNCNSs (Figure 23G) are of type IV, with capillary shrinkage at a relative pressure of P/P_0 of 0.9, which suggests that there is a predominantly macro-mesoporous structure in the material, as indicated by the distribution of the pore sizes. It can be seen that the micropores of the material are mainly distributed at 0.6–1.4 nm, and the mesopores are mainly at 25 nm.

Self-assembly exhibits notable advantages as follows: (1) it possesses the capability to synthesize oxide materials characterized by a hierarchical porous structure directly; (2) the operational procedure is straightforward to implement; and (3) it holds promising prospects for industrial-scale application. Moreover, this approach can be easily integrated with other techniques to synthesize the hierarchical porous materials with specific structures and functions. Recent studies have demonstrated the successful preparation of carbon nanotube materials characterized by a uniform pore size distribution and elevated porosity, generally featuring pore sizes below 50 nm. In contrast, dual continuous porous materials fabricated through the self-assembly of block copolymers can attain significantly larger pore sizes, typically ranging from tens of nanometers to several hundred nanometers. This advancement in material synthesis opens up new potential applications, particularly in

areas such as catalysis, gas separation, and drug delivery systems, where tailored pore structures are advantageous [130–138]. Table 2 includes the hierarchically porous materials prepared by chemical methods and their basic parameters.

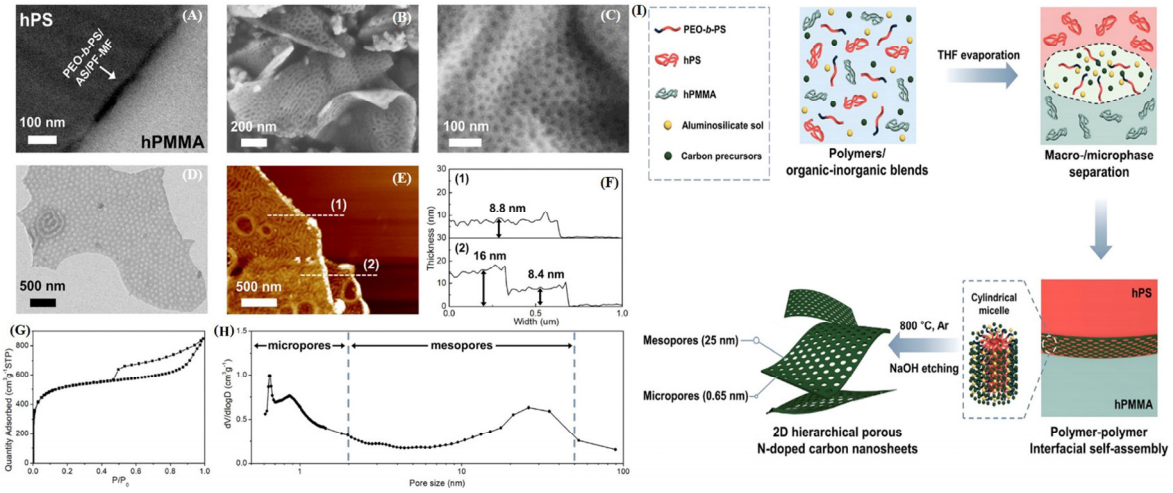

Figure 23. Characterization of an HNCNS. (**A**) TEM image of microtomed PEO-b-PS/AS/PF-MF hybrids at the hPMMA-hPS interface. (**B**,**C**) SEM, (**D**) TEM, and (**E**,**F**) AFM images with the corresponding height profiles of the HNCNS. (**G**) N_2 sorption isotherms. (**H**) Pore size distribution. (**I**) Schematic representation of polymer interfacial self-assembly for the 2D engineering of hierarchical porous N-doped carbon nanosheets. Reprinted with the permission from [129].

Table 2. Chemical methods.

Method	Structure	FE (%)/Yield (μmol/g)	Vp (cm^3/g)	SBET (m^2/g)	Ref.
Emulsion template	Macro–meso–micro	-	0.58	1145.2	[97]
Emulsion template	Macro–meso–micro	94%	0.2	961.3	[100]
Phase separation	Macro–meso–micro	-	0.79	889	[105]
Phase separation	Macro–meso–micro	77%	0.30	675	[110]
Phase separation	Meso–micro	-	0.02	3.7	[112]
Phase separation	Meso–micro	-	0.60	1374	[113]
Zeolitization	Macro–meso–micro	-	0.1	314	[120]
Zeolitization	Meso–micro	-	0.2	855.4	[125]
Zeolitization	Meso–micro	68%	0.21	269.7	[126]
Self-assembly	Meso–micro	420 μmol/g	0.18	335.1	[134]
Self-assembly	Meso–micro	73.9 μmol/g	-	268.2	[138]
Emulsion template	Macro–meso	74%	0.24	812	[139]

3.3. Physical–Chemical Methods

The utilization of physical methods in synthesizing hierarchical porous materials represents more than just a physical reaction process; it involves a synergy of physical and chemical techniques where chemical reactions occur before and after the physical processes. Key methodologies encompass the supercritical fluid method, freeze-drying method, and selective erosion method, among others.

3.3.1. Supercritical Fluids

A supercritical fluid exists in a state of matter between liquid and gas, where, at temperatures or pressures surpassing the critical point, the distinction between gas and liquid vanishes, yielding a unique phase. In this distinctive state, supercritical fluids exhibit a significantly lower viscosity than liquids and excellent diffusion properties, with extensively applications in catalytic reactions, separation technologies, and the synthesis

of nanomaterials [140]. In the fabrication of layered porous materials, the elimination of solvents can lead to structural alterations or even the collapse of the material. However, supercritical fluids, devoid of a gas–liquid interface, mitigate the risk of structural modifications and simplify solvent removal. Commonly selected supercritical fluids encompass carbon dioxide, water, and ethane, among others. Their high diffusivity and solubility characteristics facilitate the uniform dissolution of feedstock, enable the incorporation of templating agents into the homogeneous solubility system, and support reactions under specific conditions to engender the desired porous structure.

Zi-tong Zhuang [141] and his team developed a supercritical carbon dioxide (SC-CO_2) pretreatment technique to process walnut shell (WS) waste to prepare porous biochar precursors and used potassium hydroxide activation to prepare biochar adsorbent materials. Zhuang et al. introduced walnut shells into a reactor, then exhausted the air with CO_2, and kept the reaction material in supercritical CO_2 at a constant temperature and pressure. The obtained intermediates were mixed with potassium hydroxide and dried in a vacuum oven at 105 °C for 24 h, and the alkaline residue was removed to obtain the activated carbon material (AC). As it can be seen in Figure 24A–C, the external structural morphology of the biomass changed significantly after the pretreatment and activation steps. The structure of the walnut shell feedstock showed irregular lumpy particles with a relatively fatty surface and no obvious pore structure. In contrast, the surfaces of the char after the supercritical CO_2 treatment became rough and inhomogeneous, with abundant honeycomb pore structures having formed on the surface. Zhuang attributed this transformation to the pyrolysis of hemicellulose, cellulose, and lignin and the subsequent gas release. The AC after the activation step also exhibited a honeycomb pore structure, but the number of pores was significantly increased compared to the structure of the pretreated samples, which had smaller and more compact pore sizes.

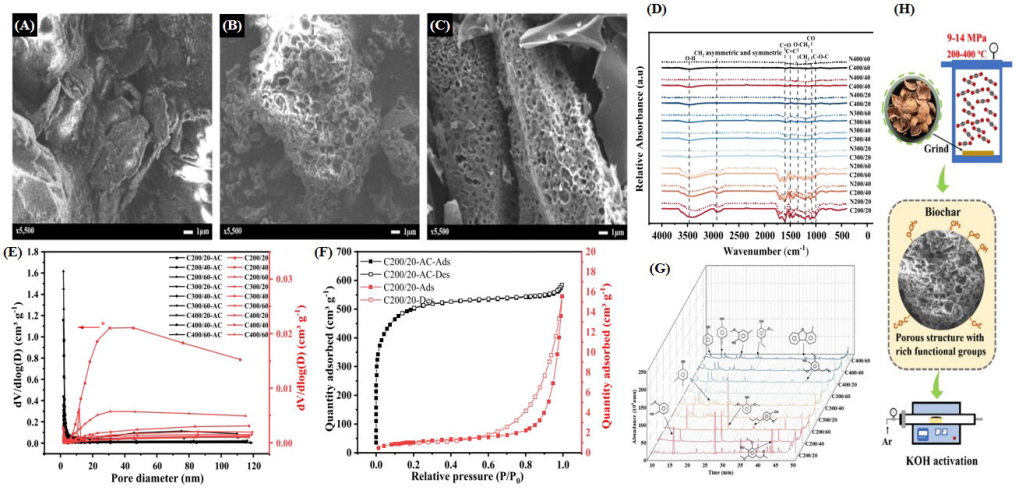

Figure 24. SEM images of solid residues (magnification = 5500). (**A**) WS, (**B**) C200/60, and (**C**) C200/60-AC. (**D**) FT-IR spectra of char in SC-CO_2 and N_2 atmosphere. (**E**) Pore size distribution of char and activated carbon. (**F**) N_2 adsorption and desorption isotherms of C200/20 and C200/20-AC. (**G**) GC-MS results of the liquid products of the SC-CO_2 pretreatment under different conditions; (**H**) Graphical depiction of the synthesis process. Reprinted with permission from [141].

From the pore size distribution diagram (e) of the supercritical CO_2-pretreated samples and AC, it can be seen that the pore structure of the lower temperature-pretreated carbon is more developed, with pore diameters in the range of 10–100 nm and with a small number of microporous structures with pore diameters less than 2 nm. The pore structure of the high temperature-pretreated carbon is relatively undeveloped, but the pore size distribution is uniform, and the micropores and mesopores are uniformly distributed. The isothermal adsorption curves of C200/20 and C200/20-AC are shown in Figure 24F, and the isothermal adsorption curve of C200/20 is consistent with the characteristics of the

isothermal adsorption curves of type III, which indicates that the material is nonporous or macroporous in structure. The curve lacks an inflection point, indicating that there is no recognizable monolayer formation, the interaction between the adsorbent material and the adsorbent gas is relatively weak, and the sample shows a limited adsorption capacity at the saturation pressure point (P/P_0). The isothermal adsorption curve of the C200/20-AC sample is of type I, which is the curve characteristic of a typical microporous material. The sharp increase in adsorption at very low values of P/P_0 is mainly due to the enhanced interaction between the adsorbent and adsorption within the narrow micropores, resulting in the decrease in these micropores at very low relative pressures. The saturation of adsorption is due to the volume limitation of the micropores into which the adsorbed gas enters and not due to the internal surface area. At saturation pressure ($P/P_0 > 0.99$), the condensation of adsorption may occur, leading to an upward turn of the curve, and the results indicate that the adsorption capacity of AC is significantly better than that of the pretreated charcoal. Charcoal functional groups were characterized using FT-IR tests as a way to explore the optimal synthesis conditions, and the results are shown in Figure 24D. The functional groups were most structurally enriched at a pretreatment temperature of 200 °C, and their structures remained essentially unchanged with the increase in the pretreatment time. The absorption peaks appearing in the 3600–3000 cm^{-1} spectral band were due to O-H stretching vibrations. The peaks associated with cellulose, such as the -CH_2 oscillation peak (1320 cm^{-1}), the C-O-C asymmetric stretching peak at the pyranose ring (1153 cm^{-1}), and the C-O-C stretching vibration peak (1031 cm^{-1}), disappeared after pretreatments at 300 °C and 400 °C, indicating complete decomposition.

Ruyi Fang and colleagues [50] similarly developed a porous biomass template derived from rice husks (RHs) through a supercritical fluid-assisted approach, aimed at creating a unique, highly loaded selenium three-dimensional porous cathode material. The preparation process is illustrated in Figure 25A, where rice husks were immersed in HCl for 12 h and subsequently heat-treated at 120 °C for 3 h to obtain SiOC intermediates. The activated 3D porous material (ARC-SiOC) was synthesized by mixing SiOC with KOH at a 3:1 ratio and calcining at 350 °C for 1.5 h and 700 °C for 2 h. Se and ARC-SiOC (ARC, activated rice carbon) powders were then placed in a stainless-steel milling flask and pressurized with CO_2 until the internal pressure reached 8.5 MPa. Ball milling and grinding were conducted at 32 °C and 350 rpm for 12 h. The resulting samples were heat-treated at 260 °C under an argon atmosphere for 6 h to obtain the selenium-loaded 3D porous bio-carbon material (ARC-SiOC-Se). As depicted in Figure 25B,C, the surface of the SiOC samples exhibit a bamboo-like morphology with no apparent pore structure. The EDX analysis revealed that the primary components of the SiOC samples were Si, O, and C.

In contrast, the surface morphology of the ARC-SiOC samples, shown in Figure 25D,E, displayed a honeycomb-like macroporous structure. The EDX results indicate a significant reduction in the contents of Si and O, and their depletion is attributed due to the reaction between Si-O and KOH. After undergoing the supercritical CO_2 treatment, ARC-SiOC-Se retained its 3D porous morphology. The EDX results show that the content of Se is substantially higher than that of other elements, indicating that the supercritical CO_2 not only maintained the material's morphology but also successfully loaded a high content of selenium. As illustrated in Figure 25H,I, the N_2 adsorption–desorption isothermal curves and pore size distribution graphs reveal that both SiOC and ARC-SiOC samples exhibit Type-I isothermal adsorption curves, indicative of the presence of microporous and mesoporous structures, resulting in a greater absorption in the lower P/P_0 range. The pore sizes of SiOC were primarily centered at 3.97 nm, whereas the ARC-SiOC pore sizes were distributed at 2.73 nm and 3.97 nm, attributed to the activating effect of KOH on the material's structure. Notably, the disappearance of the micro–mesopore structure after selenium loading indicated the successful incorporation of selenium into the available micro–mesopores.

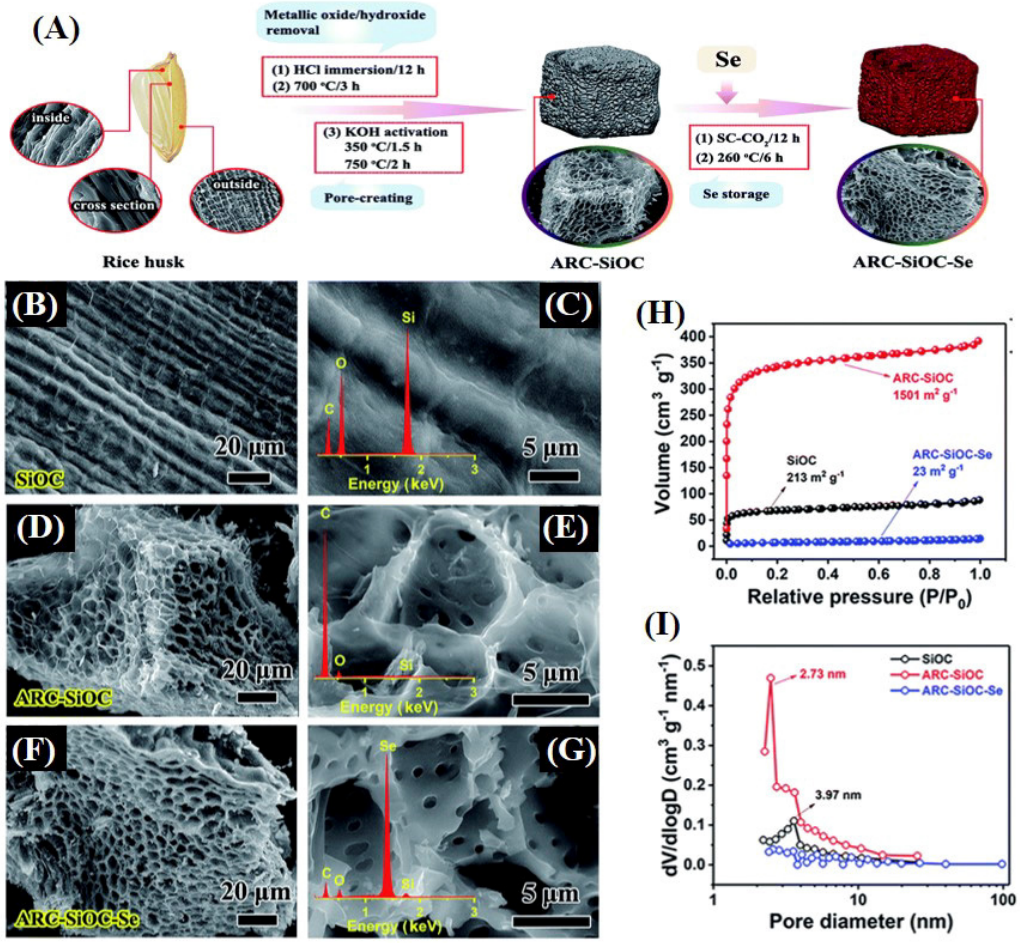

Figure 25. (**A**) Schematic of the strategy used for the synthesis of 3D porous ARC-SiOC-Se from RHs. SEM images of SiOC (**B**,**C**), ARC-SiOC (**D**,**E**), and ARC-SiOC-Se (**F**,**G**). (**H**,**I**) N_2 adsorption–desorption isotherms and pore size distribution of SiOC, ARC-SiOC, and ARC-SiOC-Se. Reprinted with the permission from [50].

The supercritical fluid-assisted method is extensively employed in the preparation of biomass template catalytic adsorbent materials for uniform surface modification without compromising the material's structure. The porous material created through supercritical fluid foaming technology features a smooth surface, uniform pore distribution, and impressive structural stability. By manipulating the process parameters, such as saturation temperature, foaming temperature, pressure, and pressure relief rate, it is possible to achieve a diverse range of pore structures, varying from 1 nm to 100 μm. This versatility allows for the production of porous materials that can consist of large-pore, mesoporous, and microporous multilayer composites, catering to various applications in different fields [85,142,143].

3.3.2. Freeze-Drying

The freeze-drying method is commonly employed for the preparation of layered porous materials, particularly those requiring high porosity and a controllable pore structure. By adjusting the temperature and pressure conditions of the sample to a critical state, the freeze-drying method facilitates the direct sublimation of ice crystals into the gas phase, thus solidifying the pore structure [144]. The customization of both the pore structure and type is intricately tied to the selection of the precursor solution. Following the dissolution of the feedstock in a specified solvent, the precise regulation of the liquid flow rate and coating rate enables the deposition of varied thicknesses of layered deposits on the substrate material. Subsequent to the rapid freezing and solidification of the layered deposits, the

freeze-drying process involves warming or depressurization to achieve a layered porous structure, culminating in a further treatment to eliminate residual impurities [143,145].

Li Xiao-Hui and colleagues [146] constructed polyoxo-metal-organic framework materials featuring both microporous and mesoporous structures through a straightforward and adaptable solvent templating approach utilizing a gel-like freeze-drying technique in a layered fashion. The preparation process is illustrated in Figure 26I. Initially, the precursor solution was synthesized using anhydrous ethanol, $Cu(OAc)_2$, PMoV, and H_3BTC and was cross-linked to produce a gel-like sample. Subsequently, after substituting deionized water and freezing the mixture, the porous metal–organic framework material was obtained via freeze-drying. In the sample name NENU-9HP-1/V, "HP" denotes the hierarchical porous structure, "1" signifies the concentration of the copper source, and "V" represents the total volume of ethanol used. Figure 26A–F reveal that the NENU-9HP-1/30 sample exhibits a small number of mesopores on its surface, with the particles being tightly packed.

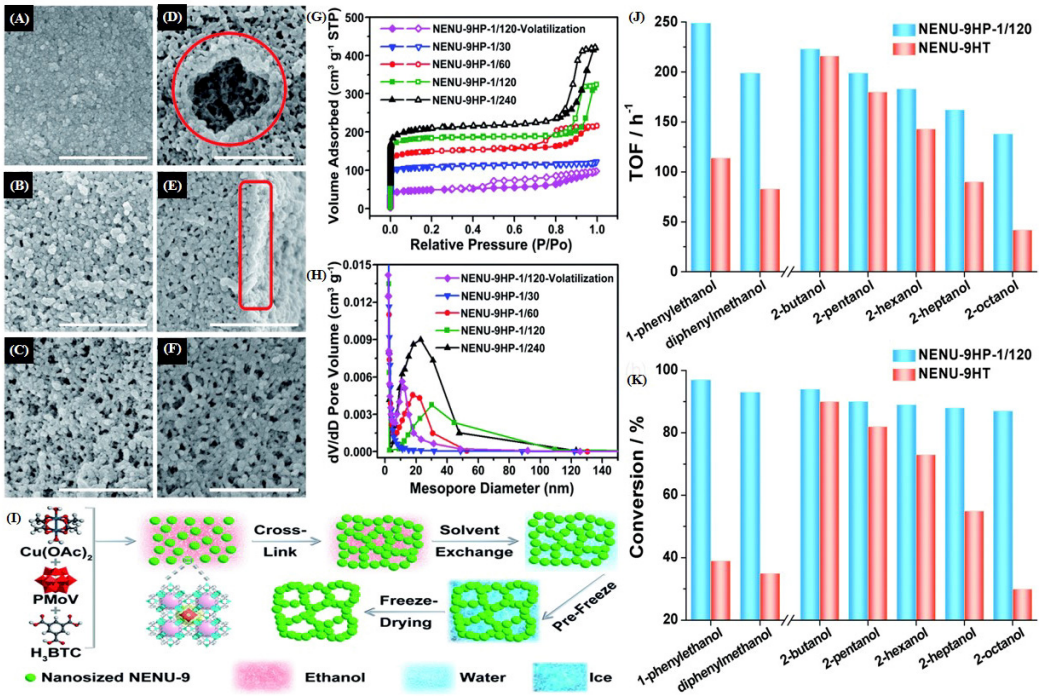

Figure 26. SEM images of (**A**) NENU-9HP-1/30, (**B**) NENU-9HP-1/60, (**C**–**E**) NENU-9HP-1/120, and (**F**) NENU-9HP-1/240. N_2 sorption isotherms (**G**) and pore size distributions of NENU-9HP-1/V (**H**). (**I**) Schematic diagram of a possible mechanism for the formation of NENU-9HP-1/V. (**J**) TOF values evaluated on the basis of the moles of the whole catalyst and reactive moles of substrates in 20 min. (**K**) Final conversions of different secondary alcohols catalyzed by NENU-9HP-1/120 and NENU-9HT. Reprinted with the permission from [146].

However, as the total volume of ethanol increases, both the number and size of the mesopores on the sample's surface significantly increase. This is due to a reduction in the reaction rate when the reactant concentration decreases, leading to the formation of numerous nanoparticles that assemble into mesoporous structures. The sample NENU-9HP-1/120 exhibits an abundance of both mesoporous and microporous structures, whereas the lower-concentration sample NENU-9HP-1/240 lacks hierarchical porous structures. Nitrogen adsorption and desorption tests were conducted on all samples, with the results presented in Figure 26G. The isothermal adsorption curve of the NENU-9HP-1/30 sample is of type I, with P/P0 < 0.1 indicating the presence of a limited number of micropores, and its pore size is primarily distributed at 12.7 nm, consistent with SEM images. The other three samples with lower concentrations (V = 60, 120, and 240) exhibited type-IV isothermal adsorption curves with a distinct hysteresis loop at high pressure, suggesting that the mesopore size gradually increases as the ethanol concentration decreases. Notably,

the NENU-9HP-1/120 sample had the largest mesopore size, with an average distribution of 30.1 nm. The pore structure of the NENU-9HP-1/120 sample is looser in the middle and tighter at the edges, attributed to volume expansion during water freezing that compresses the interconnected particles. The catalytic performance of the NENU-9HP-1/120 samples is demonstrated in Figure 26J,K, showing that the successful construction of the hierarchical porous structure significantly enhances its catalytic capabilities. The analysis of the test results indicates that the rapid reaction of the raw materials $Cu(OAc)_2$, PMoV, and H3BTC in anhydrous ethanol forms particles with an intrinsic microporous structure. During the cross-linking process, a mesoporous structure forms between the particles, primarily supported by the solvent. However, this mesoporous structure is initially unstable. In the freezing process, the expansion of freezing water extrudes the particles, stabilizing the formation of a more solid mesopore. Finally, removing the ice yields layered porous materials with a microporous-mesoporous structure.

Changxia Li and colleagues [147] successfully synthesized COF/reduced graphene oxide (rGO) aerogels utilizing the hydrothermal approach, where COF was grown directly onto the surface of two-dimensional graphene. Subsequently, ultra-lightweight aerogels featuring a layered porous structure were created in the form of three-dimensional stacks through freeze-drying. The synthesis route is illustrated in Figure 27A. Initially, the monomers diamino anthraquinone (Dp) and phenyl-toluene sulfonic acid (PTSA) were thoroughly mixed with graphene oxide (GO) to form a homogeneous precursor solution. Upon the addition of 1,3,5-tri acetaldehyde mesityl phenol (Tp), a dense and highly viscous blend was formed, followed by self-assembly during the gelation process. The mixture was then subjected to autoclaving at 120 °C for 24 h. To eliminate excess solvents, the mixture was thoroughly washed with deionized water and acetone, before being freeze-dried to yield exceptionally lightweight COF/rGO aerogels. The XRD analysis in Figure 27C confirms the presence of TpDqCOF (100) diffraction peaks at 3.4° for both COF and COF/rGO, verifying the formation of the TpDqCOF structure within the composites. Furthermore, Li conducted N_2 adsorption–desorption tests to characterize the porosities and surface areas of COF, COF/rGO, and rGO. The results, depicted in Figure 27D,E, indicate that the isothermal adsorption curve of COF is of type I. The steep rise in the curve at lower relative pressures suggests the presence of micropores, while the distinctive hysteresis loop indicates the existence of mesopores. The SEM images of COF/rGO, shown in Figure 27F–K, reveal that, as the COF content increases, the surface roughness of the samples intensifies. Additionally, a dense mesoporous structure and macroporous structure resulting from freeze-drying are observed. On the other hand, the microporous structure is considered an intrinsic aspect of the material's self-assembly process.

Weihua Gu and colleagues [148] prepared porous, ultralight carbon aerogels from pomelo peels using the freeze-drying technique combined with the calcination process. The manufacturing procedure is illustrated in Figure 28A. Initially, the pomelo peel was cleaned and placed in a freeze dryer, pre-frozen for 6 h, and subsequently dried for 48 h to produce the precursor. This precursor was then placed in a crucible and annealed at temperatures of 700 °C, 800 °C, and 900 °C for 2 h, with the resulting samples labeled as G700, G800, and G900, respectively. Figure 28B,C exhibit the morphology of the precursor after freeze-drying, revealing a complete three-dimensional porous structure devoid of fractures between the pore skeletons. Figure 28D displays the sample standing atop petals after high-temperature treatment, highlighting the aerogel's exceptional lightness. The three-dimensional porous structure of the sample remained intact after high-temperature calcination, with the pore structure becoming more compact and the pore size decreasing slightly. The mercury intrusion and extrusion curves (Figure 28K–M) of the carbon aerogels revealed total pore volumes of 3.07, 4.01, and 4.12 $mL \cdot g^{-1}$ for samples G700, G800, and G900, respectively. Their porosities were 78.70%, 83.53%, and 83.22%, respectively, indicating ultra-high porosity and lightweight characteristics.

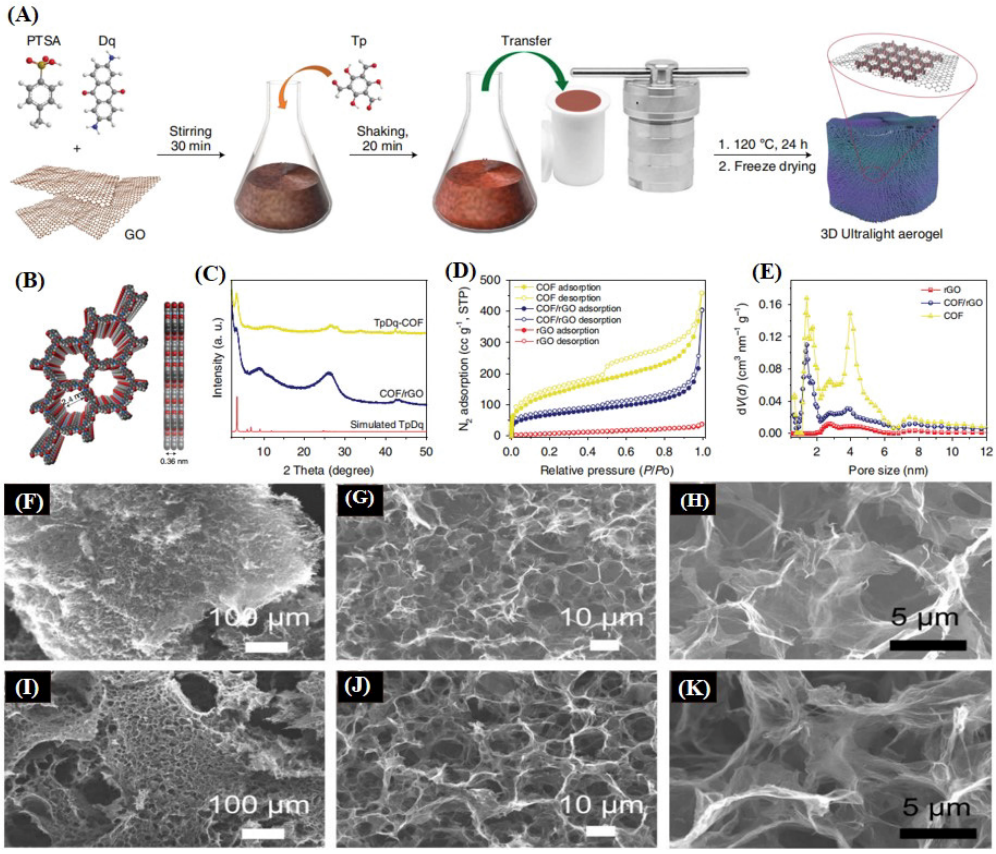

Figure 27. (**A**) Scheme of the synthetic procedure for the preparation of the COF/rGO aerogel. (**B**) Space-filled model of TpDq-COF from top and side views. (**C**) XRD pattern. (**D**) N_2 sorption isotherms and (**E**) pore size distribution of COF, COF/rGO, and Rgo. SEM images of COF/rGO aerogels with different amounts of COF: (**F**–**H**) 0.5:1 and (**I**–**K**) 2:1. Reprinted with permission from [147].

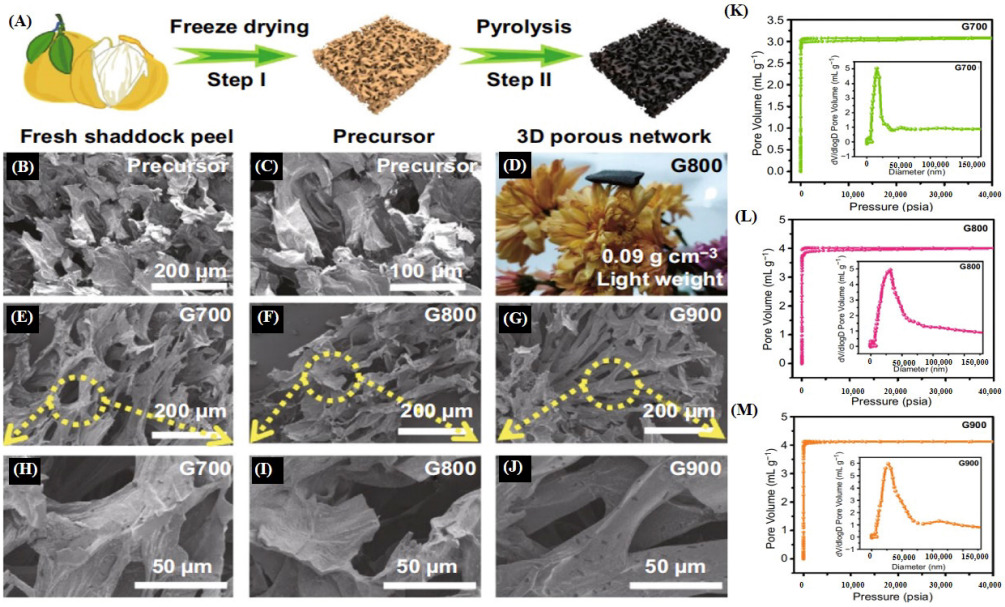

Figure 28. (**A**) Schematic of the formation process of the shaddock peel-based aerogel. (**B**,**C**) SEM images of the 3D lightweight precursor. (**D**) Digital photograph of the G800 sample on petals. (**E**–**J**) SEM images of G700, G800, and G900. (**K**–**M**) N_2 sorption isotherms and pore size distribution of G700, G800, and G900. Reprinted with the permission from [148].

By modifying factors such as the solvent type, solid-phase content, freezing rate, and sintering temperature, pore sizes ranging from 2 nm to 10 µm can be achieved. When combined with techniques like the sol–gel method and electrospinning, the freeze-drying method can effectively synthesize macroporous and mesoporous composite materials, as well as macroporous materials containing mesopores. This versatile approach enables the development of materials with tailored porosity for various applications [93,149–157].

3.3.3. Selective Leaching

The process of creating layered porous materials with diverse pore structures by regulating the solvent dissolution of the material to shape the pores is termed selective leaching [158]. This technique involves utilizing a soluble polymer with a specific level of crystallinity or distinct structural characteristics as a substrate, which is then dissolved in a solvent to create a precursor solution. Upon the desolation of the precursor solution to generate a gel, it is immersed in a suitable leaching solvent where certain portions of the polymer are selectively dissolved to establish a porous configuration. By manipulating variables such as the solvent type, leaching duration, and temperature, the size and distribution of the pores can be finely tuned. Subsequent steps involve eliminating any residual solvent, followed by drying and curing procedures to uphold the stability of the material's pore structure [159].

Shunsuke Yamada's team [160] successfully synthesized nanoporous copper through a straightforward, environmentally friendly, and rapid dealloying technique employing an ammonium chloride salt solution and magnesium as the etchant and sacrificial metal, respectively [160]. As depicted in Figure 29A, the copper foil's surface underwent a thorough cleaning process involving acetone, ethanol, and deionized water to eliminate organic impurities, followed by drying in a controlled N_2 atmosphere. Subsequently, the copper foil was sectioned, and a mixed MgCu metal layer was deposited onto its surface via ion beam sputtering. The foils were then immersed in a 10 mm ammonium chloride solution at 303 K to facilitate the dissolution of magnesium. The interaction between magnesium and the saline solution led to the formation of small bubbles on the Cu/Mg foil surface. Post-dealloying, the foils were carefully rinsed with deionized water and dried under a gentle stream of nitrogen to ensure optimal cleanliness and the preservation of the nanoporous structure.

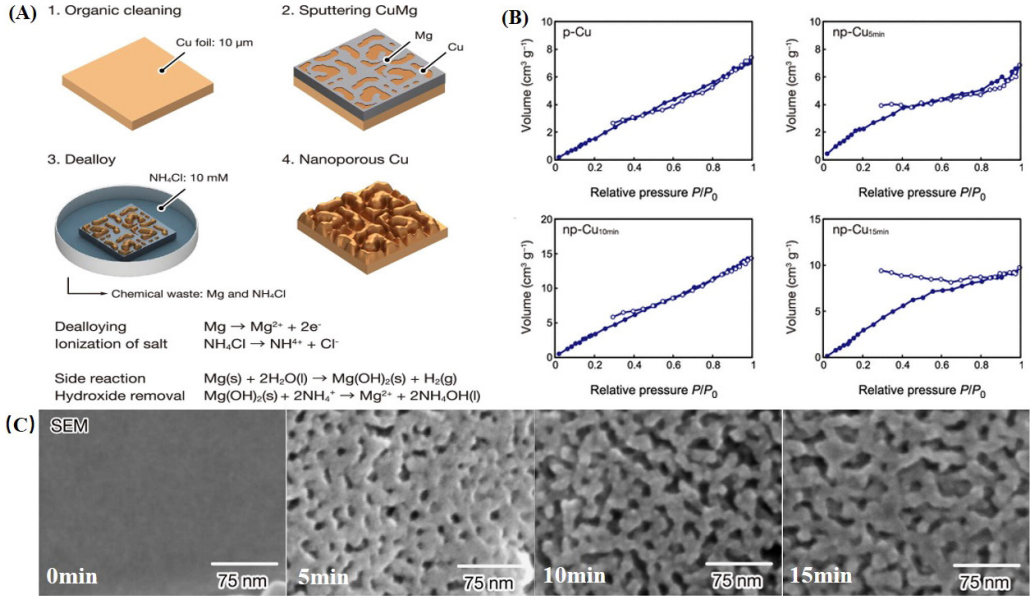

Figure 29. (**A**) Schematic showing the selective etching of the alkaline metal with saline during SEAD. (**B**) N_2 sorption isotherms of copper foils at 0, 5, 10, and 15 min. (**C**) SEM images of copper foils at 0, 5, 10, and 15 min. Reprinted with permission from [160].

The examination through scanning electron microscopy (SEM, Figure 29C) revealed the presence of minute pores (~5 nm) at the start (0 min), gradually evolving into a structured pore network as the immersion duration in the alkaline solution progressed. The nitrogen adsorption and desorption analyses conducted on samples at varying time intervals demonstrated distinct behaviors. Notably, the samples at 0 min, 5 min, and 10 min exhibited isothermal adsorption curves devoid of hysteresis loops, contrasting with the appearance of a hysteresis loop in the 15 min sample. The observed hysteresis loop, akin to type H4, signifies the emergence of a mesoporous structure in the 15-min sample. Specific surface areas for the four samples display incremental values of 6.4, 10.8, 21.1, and 24.1 $m^2 \cdot g^{-1}$, respectively, with np-Cu10 min and np-Cu15 min showcasing more than double the surface area of pristine copper. The nanoporous formation, predominantly on a singular surface and with a slim (~150 nm) profile, results in a relatively modest specific surface area. However, this can be enhanced by de-alloying bulk magnesium alloys. Moreover, the deposition of alloys through sputtering aligns well with contemporary micromachining techniques. Leveraging salt etchants facilitates the creation of nanoporous architectures on atypical substrates, encompassing flexible, stretchable, and biodegradable materials that may not withstand conventional acid/base solutions.

Prepared by Masao Miyake and his colleagues [159] through the selective etching of aluminum–zinc alloys, followed by aluminum passivation, were three-dimensional porous aluminum metallic materials featuring microporous and mesoporous structures. Miyake initially synthesized the alloys by melting high-purity aluminum (99.99%) and zinc (99.995%) at atmospheric pressure. Subsequently, the alloys underwent annealing in an H_2-Ar mixture at 200 °C for a duration of 3 h, followed by cooling to room temperature under atmospheric conditions. Observations from Figure 30A–C reveal that the alloy maintained its aluminum and zinc phases throughout the annealing process. The high temperature facilitated the diffusion of atoms into each other, resulting in the gradual growth of grains across all phases as the annealing time increased. The annealed samples were then subjected to erosion with concentrated nitric acid for 30 min and subsequently washed with deionized water and ethanol. Figure 30D–F depict the surface morphology of the eroded alloy, showcasing numerous uniformly distributed slit holes between the grains throughout the alloy phase. The pore sizes primarily range between 200 nm and 400 nm. A comparison with the size of the zinc grains indicates that pore formation occurs due to the consumption of zinc grains by the acid within the alloy phase, which is further confirmed by the XRD analysis (Figure 30H).

During the annealing process, grain growth and mutual extrusion between the aluminum and zinc phases create initial slit holes within the material before erosion, thereby establishing a certain level of initial porosity. The subsequent selective erosion of the zinc phase significantly enhances the porosity, suggesting a complex interplay between the pretreatment and erosion processes that warrants further investigation.

The selective leaching process can be controlled to produce unusual layered porous structures. The obtained porous monomers can be used as conformal coatings, porous metals, and hierarchical porous structures. Compared to other methods, there are several advantages to synthesizing materials using the leaching method. Due to the simplicity of these methods, it is expected that this simple leaching process will stimulate further research on the formation of porous materials through selective leaching methods [65,67,161–165].

The synthesis of hierarchical porous materials with multimodal and multiscale porosity is even more of interest, especially for catalysis and separation, where the optimization of diffusion and confinement mechanisms is required. The combination of the fluidized bed method with the template method or freeze-drying method can form a larger pore size structure while retaining the microporous structure of zeolite. By adjusting the introduced template or freeze-drying temperature, microporous–mesoporous or microporous–macroporous structures can be obtained [166]. The sol–gel method is generally used in combination with the heat treatment-induced phase separation method to form pore structures during gel formation and phase separation, which is usually used to pre-

pare mesoporous–macroporous structures, such as porous MOFs. The supramolecular self-assembly behavior of surfactants and copolymers can generate a structurally stable, highly ordered three-dimensional network porous structure with pore sizes in the range of 1 nm–100 µm. It is currently one of the most commonly used methods for preparing macroporous–mesoporous–microporous materials. For metal-based porous materials, selective etching is often used to etch the metal in situ to generate pores, but the resulting pore structure is uncontrollable. Micropores and mesopores provide size and shape selectivity for guest molecules, thereby enhancing the interaction between the host and guest. The presence of macropores greatly facilitates the diffusion and accessibility of active sites by guest molecules. Different pore size combinations have different mass transfer systems in practical applications, and the rational use of three different pore sizes is the only way to improve the catalytic activity of CO_2RRs [167]. Table 3 lists some hierarchically porous materials prepared using physical and chemical methods and their basic parameters for reference.

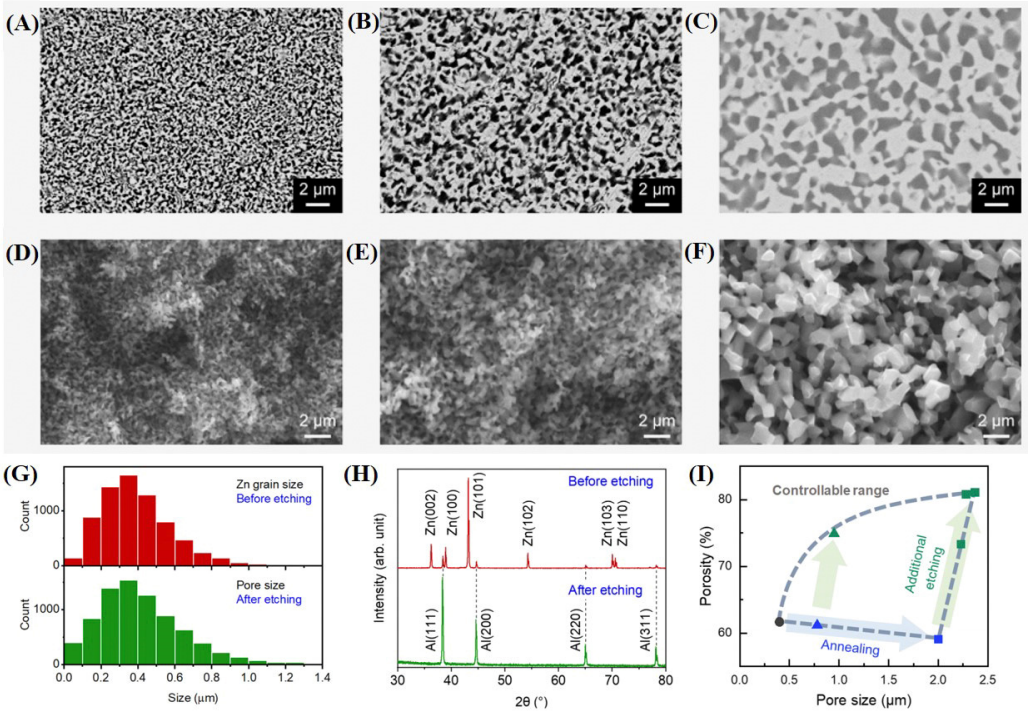

Figure 30. SEM images of cross-sections of the Al-Zn alloy foils annealed at 200 °C for (**A**) 0, (**B**), 3, and (**C**) 100 h. (**D**–**F**) Porous Al foils obtained from the alloy foils shown in (**A**–**C**), etched with concentrated nitric acid. (**G**) Histograms of Zn grain sizes in the water-cooled Al-Zn alloy and pore sizes in porous Al obtained by etching the Al-Zn alloy. (**H**) XRD patterns of Al-Zn alloy foil before etching and porous Al foil obtained from the alloy that is etched with concentrated nitric acid. (**I**) Pore size and porosity of porous Al created through a process involving both annealing and etching. Reprinted with permission from [159].

The pore size range of hierarchical porous materials prepared by basic methods is quite diverse, spanning from 1 nm to 100 nm. Different pore structures can be tailored by using various templates, allowing for the creation of macroporous structures that include mesopores or micropores. In contrast, chemical methods offer a more precise approach to regulating pore size structures. For instance, rich mesoporous structures can be formed during phase separation, and the morphology and structure of supramolecular self-assembly can be controlled based on the functional groups present in the self-assembled molecules. This makes chemical methods a preferred option for producing macroporous, mesoporous, and microporous structures. However, chemical methods also have challenges, such as poor product stability and difficulties with purification. On the other hand, physical

and chemical methods can create numerous narrow gaps, resulting in a pore structure that demonstrates good stability. These methods are commonly employed to prepare mesoporous and microporous structures. Nonetheless, accurately controlling the pore size generated by these methods remains a challenge that requires further improvement.

Table 3. Physical–chemical methods.

Method	Structure	FE (%)/Yield (μmol/g)	V_p (cm^3/g)	S_{BET} (m^2/g)	Ref.
Supercritical fluid	Macro–meso–micro	874.1 μmol/g	0.02	43.6	[142]
Supercritical fluid	Macro–meso–micro	-	0.03	32.7	[143]
Supercritical fluid	Meso–micro	66%	0.02	47	[85]
Freeze-drying	Macro–meso–micro	-	0.5	692	[156]
Freeze-drying	Macro–meso–micro	58%	0.62	721	[157]
Freeze-drying	Macro–meso–micro	81%	0.88	942.1	[93]
Freeze-drying	Macro–meso–micro	-	0.12	56.9	[154]
Selective leaching	Macro–micro	-	1,07	1046	[161]
Selective leaching	Macro–meso–micro	78%	0.15	69.2	[164]
Selective leaching	Macro–meso–micro	44%	0.31	79	[165]
Selective leaching	Macro–meso–micro	-	0.42	107.3	[67]

4. Application of Hierarchical Porous Materials in CO_2RRs

The substantial specific surface area of hierarchically pore materials offers a plethora of catalytic active sites, thereby significantly enhancing the catalytic efficiency. Additionally, their impressive mass transfer capabilities expedite the diffusion of reactants, further accelerating the reaction rate. The exceptional stability of these materials has garnered extensive attention and diverse applications in carbon dioxide reduction [168]. This section delves into the utilization of hierarchical porous materials in the electrocatalytic reduction of CO_2.

Ruru Li and colleagues [169] synthesized a nitrogen and sulfur-co-doped hierarchical porous carbon material (NSHPC) through the pyrolysis of glucosamine hydrochloride (GM) and trithiocyanuric acid (TA) precursors, utilizing silica as a hard template. This material exhibits exceptional catalytic properties in carbon dioxide reduction reactions. The synthesis process is illustrated in Figure 31A. Initially, the silica template fully reacts with the GM and TA precursors, followed by heat treatment to yield an intermediate powder. After removing the silica template using a potassium hydroxide solution (the control samples involved either no silica template for NSPC or no TA for NHPC), high-temperature carbonization results in the formation of the nitrogen and sulfur-co-doped layered porous carbon material. The scanning electron microscopy (SEM) image of NSHPC in Figure 31B reveals a fluffy, honeycomb-like porous structure. The transmission electron microscopy (TEM) image in Figure 31C demonstrates the presence of a cross-linked mesh-like porous structure within the NSHPC. The high-angle annular dark-field scanning transmission electron microscopy (HAADF-STEM) image identifies a graphitized structure at the edge of NSHPC, which is vital in electrochemical applications. The energy-dispersive X-ray (EDX) elemental distribution results in Figure 31D, E indicate the presence of corresponding nitrogen (N) and sulfur (S) elements. The isothermal adsorption curves of NSHPC and NSPC are presented in Figure 31F. The curves for NSHPC exhibit type-IV characteristics, confirming the presence of mesoporosity. The rapid uptake at $P/P0 > 0.9$ suggests the existence of pores with larger dimensions. The higher nitrogen uptake at lower relative pressures confirms the presence of micropores. The pore size distribution curve of NSHPC shows a distribution across micropores, mesopores, and macropores, further confirming its hierarchical porous structure. Similarly, Figure 31F also indicates that NSPC possesses a porous structure, primarily due to the evolution of the small molecules of hot gases during the pyrolysis of GM and TA. The X-ray diffraction (XRD) characterization of the samples in Figure 31G reveals that all three samples exhibit crystalline peaks corresponding to graphite at (002) and (101). The production of graphitic carbon atoms is further confirmed

by the two peaks present in the Raman spectra (Figure 31H) at 1344 cm^{-1} in the D band and 1592 cm^{-1} in the G band.

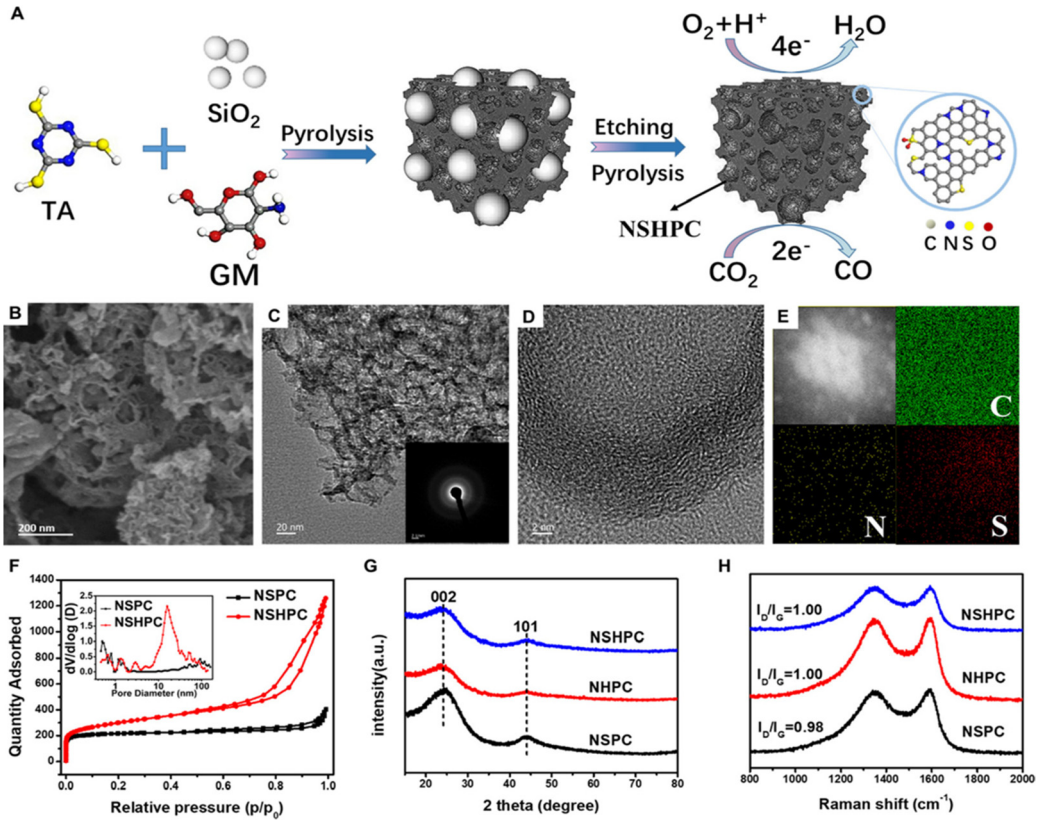

Figure 31. (**A**) Schematic illustration of the preparation of NSHPC (N, S-co-doped hierarchical porous carbon). (**B**) SEM and (**C**) TEM images of the NSHPC. (**D**) HR-TEM and (**E**) HAADF-STEM and corresponding EDS mapping images of the NSHPC. (**F**) N_2 sorption isotherms of the NSHPC and NSPC. (**G**) XRD pattern and (**H**) Raman spectra of NSHPC N, S-co-doped hierarchical porous carbon), NSPC (N, S-co-doped porous carbon), and NHPC (N-doped hierarchical porous carbon). Reprinted with permission from [169].

The XPS results depicted in Figure 32A reveal that the N 1s spectrum can be decomposed into four peaks, corresponding to typical pyridine nitrogen (398.3 eV), pyrrole nitrogen (399.5 eV), graphitic nitrogen (400.9 eV), and oxidized nitrogen (401.9 eV). The S 2p spectra illustrated in Figure 32B can be divided into three components, which align with C-SOx-C (168.4 eV), C-S-C (165.2 eV), and C=S-C (164.0 eV). Graphitic nitrogen and pyridine nitrogen play pivotal roles in catalysis, as they are considered to facilitate the formation of catalytically active sites. Similarly, thiophene sulfur also contributes to the creation of these active sites. The co-doping effect of pyridine nitrogen and C-S lowers the Gibbs free energy of the crucial intermediate *COOH in the carbon dioxide reduction reaction (CO_2RR), leading to enhanced catalytic activity. The LSV curves presented in Figure 32E demonstrate that the current density in a CO_2-saturated 0.1 M potassium bicarbonate solution is notably higher than that in a N_2-saturated solution. The Faradaic efficiency (FE) of NSHPC for CO increases from −0.4 V to −0.6 V, peaking at 87.8% at −0.6 V. In contrast, the Faradaic efficiency for H_2 is only 12%, as shown in Figure 32F. NSHPC exhibits excellent selectivity for the reduction of CO_2 to produce CO, while effectively inhibiting the hydrogen evolution reaction (HER) as a competing process. Furthermore, the current densities of both CO and H_2 increase with the rise in the voltage, as illustrated in Figure 32G. After 10 h of constant current density testing, the current density of NSHPC remained stable in a CO_2-saturated 0.1 M potassium bicarbonate solution, indicating the material's long-term stability in CO_2RRs (Figure 32H).

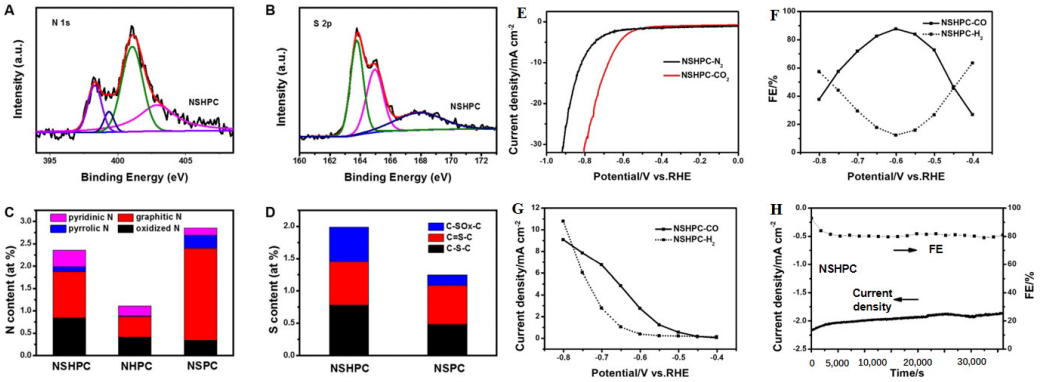

Figure 32. (**A**,**B**) HR-XPS spectra of N 1s and S 2p of the NSHPC. (**C**) N contents and relative content ratios of various N species of the NSHPC, NHPC, and NSPC. (**D**) S contents and relative content ratios of various S species of the NSHPC and NSPC. (**E**) LSV curves in N_2- and CO_2-saturated 0.1 M $KHCO_3$ using the NSHPC as a cathode. (**F**) FEs for CO and H_2 versus the potential on the NSHPC electrode between −0.8 and −0.4 V. (**G**) Partial current density of CO and H_2 at the applied cell potential for the NSHPC catalyst. (**H**) Stability test of the NSHPC for CO_2RRs operated at −0.6 V for 10 h. Reprinted with permission from [169].

Qilong Wu and his colleagues [20] crafted a hierarchical porous carbon catalyst abundant in defects, exhibiting remarkable selectivity and stability for CO_2 reduction reactions (CO_2RRs). This was achieved through the pyrolysis of ZnO@ZIF-8, utilizing potassium nitrate and ZnO nanoparticles (NPs), as illustrated in Figure 33A. Wu encapsulated potassium nitrate and ZnO NPs within ZIF-8 using an in situ encapsulation technique to synthesize ZnO@ZIF-8. The control group, designated as ZnO@ZIF-W, was subjected to washing with an ethanol–water mixture (EtOH: H_2O = 1:1) to eliminate potassium nitrate molecules. Both ZnONP@ZIF-8 and ZnONP@ZIF-W underwent heat treatment at 900 °C, resulting in the formation of delaminated defective porous carbon (DHPC) and delaminated porous carbon catalyst (HPC), respectively. The surface morphology of HPC is depicted in Figure 33B, showcasing a fractured polyhedral structure with an average size of 100 nm. Conversely, DHPC exhibits a spongy morphology with aggregated particles, as seen in Figure 33C. The TEM images of both samples reveal that DHPC possesses a more abundant mesoporous structure and numerous irregular cavities, enhancing its mass transfer capacity. These irregular cavities may introduce additional defect structures and modify the local electron density, thereby providing more catalytically active sites. The isothermal adsorption curves for both DHPC and HPC, shown in Figure 33F, exhibit type-IV characteristics, with DHPC displaying a more pronounced hysteresis loop. DHPC boasts a larger mesoporous structure, with an average pore size ranging from 5 to 20 nm, aligning with the TEM-observed morphology. Figure 33G illustrates the adsorption behavior of DHPC and HPC toward CO_2. The adsorption of CO_2 for both samples increased linearly with the rise in the relative pressure. Notably, DHPC's CO_2 uptake was 3.75 mmol/g, approximately 1.26 times that of HPC. This exceptional CO_2 adsorption capacity indicates the abundance of active sites for CO_2RRs in DHPC.

In a 0.5 M $KHCO_3$ solution saturated with CO_2, it can be observed that there is a low onset potential of −0.35 V for the DHPC sample, with the current density reaching 10 mA/cm^2 at −0.8 V. To further evaluate the CO_2 reduction reaction (CO_2RR) performance of DHPC versus HPC, Wu examined the Faradaic efficiencies of CO and H_2 in 0.5 M $KHCO_3$ (Figure 34B). For the DHPC sample, the CO Faradaic efficiency (FE) remained above 90% between −0.5 V and −0.9 V, peaking at 99.5% at −0.5 V, while the H_2 signal was negligible. In contrast, the HPC exhibited a poor CO_2RR performance, with a CO Faradaic efficiency of only 22.4% and an H_2 Faradaic efficiency of 88.9%. Furthermore, the local current density of CO for DHPC was more than ten times higher than that of HPC, indicating that the abundant defective sites favor the CO_2RR (Figure 34C). In real seawater, DHPC maintained

a CO Faradaic efficiency above 90% between −0.6 V and −0.9 V and demonstrated ultra-high selectivity for CO_2 in this complex medium.

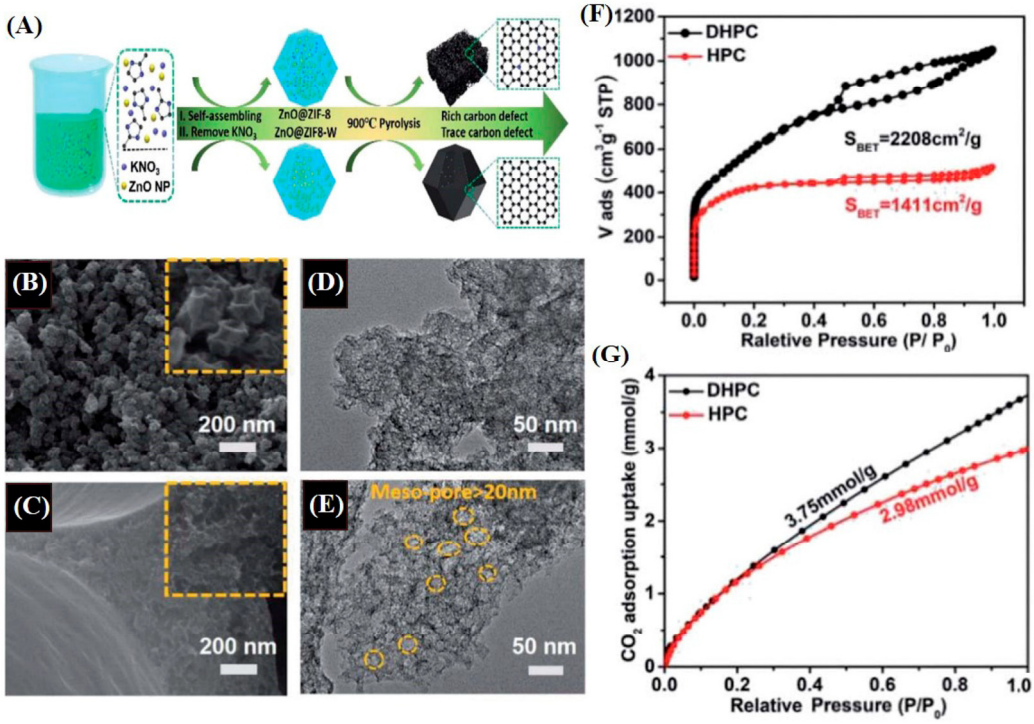

Figure 33. (**A**) Synthetic process of DHPC and HPC. (**B**) SEM image of HPC (the inset image is the magnified SEM image of HPC). (**C**) SEM image of DHPC (the inset image is the magnified SEM image of DHPC). (**D**) TEM image of HPC. (c1–c4) The element mappings of HPC. (**E**) TEM image of DHPC. (**F**) N_2 sorption isotherms of hierarchical porous carbon materials of DHPC and HPC at 77 K. (**G**) CO_2 adsorption isotherms of DHPC and HPC at 273 K. Reprinted with permission from [20].

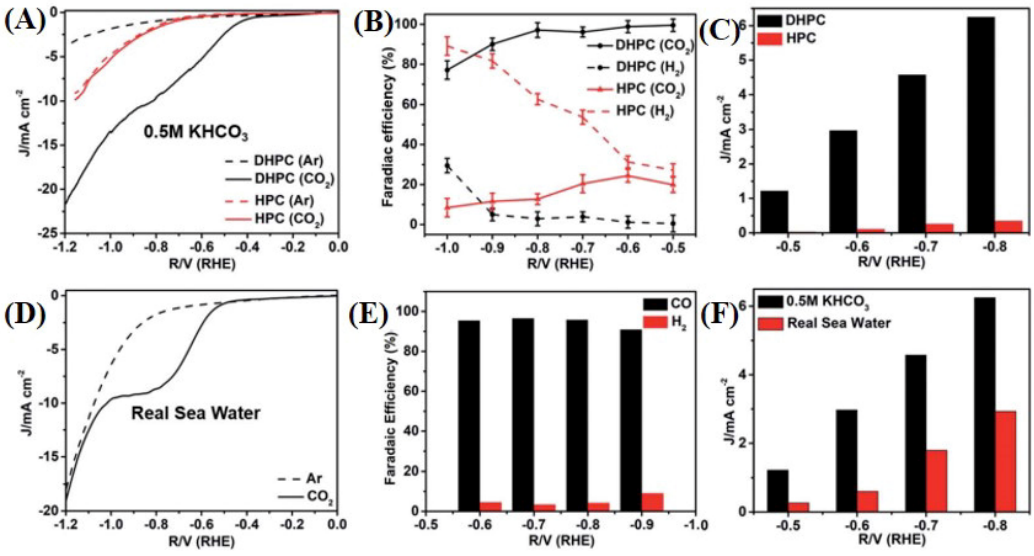

Figure 34. (**A**) LSV curves of DHPC and HPC in a 0.5 M $KHCO_3$ electrolyte. (**B**) Faraday efficiencies of DHPC and HPC in 0.5 M $KHCO_3$ at various potentials. (**C**) Partial current densities (CO) of DHPC and HPC in 0.5 M $KHCO_3$ at various potentials. (**D**) LSV curves of DHPC in a real seawater electrolyte. (**E**) Faradaic efficiencies of DHPC in real seawater at various potentials. (**F**) Partial current densities (CO) of DHPC in 0.5 M $KHCO_3$/real seawater at various potentials. Reprinted with permission from [20].

Ying Hou and colleagues [170] dispersed monomeric Ni sites on N-doped nanotubes derived from metal-organic frameworks using a self-sacrificial templating method to enhance the CO_2 reduction reaction (CO_2RR) efficiency. The process of material synthesis is illustrated in Figure 35G. ZnO@ZIF-NiZn was obtained by thermally treating ZnO and nickel nitrate hexahydrate. Following carbonization at 800 °C, residual ZnO and Ni/NiZn nanoparticles were removed through hydrochloric acid etching. The surface morphology of Ni/NCTs, as depicted in Figure 35A, reveals a rod-like structure with numerous slit voids. Additionally, Figure 35A demonstrates that the Ni/NCTs exhibit a nanorod-like structure characterized by numerous slit voids, and distinct tiny pore sizes are visible in the TEM images (Figure 35B,C). The EDX analysis under TEM confirmed the uniform distribution of Ni, C, and N elements within the Ni/NCTs. Atomic-sized Ni-related bright spots observed in the HAADF-STEM images indicate the successful synthesis of hierarchical porous materials loaded with Ni single atoms on N-doped carbon nanotubes. The Ni/NCTs exhibited excellent performance in a CO_2-saturated 0.5 M $KHCO_3$ solution, achieving a peak CO Faradaic efficiency at −0.9 V, which is approximately four times higher than that of carbon nanotubes without Ni single atoms.

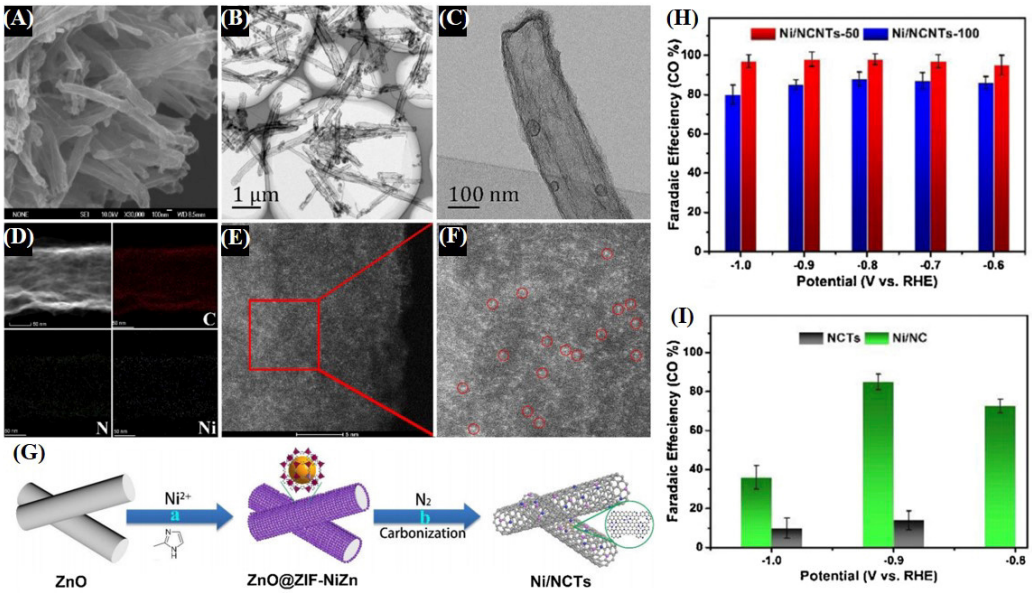

Figure 35. (**A**) SEM image, (**B**,**C**) TEM images of Ni/NCTs-50, and (**D**) its corresponding EDS mapping reveals the homogeneous distribution of Ni, C, and N elements. (**E**,**F**) Aberration-corrected HAADF-STEM image with scale bars of 5 nm and an enlarged image of Ni/NCTs-50 (partial view of Ni single atoms is highlighted by red circles; (**G**) Synthetic path diagram of Ni/NCTs; (**H**,**I**) FE_{CO} for Ni/NCTs-50, Ni/NCTs-100, Ni/NC, and NCTs in a CO_2-saturated 0.5 M $KHCO_3$ solution at various applied potentials. Reprinted with permission from [170].

Qiu-Jin Wu and his team [168] devised a solution by fabricating two-dimensional planar π-conjugated conducting COFs. They achieved this by connecting aromatic groups and incorporating the potent electron transporter tetrathiopentene (TTF) into a two-dimensional cobalt porphyrin-based covalent organic framework, known as TTF-Por(Co) -COF. This integration aimed to enhance the electrotransfer capability of TTF to metalloporphyrin, thereby boosting the CO_2RR catalytic performance.

In Figure 36A, the material's microstructure reveals a planar conjugated porous macrocyclic structure comprising compact multilayers. The pore diameters measure 1.5 nm across the layers, with a finer dimension of 0.9 nm within a single layer. This observation aligns with the pore size distribution structure depicted in Figure 36B, where each layer maintains a spacing of 3.69 Å. TTFPor(Co)-COF showcases an outstanding electrical conductivity of 1.32×10^{-7} s^{-1} and a rapid carrier mobility (μ) of 0.26 $cm^2 \cdot V^{-1} \cdot s^{-1}$, surpassing the values for COF-366-Co (6.5×10 Sm^{-1} and 0.06 $cm^2 \cdot V^{-1} \cdot s^{-1}$). The substantial BET surface area

(888 $m^2 \cdot g^{-1}$) and CO_2 uptake (22 $cm^3 \cdot g^{-1}$) of the TTF-Por(Co)-covalent organic framework at 298 K further support the advancement of CO_2RR on CO. Notably, TTF-Por(Co)-COF achieves a CO Faradaic efficiency (FE_{CO}) nearing 95% at a −0.7 V reduction potential and demonstrates a significantly elevated Jco, approximately three times greater than the current density exhibited by COF-366-Co. Refs. [171–178] include some applications of different metal-supported MOF-based catalysts in CO_2RRs.

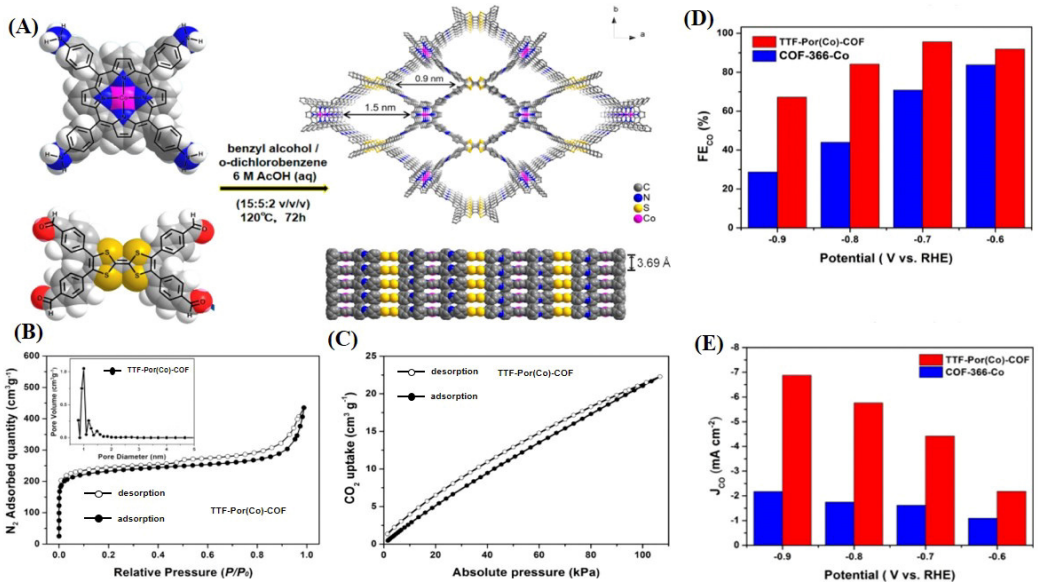

Figure 36. (**A**) The assembly of 2D TTF-Por(Co)-COF. (**B**) N_2 sorption curve for TTF-Por(Co)-COF at 77 K and pore size distribution profile (inset). (**C**) CO_2 sorption result for TTF-Por(Co)-COF at 298 K. (**D**) FE_{CO} of TTF-Por(Co)-COF. (**E**) j_{CO} of TTF-Por(Co)-COF. Reprinted with permission from [168].

Chen and his team [29] synthesized Fe-doped ZIF-8 crystals using polystyrene microspheres as templates. As shown in Figure 37A, a single-atom Fe-N-C catalyst named HP-Fe-NC was obtained by pyrolyzing a polystyrene template and carbonizing the ZIF-8 precursor at high temperatures. It can be seen in the SEM image (Figure 37B–E) that HP-Fe-NC has a uniform, layered, porous morphology, with large pore diameters uniformly distributed at 260 nm and mesopores at 42 nm and 67 nm. Moreover, according to the pore size distribution, there are abundant microporous structures on the surface of the HP-Fe-NC samples. As shown in Figure 37I–K, the Fe NC catalyst with a porous structure exhibits a lower hydrogen evolution overpotential in the LSV curve and shows a Faradaic efficiency of up to 96% and a CO local current density of -19 mA/cm^2 at lower reduction potentials. This is attributed to the abundant active sites and high specific surface area inside HP-Fe-NC. However, through double-layer testing, it was found that the electrochemically active area of HP-Fe-NC is about half of that of nonporous samples, indicating that there is another decisive factor behind the high catalytic activity of hierarchical porous samples, which is mass transfer.

To investigate the effect of the mass transfer on the catalytic activity, Chen used LBM-DEM to simulate the transport behavior of carbon dioxide molecules in electrolytes with different pore structures. Figure 38 qualitatively and quantitatively shows the velocity distribution of carbon dioxide along the *x*-axis at a time (t) of 0.01 μs for three catalysts with different pore sizes. In all three cases, the carbon dioxide molecules are uniformly distributed within the porous catalyst, and at the same saturation level, the number of carbon dioxide molecules significantly increases with the increase in the catalyst pore size. The LBMDEM simulation results at the pore scale indicate that, compared to 4 nm and 2 nm, the porous structure with a pore size of 50 nm has the highest carbon dioxide density but the lowest migration rate. The strong diffusion ability of carbon dioxide toward the inner surface of the catalyst is attributed to the larger mesopores, which create a favorable

environment with a high local carbon dioxide concentration for the conversion of carbon dioxide to CO.

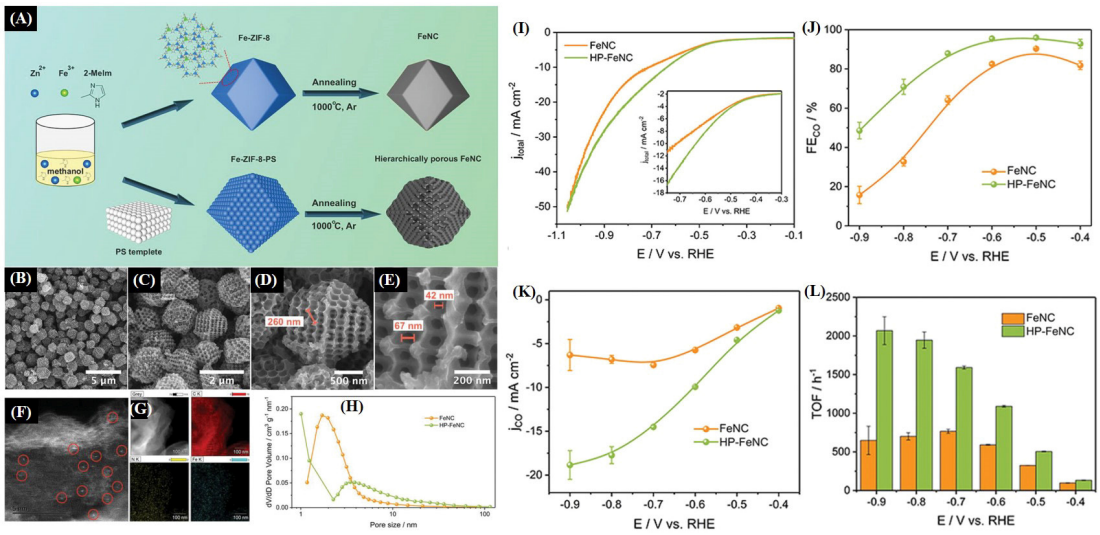

Figure 37. (**A**) Illustration of the synthesis route of Fe-NC and HP-Fe-NC. (**B**–**E**) SEM images of HP-Fe-NC. (**F**) HAADF-STEM images of HP-Fe-NC. (**G**) EDAX images of HPC-Fe-NC. (**H**) Pore size distribution of HP-Fe-NC. (**I**) LSV curves. (**J**) CO Fes. (**K**) j_{co}. (**L**) TOFs of HP-Fe-NC. Reprinted with permission from [29].

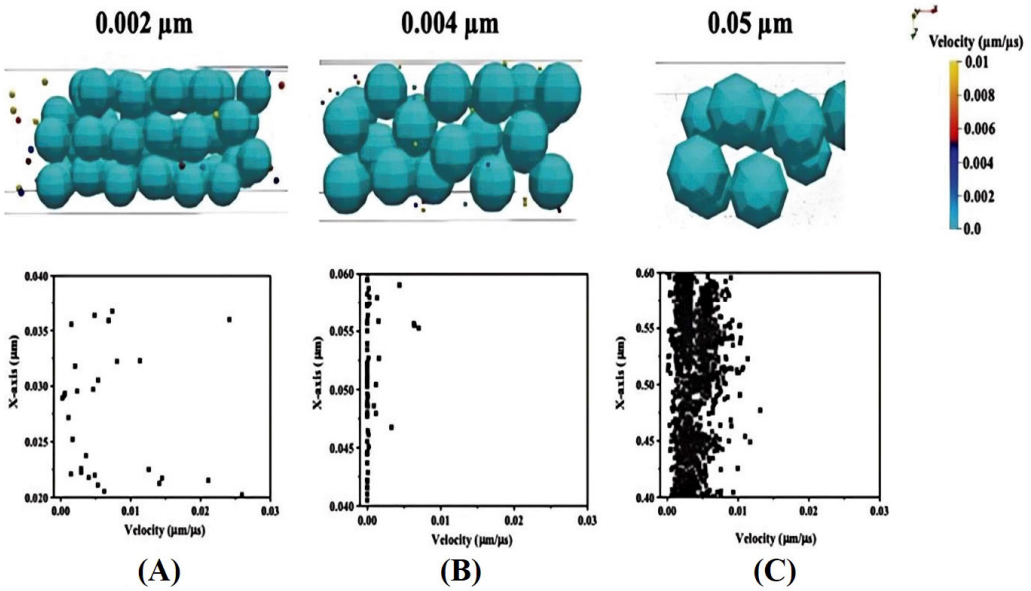

Figure 38. The velocity distribution of CO_2 particles along the *X*-axis for catalysts with different pore sizes at t = 0.01 μm: (**A**) 0.002 μm; (**B**) 0.004 μm; and (**C**) 0.05 μm. Reprinted with permission from [29].

Simeng Li et al. [31] constructed a porous carbon-supported copper selenide electrocatalyst and achieved a C2 product selectivity of up to 85.2% in CO_2RRs, with a local current density of 229.5 mA/cm^2. The synthetic pathway is shown in Figure 39A. As shown, Se was loaded onto the copper-based MOF (HKUST-1) by etching with a Se-containing acid solution, and a porous carbon-dispersed $Cu_{2-x}Se$ material was obtained by removing the template through heat treatment. As shown in Figure 39B, the sample exhibits a rough diamond-shaped octahedral structure with an average pore size of 2 nm. The ultra-small pores are caused by the carbonization of organic ligands during annealing. As shown in

TEM and HRTEM (Figure 39C,D), the $Cu_{2-x}Se$ particles are uniformly distributed throughout the carbon matrix. In Figure 39F, the XRD pattern analysis is shown, with the main diffraction peaks of the (200) and (220) crystal planes, which is consistent with the results displayed in HRTEM.

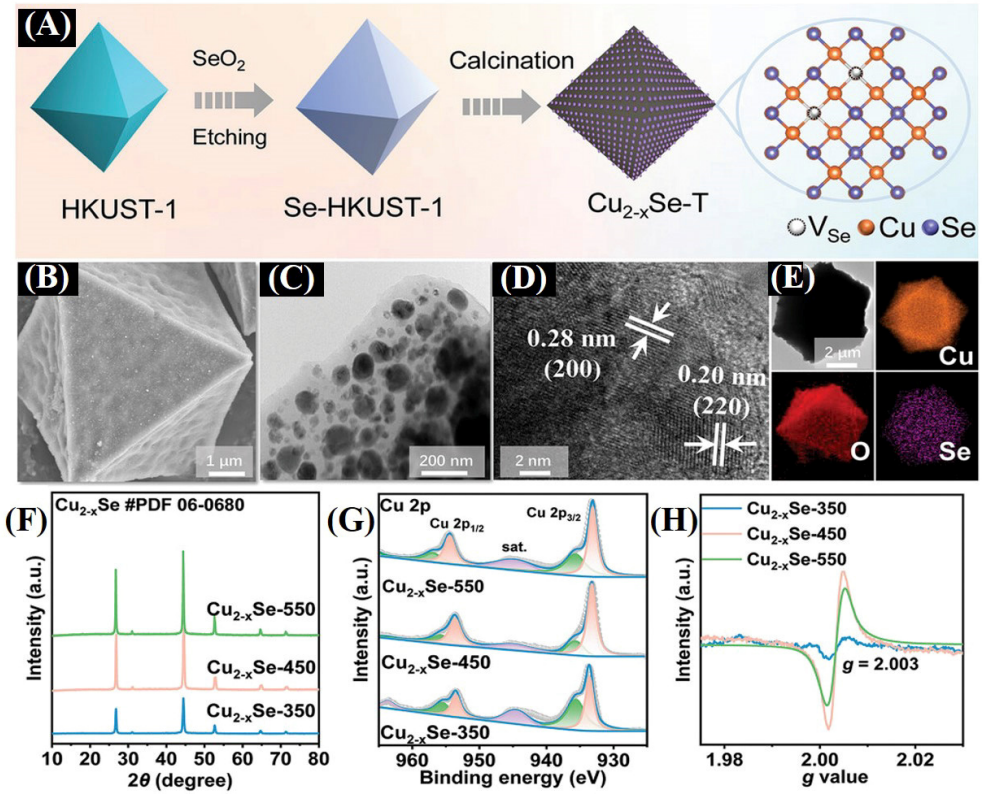

Figure 39. (**A**) Schematic showing the synthetic process of $Cu_{2-x}Se$-T. (**B**) SEM image. (**C**) TEM image. (**D**) HR-TEM image and (**E**) the elemental mapping images of $Cu_{2-x}Se$-500. (**F**) XRD pattern. (**G**) Cu 2p XPS spectra and (**H**) EPR spectra. Reprinted with permission from [31].

The CO_2RR electrochemical performance was tested in a flow cell with a uniformly loaded catalyst as the working electrode on a gas diffusion layer. As shown in Figure 40C–E, the main product of the $Cu_{2-x}Se$-450 sample in the CO_2RR is the C2 product, with a Faradaic efficiency of up to 76% for the C2 product. Selenium vacancies can shorten the Cu distance closest to adjacent Cu atoms, exposing more active Cu sites with a stronger affinity for carbon dioxide reactants and reaction intermediates, thereby reducing the C-C coupling barrier generated by C2. Compared to the sites separated near V_{Se}, the appearance of Cu_0 sites with appropriate atomic distances can stabilize the key intermediate of * OC_2H_4 through their formation.

Wei et al. [36] constructed a $Ni/Ni_3ZnC_{0.7}$ porous nitrogen-doped carbon nanofiber material using electrospinning technology for the electrochemical reduction of carbon dioxide, with a selectivity of up to 91.5% for CO. As shown in Figure 41A, $Ni(Ac)_2$, $Zn(Ac)_2$, and zinc oxide precursors were first dispersed in the one-dimensional PAN nanofibers and then annealed at 900 °C in an Ar atmosphere. During the pyrolysis process, zinc-containing substances evaporated to form porous n-doped carbon nanofibers (PNCFs). At the same time, $Ni/Ni_3ZnC_{0.7}$ heterostructure nanoparticles were formed and uniformly embedded in carbon nanofibers. From the SEM image, it can be seen (Figure 41C that the porous material exhibits a uniform fiber-like structure and a rough surface morphology, which may be due to the presence of pores formed by the evaporation of zinc during the pyrolysis process. The corresponding transmission electron microscopy (TEM) images show that nanoparticles with an average size of 12.2 nm are uniformly embedded in porous carbon fibers. Subsequently, high-resolution TEM (HR-TEM; Figure 41) was conducted. The

lattice fringes with inter-planar distances of~0.203 and~0.183 nm are attributed to the (200) plane of $Ni_3ZnC_{0.7}$ and the (111) plane of Ni, respectively. This creates different interfaces of heterostructures composed of these two phases. In addition, the energy-dispersive X-ray spectroscopy (EDS) mapping shows that N and C elements are uniform in carbon nanofibers (Figure 41G). Ni and Zn overlap with each other, consistent with the presence of nanoparticles.

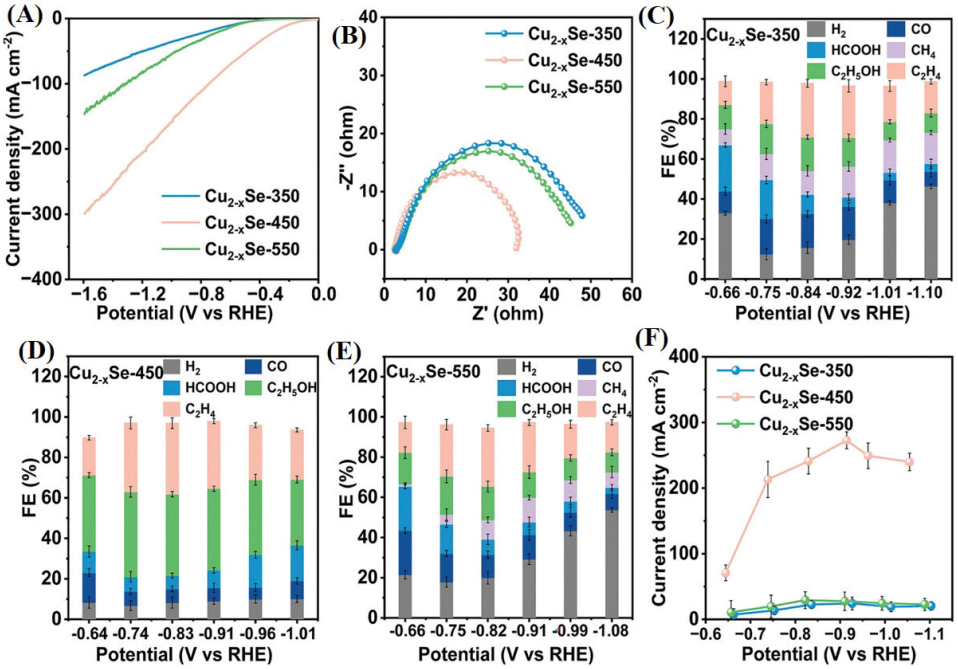

Figure 40. Effect of Se vacancies in $Cu_{2-x}Se$ on CO_2RR activity and selectivity among the samples annealed at different temperatures. (**A**) LSV curves and (**B**) Nyquist plots of $Cu_{2-x}Se$-350, $Cu_{2-x}Se$-450, and $Cu_{2-x}Se$-550. The measured FEs of (**C**) $Cu_{2-x}Se$-350, (**D**) $Cu_{2-x}Se$-450, and (**E**) $Cu_{2-x}Se$-550. (**F**) Partial current densities of C2+ (J_{C2})(C_2H_5OH and C_2H_4) were measured for the three catalysts. Reprinted with permission from [31].

Firstly, the electrocatalytic performances of PNCF, Ni-N-C, and $Ni/Ni_3ZnC_{0.7–0.4}$ were evaluated using LSV in an h-type electrochemical cell-containing CO_2-saturated 0.5 M potassium bicarbonate electrolyte. As shown in Figure 42A, $Ni/Ni_3ZnC_{0.7–0.4}$ exhibits the highest current density among all samples at all applied potentials, reaching 25.1 mA/cm^2 at −1.0 V. The FE_{CO} corresponding to $Ni/Ni_3ZnC_{0.7–0.4}$, as shown in Figure 42B, exceeds 86% within the potential range from −0.7 V to −0.95 V. Figure 42C,D shows the local current density of CO and the Tafel slope of the catalyst sample, and the results show that the optimal performance was achieved in the $Ni/Ni_3ZnC_{0.7–0.4}$ sample.

To elucidate the origin of the excellent CO_2RR performance of $Ni/Ni_3ZnC_{0.7–0.4}$, we conducted the first major calculation. The Gibbs free energy diagrams of $Ni/Ni_3ZnC_{0.7}$ and Ni in Figure 43A show that the formation of carboxyl * can serve as the RDS for both models, which is consistent with the results of the Tafel analysis. $Ni/Ni_3ZnC_{0.7}$ exhibits an endothermic energy barrier of 1.35 eV, which is significantly lower than that of the pure Ni model (1.93 eV), indicating that the RDS is promoted by heterostructures. In addition, compared to pure Ni (0.13 eV), $Ni/Ni_3ZnC_{0.7}$ has a free energy change of 0.27 eV, indicating that $Ni/Ni_3ZnC_{0.7}$ can suppress competitive HER processes (Figure 43B. In $Ni/Ni_3ZnC_{0.7}$ (Figure 43B [39], the HER process can be inhibited and suppressed. A further investigation was conducted on the difference in the charge density of carboxyl groups adsorbed on $Ni/Ni_3ZnC_{0.7}$ and pure Ni. Figure 43C shows that the heterostructure exhibits a strong electron density consumption and accumulation, indicating an enhanced charge transfer compared to pure Ni. In addition, the calculated density of states (DOS) indicates that the d

band center of Ni/$Ni_3ZnC_{0.7}$ increases by 0.14 eV after the adsorption of carboxyl *, while that of the pure Ni decreases, indicating more electron transfer between Ni/$Ni_3ZnC_{0.7}$ and carboxyl *.

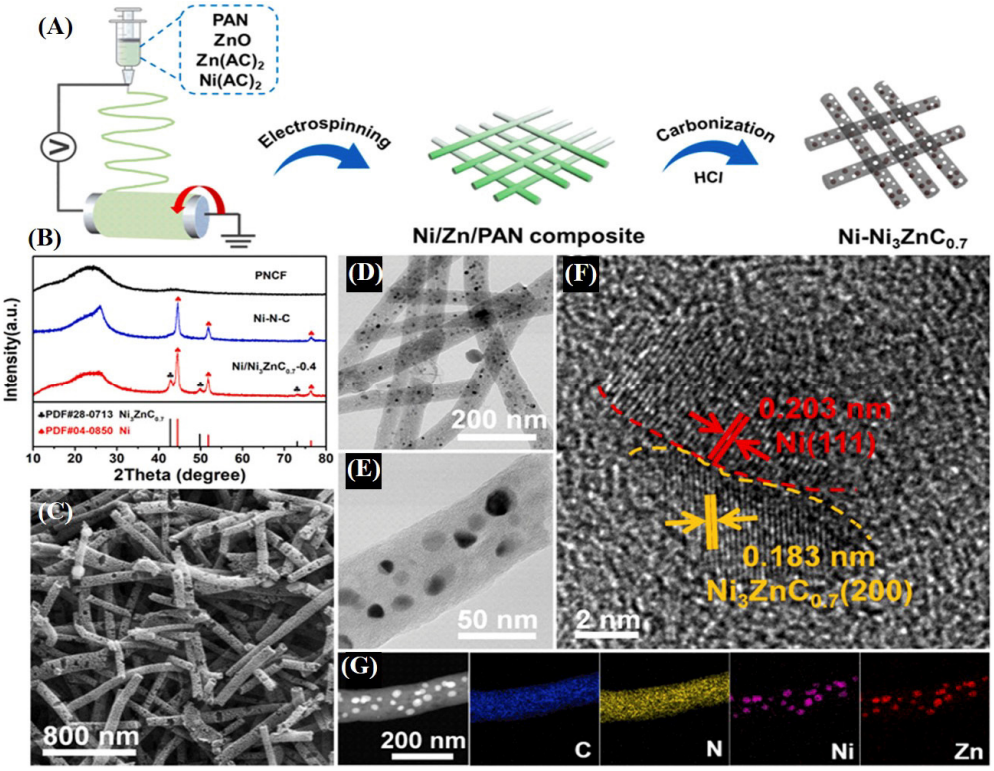

Figure 41. (**A**) Schematic illustration for the preparation of Ni/$Ni_3ZnC_{0.7}$. (**B**) XRD patterns, (**C**) SEM image, (**D**,**E**) TEM, and (**F**) HR-TEM image of Ni/$Ni_3ZnC_{0.7–0.4}$. (**G**) EDS mapping images of Ni/$Ni_3ZnC_{0.7–0.4}$. Reprinted with permission from [36].

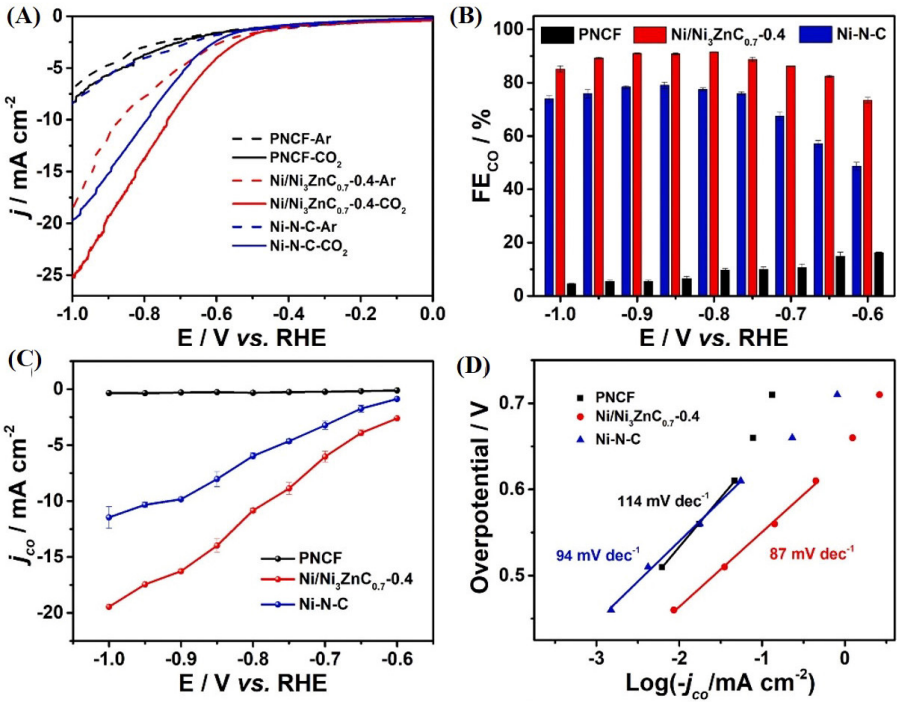

Figure 42. (**A**) LSV curves. (**B**) FE_{CO}. (**C**) J_{co}. (**D**) Tafel plots of PNCF, Ni/$Ni_3ZnC_{0.7–0.4}$, and Ni-N-C. Reprinted with permission from [36].

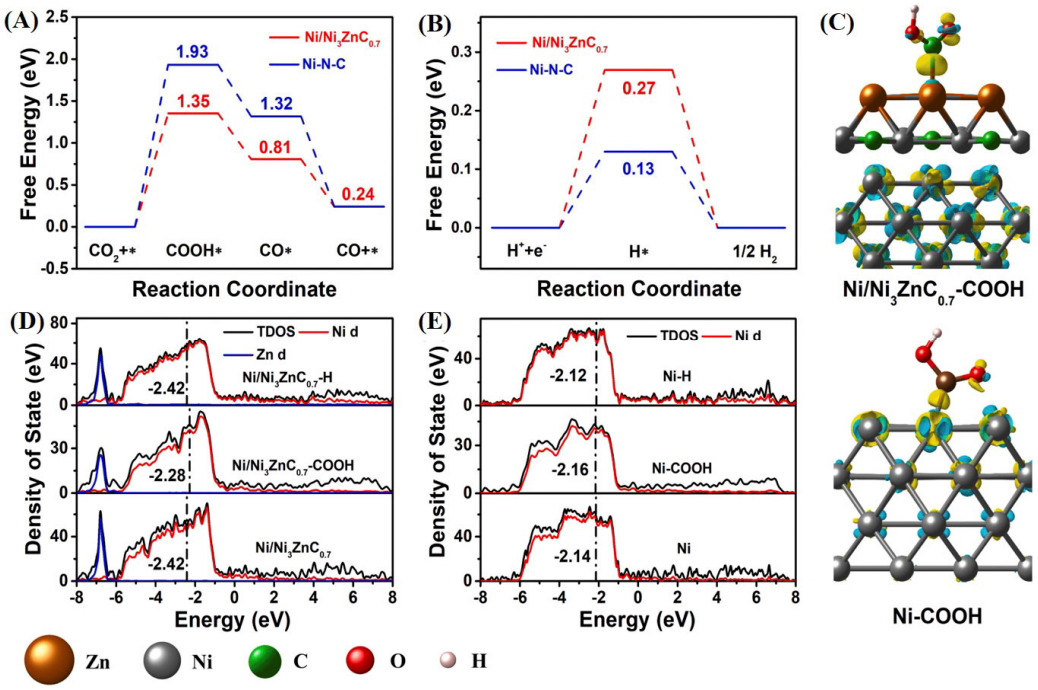

Figure 43. Gibbs free energy diagrams for (**A**) CO_2 reduction to CO and (**B**) HER on $Ni/Ni_3ZnC_{0.7–0.4}$ and Ni-N-C. (**C**) The difference of electron density for COOH* intermediates adsorbed on $Ni/Ni_3ZnC_{0.7}$ and pure Ni. Calculated DOS and d-states of the optimized structures for (**D**) $Ni/Ni_3ZnC_{0.7}$ and (**E**) Ni-N-C. Reprinted with permission from [36].

From the current research on porous materials in CO_2RRs, we can see that, in materials with a mesoporous structure, the Faradaic efficiency of carbon dioxide increases with the increase in the mesoporous porosity [179]. The electrochemically active area of a material depends on the proportion of mesopores and micropores in the material, that is, the specific surface area of the material. The size of the electrochemically active area determines the number of catalytic active sites. The specific surface area of materials rich in micropores can reach 3000 times that of conventional materials, and the catalytic active sites are 20 times that of conventional materials. Such a large number of catalytic active sites is a necessary condition for achieving a high performance. However, there is still a lack of research on the coupling mechanism between the mass transfer effect brought by mesopores and the number of catalytic active sites. Maintaining the high conversion rates of CO_2RRs while improving the selectivity of specific products is currently a major challenge [180,181].

5. Conclusions

This paper provides a comprehensive review of the structural characteristics, synthesis techniques, and current applications of hierarchical porous catalytic materials in CO_2 reduction reactions. Moreover, the electrochemical reduction mechanisms of CO_2 over metal oxides and metallic catalysts have been fully elucidated, with a special focus on the key role of mesopores in hierarchical porous materials for promoting an efficient diffusion of CO_2 molecules toward the inner surface of the catalyst, as well as highlighting the micropores' contribution to the distribution of catalytic active sites. In the third section, we mainly discussed different synthesis methods, and self-assembly based on the supramolecular host–guest self-assembly effect is currently the most promising synthesis method. The self-assembly method can regulate the intermolecular forces to control the pore structure, with a wide range of pore sizes (1 nm–100 μm) and highly ordered synthesized pore sizes. Adding different functional groups results in porous materials with different properties, such as introducing hydroxyl groups to obtain hydrophilic materials. The Faradaic efficiency of CO_2RR products increases with the increase in the mesoporous porosity (over 96%), and micropores provide 20 times the number of catalytic active sites for the catalyst

as nonporous catalysts. However, the optimal matching mechanism between mesopores and micropores is currently unclear. Further research is needed to improve the catalytic performance of CO_2RRs by regulating the size ratio and porosity ratio of macropores, mesopores, and micropores. We hope that, in future research and development, there will be hierarchical porous catalytic materials that balance structural stability and mass transfer ratio while ensuring the CO_2 conversion rate and improving the selectivity of CO_2RR products. It is anticipated that this review will function as a guideline for the development of hierarchical porous materials for future investigations in CO_2RRs.

Author Contributions: Z.W. and B.-L.S. supervised the work. Y.-D.W. performed the experiments and analyzed the data. Z.-L.G., Z.W., Y.H., S.-L.L., H.-W.L. and X.-L.L., provided advices and other help with the experiments. Z.-L.G. and Z.W. co-wrote the paper. All authors discussed the results and commented on the manuscript. Z.-L.G. and Z.W. finalized the manuscript. All authors have read and agreed to the published version of the manuscript.

Funding: This work was supported by the National Key R&D Program of China (grant 2021YFE0115800); Natural Science Foundation of Hubei Province (No. 20221j0082); National Natural Science Foundation of China (Nos. 21902122, 22293020, and 22293022); Program for Changjiang Scholars and Innovative Research Team in University (IRT_15R52) of the Chinese Ministry of Education; and the Program of Introducing Talents of Discipline to Universities-Plan 111 (grant No. B20002) from the Ministry of Science and Technology and the Ministry of Education of China.

Data Availability Statement: Data will be made available upon request.

Acknowledgments: Zhao Wang acknowledges the Hubei Provincial Department of Education for the "Chutian Scholar" program and the "Wuhan Yingcai" program.

Conflicts of Interest: The authors declare no conflicts of interest.

References

1. Zhang, X.; Li, X.; Chen, D.; Cui, H.; Ge, Q. Overestimated climate warming and climate variability due to spatially homogeneous CO_2 in climate modeling over the Northern Hemisphere since the mid-19th century. *Sci. Rep.* **2019**, *9*, 17426. [CrossRef]
2. Nunes, L.J.R.; Meireles, C.I.R.; Pinto Gomes, C.J.; Almeida Ribeiro, N.M.C. Forest Contribution to Climate Change Mitigation: Management Oriented to Carbon Capture and Storage. *Climate* **2020**, *8*, 21. [CrossRef]
3. Friedlingstein, P.; Jones, M.W.; O'Sullivan, M.; Andrew, R.M.; Bakker, D.C.E.; Hauck, J.; Le Quéré, C.; Peters, G.P.; Peters, W.; Pongratz, J.; et al. Global Carbon Budget 2021. *Earth Syst. Sci. Data* **2022**, *14*, 1917–2005. [CrossRef]
4. Hasan, S.Z.; Ahmad, K.N.; Isahak, W.N.R.W.; Pudukudy, M.; Masdar, M.S.; Jahim, J.M. Synthesis, Characterisation and Catalytic Activity of NiO supported Al_2O_3 for CO_2 Hydrogenation to Carboxylic Acids: Influence of Catalyst Structure. *IOP Conf. Ser. Earth Environ. Sci.* **2019**, *268*, 012079. [CrossRef]
5. Zhou, J.; Yu, Z.; Ma, L.; Zhu, X.; Jin, S.; Du, J.; Cheng, X.; Ke, S.; Xie, G.; Cheng, Y.-B.; et al. Pure Ammonia-Fueled Roller Kiln for the Production of Ceramic Tiles: A First Demonstration. *Energy Fuels* **2024**, *38*, 22593–22604. [CrossRef]
6. Moritz, M.; Schönfisch, M.; Schulte, S. Estimating global production and supply costs for green hydrogen and hydrogen-based green energy commodities. *Int. J. Hydrogen Energy* **2023**, *48*, 9139–9154. [CrossRef]
7. Yan, J.; Zhang, Z. Carbon Capture, Utilization and Storage (CCUS). *Appl. Energy* **2019**, *235*, 1289–1299. [CrossRef]
8. Tan, X.; Sun, X.; Han, B. Ionic liquid-based electrolytes for CO_2 electroreduction and CO_2 electroorganic transformation. *Natl. Sci. Rev.* **2022**, *9*, nwab022. [CrossRef]
9. Kumaravel, V.; Bartlett, J.; Pillai, S.C. Photoelectrochemical Conversion of Carbon Dioxide (CO_2) into Fuels and Value-Added Products. *ACS Energy Lett.* **2020**, *5*, 486–519. [CrossRef]
10. Sun, K.; Fan, Z.; Ye, J.; Yan, J.; Ge, Q.; Li, Y.; He, W.; Yang, W.; Liu, C.-j. Hydrogenation of CO_2 to methanol over In2O3 catalyst. *J. CO_2 Util.* **2015**, *12*, 1–6. [CrossRef]
11. Yang, D.; Zhu, Q.; Han, B. Electroreduction of CO_2 in Ionic Liquid-Based Electrolytes. *Innovation* **2020**, *1*, 100016. [CrossRef] [PubMed]
12. Wang, X.-K.; Liu, J.; Zhang, L.; Dong, L.-Z.; Li, S.-L.; Kan, Y.-H.; Li, D.-S.; Lan, Y.-Q. Monometallic Catalytic Models Hosted in Stable Metal–Organic Frameworks for Tunable CO_2 Photoreduction. *ACS Catal.* **2019**, *9*, 1726–1732. [CrossRef]
13. Chen, C.; Sun, X.; Yan, X.; Wu, Y.; Liu, H.; Zhu, Q.; Bediako, B.B.A.; Han, B. Boosting CO_2 Electroreduction on N,P-Co-doped Carbon Aerogels. *Angew. Chem. Int. Ed.* **2020**, *59*, 11123–11129. [CrossRef] [PubMed]
14. Zhu, Q.; Ma, J.; Kang, X.; Sun, X.; Liu, H.; Hu, J.; Liu, Z.; Han, B. Efficient Reduction of CO_2 into Formic Acid on a Lead or Tin Electrode using an Ionic Liquid Catholyte Mixture. *Angew. Chem. Int. Ed.* **2016**, *55*, 9012–9016. [CrossRef] [PubMed]
15. Hepburn, C.; Adlen, E.; Beddington, J.; Carter, E.A.; Fuss, S.; Mac Dowell, N.; Minx, J.C.; Smith, P.; Williams, C.K. The technological and economic prospects for CO_2 utilization and removal. *Nature* **2019**, *575*, 87–97. [CrossRef] [PubMed]

16. Chen, L.-H. Hierarchically porous materials and green chemistry—An interview with Ming-Yuan He. *Natl. Sci. Rev.* **2020**, *7*, 1759–1761. [CrossRef]
17. Sun, K.; Cheng, T.; Wu, L.; Hu, Y.; Zhou, J.; Maclennan, A.; Jiang, Z.; Gao, Y.; Goddard, W.A.; Wang, Z. Ultrahigh Mass Activity for Carbon Dioxide Reduction Enabled by Gold–Iron Core–Shell Nanoparticles. *J. Am. Chem. Soc.* **2017**, *139*, 15608–15611. [CrossRef]
18. Ma, Y.; Zhang, H.; Lin, R.; Ai, Y.; Lan, K.; Duan, L.; Chen, W.; Duan, X.; Ma, B.; Wang, C.; et al. Remodeling nanodroplets into hierarchical mesoporous silica nanoreactors with multiple chambers. *Nat. Commun.* **2022**, *13*, 6136. [CrossRef]
19. Latif, M.N.; Wan Isahak, W.N.R.; Samsuri, A.; Hasan, S.Z.; Manan, W.N.; Yaakob, Z. Recent Advances in the Technologies and Catalytic Processes of Ethanol Production. *Catalysts* **2023**, *13*, 1093. [CrossRef]
20. Wu, Q.; Gao, J.; Feng, J.; Liu, Q.; Zhou, Y.; Zhang, S.; Nie, M.; Liu, Y.; Zhao, J.; Liu, F.; et al. A CO_2 adsorption dominated carbon defect-based electrocatalyst for efficient carbon dioxide reduction. *J. Mater. Chem. A* **2020**, *8*, 1205–1211. [CrossRef]
21. Wang, R.; Zhao, J.; Fang, Q.; Qiu, S. Advancements and applications of three-dimensional covalent organic frameworks. *Chem. Synth.* **2024**, *4*, 29. [CrossRef]
22. Ting, L.R.L.; Yeo, B.S. Recent advances in understanding mechanisms for the electrochemical reduction of carbon dioxide. *Curr. Opin. Electrochem.* **2018**, *8*, 126–134. [CrossRef]
23. Firet, N.J.; Smith, W.A. Probing the Reaction Mechanism of CO_2 Electroreduction over Ag Films via Operando Infrared Spectroscopy. *ACS Catal.* **2016**, *7*, 606–612. [CrossRef]
24. Han, N.; Ding, P.; He, L.; Li, Y.; Li, Y. Promises of Main Group Metal–Based Nanostructured Materials for Electrochemical CO_2 Reduction to Formate. *Adv. Energy Mater.* **2019**, *10*, 1902338. [CrossRef]
25. Abdinejad, M.; Subramanian, S.; Motlagh, M.K.; Noroozifar, M.; Duangdangchote, S.; Neporozhnii, I.; Ripepi, D.; Pinto, D.; Li, M.; Tang, K.; et al. Insertion of MXene-Based Materials into Cu–Pd 3D Aerogels for Electroreduction of $CO_2$to Formate. *Adv. Energy Mater.* **2023**, *13*, 2300402. [CrossRef]
26. Chen, H.; Liang, X.; Liu, Y.; Ai, X.; Asefa, T.; Zou, X. Active Site Engineering in Porous Electrocatalysts. *Adv. Mater.* **2020**, *32*, 2002435. [CrossRef]
27. Fujiwara, A.; Wang, J.; Hiraide, S.; Götz, A.; Miyahara, M.T.; Hartmann, M.; Apeleo Zubiri, B.; Spiecker, E.; Vogel, N.; Watanabe, S. Fast Gas-Adsorption Kinetics in Supraparticle-Based MOF Packings with Hierarchical Porosity. *Adv. Mater.* **2023**, *35*, 2305980. [CrossRef]
28. Jena, R.; Rahimi, F.A.; Karmakar, S.; Dey, A.; Kalita, D.; Das, T.N.; Maji, T.K. Electron Rich Guest Regulated Enhanced CO_2 Reduction in a Multivariate Porous Coordination Polymer. *Adv. Funct. Mater.* **2024**, *34*, 2407721. [CrossRef]
29. Jia, C.; Zhao, Y.; Song, S.; Sun, Q.; Meyer, Q.; Liu, S.; Shen, Y.; Zhao, C. Highly Ordered Hierarchical Porous Single-Atom Fe Catalyst with Promoted Mass Transfer for Efficient Electroreduction of CO_2. *Adv. Energy Mater.* **2023**, *13*, 2302007. [CrossRef]
30. Li, H.; Niu, J.B.; Tao, L.G.; Tan, M.C.; Low, H.Y. Cascade Reactions for Enhanced CO_2 Capture: Concurrent Optimization of Porosity and N-Doping. *Adv. Funct. Mater.* **2024**, *34*, 2415441. [CrossRef]
31. Li, S.; Yu, J.; Zhang, S.; Qiu, W.; Tang, X.; Lin, Z.; Cai, R.; Fang, Y.; Yang, S.; Cai, X. OperandoReconstruction of Porous Carbon Supported Copper Selenide Promotes the C2Production from CO_2RR. *Adv. Funct. Mater.* **2023**, *34*, 2311989. [CrossRef]
32. Li, S.; Zhang, H.; Li, S.; Wang, J.; Wang, Q.; Cheng, Z. Advances in hierarchically porous materials: Fundamentals, preparation and applications. *Renew. Sustain. Energy Rev.* **2024**, *202*, 114641. [CrossRef]
33. Ni, W.; Xue, Y.; Zang, X.; Li, C.; Wang, H.; Yang, Z.; Yan, Y.-M. Fluorine Doped Cagelike Carbon Electrocatalyst: An Insight into the Structure-Enhanced CO Selectivity for CO_2 Reduction at High Overpotential. *ACS Nano* **2020**, *14*, 2014–2023. [CrossRef]
34. Ni, Y.; Hu, R.; Cheng, Z.; Meng, F.; Sun, F. An Ice-Dissolving-Crosslinking Method for Efficient and Large-Scale Preparation of Polyelectrolyte Monoliths with Ultra-Stability in Aqueous Environments. *Adv. Funct. Mater.* **2024**, *34*, 2407268. [CrossRef]
35. Sam, D.K.; Li, H.; Xu, Y.-T.; Cao, Y. Advances in porous carbon materials for a sustainable future: A review. *Adv. Colloid Interface Sci.* **2024**, *333*, 103279. [CrossRef] [PubMed]
36. Wei, X.; Xiao, S.; Wu, R.; Zhu, Z.; Zhao, L.; Li, Z.; Wang, J.; Chen, J.S.; Wei, Z. Activating COOH* intermediate by Ni/Ni3ZnC0.7 heterostructure in porous N-doped carbon nanofibers for boosting CO_2 electroreduction. *Appl. Catal. B Environ.* **2022**, *302*, 120861. [CrossRef]
37. Zhao, D.; Li, X.; Zhang, K.; Guo, J.; Huang, X.; Wang, G. Recent advances in thermocatalytic hydrogenation of unsaturated organic compounds with Metal-Organic Frameworks-based materials: Construction strategies and related mechanisms. *Coord. Chem. Rev.* **2023**, *487*, 215159. [CrossRef]
38. Zhao, Y.; Zhu, L.; Kang, Y.; Shen, C.-H.; Liu, X.; Jiang, D.; Fu, L.; Guselnikova, O.; Huang, L.; Song, X.; et al. Nanoengineering Multilength-Scale Porous Hierarchy in Mesoporous Metal–Organic Framework Single Crystals. *ACS Nano* **2024**, *18*, 22404–22414. [CrossRef] [PubMed]
39. Ding, Y.; Wang, C.; Han, N.; Liu, M.; Zheng, R.; Chen, L.-H.; Zhong, J.; Su, B.-L. Two-dimensional hierarchically porous C3N4 for photocatalysis: Perspective and challenges. *Chem. Synth.* **2024**, *4*, 59. [CrossRef]
40. Li, W.; Wang, D.; Wang, Y.; Shi, Z.; Liu, J.; Zhang, L.; Xue, D.; Liu, Y. Biological metal–organic frameworks for natural gas purification and MTO product separation. *Chem. Synth.* **2024**, *4*, 22. [CrossRef]
41. Li, Y.; Wu, Y.; Wang, S.; Fu, Y.; Li, X.; Zeng, J.; Zhang, W.; Ma, H. Fluorinated porous organic frameworks for C2F6/CF4 gases separation. *Chem. Synth.* **2024**, *4*, 48. [CrossRef]
42. Wang, Z.; Zhang, Y.; Jiang, L.; Han, Q.; Wang, Q.; Jia, J.; Zhu, G. Post-modified porous aromatic frameworks for carbon dioxide capture. *Chem. Synth.* **2024**, *4*, 40. [CrossRef]

43. Sun, M.-H.; Zhou, J.; Hu, Z.-Y.; Chen, L.-H.; Li, L.-Y.; Wang, Y.-D.; Xie, Z.-K.; Turner, S.; Van Tendeloo, G.; Hasan, T.; et al. Hierarchical Zeolite Single-Crystal Reactor for Excellent Catalytic Efficiency. *Matter* **2020**, *3*, 1226–1245. [CrossRef]
44. Sun, M.-H.; Gao, S.-S.; Hu, Z.-Y.; Barakat, T.; Liu, Z.; Yu, S.; Lyu, J.-M.; Li, Y.; Xu, S.-T.; Chen, L.-H.; et al. Boosting molecular diffusion following the generalized Murray's Law by constructing hierarchical zeolites for maximized catalytic activity. *Natl. Sci. Rev.* **2022**, *9*, nwac236. [CrossRef] [PubMed]
45. Gao, M.; Li, H.; Yu, J.; Ye, M.; Liu, Z. Quantitative principle of shape-selective catalysis for a rational screening of zeolites for methanol-to-hydrocarbons. *AIChE J.* **2022**, *69*, e17881. [CrossRef]
46. Hu, N.; Li, X.-Y.; Liu, S.-M.; Wang, Z.; He, X.-K.; Hou, Y.-X.; Wang, Y.-X.; Deng, Z.; Chen, L.-H.; Su, B.-L. Enhanced stability of highly-dispersed copper catalyst supported by hierarchically porous carbon for long term selective hydrogenation. *Chin. J. Catal.* **2020**, *41*, 1081–1090. [CrossRef]
47. Mohan, S.; Honnappa, B.; Augustin, A.; Shanmugam, M.; Chuaicham, C.; Sasaki, K.; Ramasamy, B.; Sekar, K. A Critical Study of Cu2O: Synthesis and Its Application in CO_2 Reduction by Photochemical and Electrochemical Approaches. *Catalysts* **2022**, *12*, 445. [CrossRef]
48. Mendoza-Castro, M.J.; Serrano, E.; Linares, N.; García-Martínez, J. Surfactant-Templated Zeolites: From Thermodynamics to Direct Observation. *Adv. Mater. Interfaces* **2020**, *8*, 2001388. [CrossRef]
49. Zhao, S.; Li, H.; Zhang, W.; Wang, B.; Yang, X.; Peng, Y.; Zhang, Y.; Li, Z. Insight into Crystallization Features of MOR Zeolite Synthesized via Ice-Templating Method. *Catalysts* **2022**, *12*, 301. [CrossRef]
50. Fang, R.; Xia, Y.; Liang, C.; He, X.; Huang, H.; Gan, Y.; Zhang, J.; Tao, X.; Zhang, W. Supercritical CO_2-assisted synthesis of 3D porous SiOC/Se cathode for ultrahigh areal capacity and long cycle life Li–Se batteries. *J. Mater. Chem. A* **2018**, *6*, 24773–24782. [CrossRef]
51. He, N.; Zou, Y.; Chen, C.; Tan, M.; Zhang, Y.; Li, X.; Jia, Z.; Zhang, J.; Long, H.; Peng, H.; et al. Constructing ordered and tunable extrinsic porosity in covalent organic frameworks via water-mediated soft-template strategy. *Nat. Commun.* **2024**, *15*, 3896. [CrossRef] [PubMed]
52. Wang, J.; Zhang, C.; Bai, Y.; Li, Q.; Yang, X. Synthesis of mesoporous silica with ionic liquid surfactant as template. *Mater. Lett.* **2021**, *291*, 129556. [CrossRef]
53. Li, C.; Hu, Z.; Jiang, G.; Zhang, Y.; Wu, Z. 3D Carbon Microspheres with a Maze-Like Structure and Large Mesopore Tunnels Built from Rapid Aerosol-Confined Coherent Salt/Surfactant Templating. *Small* **2023**, *20*, 2305316. [CrossRef]
54. Feng, A.; Mi, L.; Yu, Y.; Cao, Y.; Yu, Y.; Song, L. Development of intracrystalline mesoporosity in NH4HF2-etched NaY zeolites by surfactant-templating and its effect on toluene adsorption. *Chem. Eng. J.* **2020**, *390*, 124529. [CrossRef]
55. Hasanvandian, F.; Zehtab Salmasi, M.; Moradi, M.; Farshineh Saei, S.; Kakavandi, B.; Rahman Setayesh, S. Enhanced spatially coupling heterojunction assembled from CuCo2S4 yolk-shell hollow sphere capsulated by Bi-modified TiO2 for highly efficient CO_2 photoreduction. *Chem. Eng. J.* **2022**, *444*, 136493. [CrossRef]
56. Lv, H.; Mao, Y.; Yao, H.; Ma, H.; Han, C.; Yang, Y.Y.; Qiao, Z.A.; Liu, B. Ir-Doped CuPd Single-Crystalline Mesoporous Nanotetrahedrons for Ethylene Glycol Oxidation Electrocatalysis: Enhanced Selective Cleavage of C-C Bond. *Angew. Chem. Int. Ed.* **2024**, *63*, 2400281. [CrossRef] [PubMed]
57. Qiu, P.; Yang, J.; Jiang, W.; Wang, L.; Fan, Y.; Luo, W. Interfacial engineering of core-shell structured mesoporous architectures from single-micelle building blocks. *Nano Today* **2020**, *35*, 100940. [CrossRef]
58. Sun, L.; Lv, H.; Feng, J.; Guselnikova, O.; Wang, Y.; Yamauchi, Y.; Liu, B. Noble-Metal-Based Hollow Mesoporous Nanoparticles: Synthesis Strategies and Applications. *Adv. Mater.* **2022**, *34*, 2201954. [CrossRef] [PubMed]
59. Vu, H.-T.; Harth, F.M.; Goepel, M.; Linares, N.; García-Martínez, J.; Gläser, R. Enhanced activity of a bifunctional Pt/zeolite Y catalyst with an intracrystalline hierarchical pore system in the aqueous-phase hydrogenation of levulinic acid. *Chem. Eng. J.* **2022**, *430*, 132763. [CrossRef]
60. Li, K.; Yang, J.; Gu, J. Hierarchically Porous MOFs Synthesized by Soft-Template Strategies. *Acc. Chem. Res.* **2022**, *55*, 2235–2247. [CrossRef]
61. Suresh, A.; Rowan, S.J.; Liu, C. Macroscale Fabrication of Lightweight and Strong Porous Carbon Foams through Template-Coating Pair Design. *Adv. Mater.* **2023**, *35*, 2206416. [CrossRef]
62. Wu, B.; Meng, Y.; Peng, C.; Yang, J.; Xing, S.; Wu, N.; Yin, C.; Yang, J.; Bai, S.; Tiwari, M.K. Porous bulk superhydrophobic nanocomposites for extreme environments. *Matter* **2023**, *6*, 1992–2004. [CrossRef]
63. Liu, R.-L.; Ji, W.-J.; He, T.; Zhang, Z.-Q.; Zhang, J.; Dang, F.-Q. Fabrication of nitrogen-doped hierarchically porous carbons through a hybrid dual-template route for CO_2 capture and haemoperfusion. *Carbon* **2014**, *76*, 84–95. [CrossRef]
64. Jia, J.; Wang, Y.; Feng, Y.; Hu, G.; Lin, J.; Huang, Y.; Zhang, Y.; Liu, Z.; Tang, C.; Yu, C. Hierarchically Porous Boron Nitride/HKUST-1 Hybrid Materials: Synthesis, CO_2 Adsorption Capacity, and CO_2/N2 and CO_2/CH_4 Selectivity. *Ind. Eng. Chem. Res.* **2021**, *60*, 2463–2471. [CrossRef]
65. Estevez, L.; Barpaga, D.; Zheng, J.; Sabale, S.; Patel, R.L.; Zhang, J.-G.; McGrail, B.P.; Motkuri, R.K. Hierarchically Porous Carbon Materials for CO_2 Capture: The Role of Pore Structure. *Ind. Eng. Chem. Res.* **2018**, *57*, 1262–1268. [CrossRef]
66. Luo, Z.; Lin, N.; Sun, M.; Wang, Y.; Zhu, X. Synthesis of 3D-interconnected hierarchical porous carbon from heavy fraction of bio-oil using crayfish shell as the biological template for high-performance supercapacitors. *Carbon* **2021**, *173*, 910–917. [CrossRef]
67. Zhu, J.; Zhu, S.; Cui, Z.; Li, Z.; Wu, S.; Xu, W.; Ba, T.; Liang, Y.; Jiang, H. Solvent-free one-step green synthesis of MXenes by "gas-phase selective etching". *Energy Storage Mater.* **2024**, *70*, 103503. [CrossRef]

68. Li, R.; Wang, L.; Zhou, P.; Lin, J.; Liu, Z.; Chen, J.; Zhao, D.; Huang, X.; Tao, Z.; Wang, G. Electronic state, abundance and microenvironment modulation of Ru nanoclusters within hierarchically porous UiO-66(Ce) for efficient hydrogenation of dicyclopentadiene. *Chin. J. Catal.* **2024**, *56*, 150–165. [CrossRef]
69. Li, Y.; Wu, Z.; Liu, Y.; Zhang, K.; Luo, S.; Li, W.; Liu, S. Worm-like ordered mesoporous carbon from liquefied wood: Morphological manipulation by varying hydrothermal temperature. *Aggregate* **2024**, *5*, e570. [CrossRef]
70. Min, S.; Chang, H.; Tao, H.; Wang, F. A porous carbon membrane with abundant intrinsic carbon defects as an integrated gas-diffusion electrode for CO_2 electroreduction. *J. Mater. Chem. A* **2023**, *11*, 15643–15650. [CrossRef]
71. Song, G.; Li, C.; Wang, T.; Lim, K.H.; Hu, F.; Cheng, S.; Hondo, E.; Liu, S.; Kawi, S. Hierarchical Hollow Carbon Particles with Encapsulation of Carbon Nanotubes for High Performance Supercapacitors. *Small* **2023**, *20*, 2305517. [CrossRef]
72. Taniguchi, Y.; Kokuryo, S.; Takada, R.; Yang, X.; Miyake, K.; Uchida, Y.; Nishiyama, N. Synthesis of N-doped carbon with a high concentration of pyridinic N using a zeolite template method with pyridine as the deposition source. *Carbon* **2024**, *223*, 118961. [CrossRef]
73. Xie, L.; Jin, Z.; Dai, Z.; Chang, Y.; Jiang, X.; Wang, H. Porous carbons synthesized by templating approach from fluid precursors and their applications in environment and energy storage: A review. *Carbon* **2020**, *170*, 100–118. [CrossRef]
74. Yang, Y.; Lou, J.; Zhao, Y.; Wei, J.; Zhou, Y.; Zhang, C.; Wu, M.; Zhang, Y.; Wang, Q.; Wang, L.; et al. Ice-templating co-assembly of dual-MOF superstructures derived 2D carbon nanobelts as efficient electrocatalysts. *Chem. Eng. J.* **2023**, *477*, 146900. [CrossRef]
75. Sakka, S. Birth of the sol–gel method: Early history. *J. Sol-Gel Sci. Technol.* **2021**, *102*, 478–481. [CrossRef]
76. Xiao, P.-W.; Zhao, L.; Sui, Z.-Y.; Han, B.-H. Synthesis of Core–Shell Structured Porous Nitrogen-Doped Carbon@Silica Material via a Sol–Gel Method. *Langmuir* **2017**, *33*, 6038–6045. [CrossRef] [PubMed]
77. Li, J.; Zhang, W.; Bao, A. Design of Hierarchically Structured Porous Boron/Nitrogen-Codoped Carbon Materials with Excellent Performance for CO_2 Capture. *Ind. Eng. Chem. Res.* **2021**, *60*, 2710–2718. [CrossRef]
78. Chen, H.; Zhang, P.; Duan, Y.; Zhao, C. CO_2 capture of calcium based sorbents developed by sol–gel technique in the presence of steam. *Chem. Eng. J.* **2016**, *295*, 218–226. [CrossRef]
79. Zhang, K.; Chen, H.; Zheng, Y.; Chen, Y.; Ma, M.; Wang, X.; Wang, L.; Zeng, D.; Shi, J. A facile in situ hydrophobic layer protected selective etching strategy for the synchronous synthesis/modification of hollow or rattle-type silica nanoconstructs. *J. Mater. Chem.* **2012**, *22*, 12553–12561. [CrossRef]
80. Carrington, M.E.; Rampal, N.; Madden, D.G.; O'Nolan, D.; Casati, N.P.M.; Divitini, G.; Martín-Illán, J.Á.; Tricarico, M.; Cepitis, R.; Çamur, C.; et al. Sol-gel processing of a covalent organic framework for the generation of hierarchically porous monolithic adsorbents. *Chem* **2022**, *8*, 2961–2977. [CrossRef]
81. Fijneman, A.J.; Högblom, J.; Palmlöf, M.; de With, G.; Persson, M.; Friedrich, H. Multiscale Colloidal Assembly of Silica Nanoparticles into Microspheres with Tunable Mesopores. *Adv. Funct. Mater.* **2020**, *30*, 2002725. [CrossRef]
82. Lori, O.; Zion, N.; Honig, H.C.; Elbaz, L. 3D Metal Carbide Aerogel Network as a Stable Catalyst for the Hydrogen Evolution Reaction. *ACS Catal.* **2021**, *11*, 13707–13713. [CrossRef]
83. Luo, Y.; Li, K.; Hu, Y.; Chen, T.; Wang, Q.; Hu, J.; Feng, J.; Feng, J. TiN as Radical Scavenger in Fe-N-C Aerogel Oxygen Reduction Catalyst for Durable Fuel Cell. *Small* **2024**, *20*, 2309822. [CrossRef] [PubMed]
84. Lv, C.; Huang, K.; Fan, Y.; Xu, J.; Lian, C.; Jiang, H.; Zhang, Y.; Ma, C.; Qiao, W.; Wang, J.; et al. Electrocatalytic reduction of carbon dioxide in confined microspace utilizing single nickel atom decorated nitrogen-doped carbon nanospheres. *Nano Energy* **2023**, *111*, 108384. [CrossRef]
85. Martín-Illán, J.Á.; Rodríguez-San-Miguel, D.; Castillo, O.; Beobide, G.; Perez-Carvajal, J.; Imaz, I.; Maspoch, D.; Zamora, F. Macroscopic Ultralight Aerogel Monoliths of Imine-based Covalent Organic Frameworks. *Angew. Chem. Int. Ed.* **2021**, *60*, 13969–13977. [CrossRef] [PubMed]
86. Tian, X.K.; Lin, S.C.; Yan, J.; Zhao, C.Y. Improved durability in thermochemical energy storage using Ti/Al/Mg Co-doped Calcium-based composites with hierarchical Meso/Micro pore structures. *Chem. Eng. J.* **2022**, *450*, 138142. [CrossRef]
87. Wang, Y.; Wang, H.; Li, B.; Han, P.; Qi, G.; Gao, D.; Wei, Z.; Tao, S. Facile synthesis of hierarchically porous carbon monolith without templating agent for various applications in energy and catalysis. *Carbon* **2024**, *230*, 119645. [CrossRef]
88. Wu, C.; Huang, H.; Jin, X.; Yan, X.; Wang, H.; Pan, Y.; Zhang, X.; Hong, C. Water-assisted synthesis of phenolic aerogel with superior compression and thermal insulation performance enabled by thick-united nano-structure. *Chem. Eng. J.* **2023**, *464*, 142805. [CrossRef]
89. Zhang, L.; Xia, S.; Zhang, X.; Yao, Y.; Zhang, Y.; Chen, S.; Chen, Y.; Yan, J. Low-Temperature Synthesis of Mesoporous Half-Metallic High-Entropy Spinel Oxide Nanofibers for Photocatalytic CO_2 Reduction. *ACS Nano* **2024**, *18*, 5322–5334. [CrossRef] [PubMed]
90. Jiang, Q.; Horozov, T.; Bismarck, A. One-pot approach to fabrication of porous polymers from Pickering emulsion templates. *Polymer* **2022**, *261*, 125406. [CrossRef]
91. Wen, Z.; Yang, H.; Lv, M.; Yu, C.; Li, Y. A compressible porous superhydrophobic material constructed by a multi-template high internal phase emulsion method for oil–water separation. *RSC Adv.* **2023**, *13*, 25920–25929. [CrossRef] [PubMed]
92. Choi, S.; Jeon, J.; Chae, J.; Yuk, S.; Lee, D.-H.; Doo, G.; Lee, D.W.; Hyun, J.; Kwen, J.; Choi, S.Q.; et al. Single-Step Fabrication of a Multiscale Porous Catalyst Layer by the Emulsion Template Method for Low Pt-Loaded Proton Exchange Membrane Fuel Cells. *ACS Appl. Energy Mater.* **2021**, *4*, 4012–4020. [CrossRef]

93. Hang, T.; Zhou, L.; Li, Z.; Zheng, Y.; Yao, Y.; Cao, Y.; Xu, C.; Jiang, S.; Chen, Y.; Zheng, J. Constructing gradient reflection and scattering porous framework in composite aerogels for enhanced microwave absorption. *Carbohydrate Polymers* **2024**, 329. [CrossRef]
94. Yuan, L.; Li, X.; Ge, L.; Jia, X.; Lei, J.; Mu, C.; Li, D. Emulsion Template Method for the Fabrication of Gelatin-Based Scaffold with a Controllable Pore Structure. *ACS Appl. Mater. Interfaces* **2018**, *11*, 269–277. [CrossRef] [PubMed]
95. Bai, X.; Liu, J.; Xu, Y.; Ma, Y.; Liu, Z.; Pan, J. CO_2 Pickering emulsion in water templated hollow porous sorbents for fast and highly selective uranium extraction. *Chem. Eng. J.* **2020**, *387*, 124096. [CrossRef]
96. Liu, S.; Tang, N.; Huang, H.; Zhang, X.; Lu, R.; Li, Y. Green and eco-friendly porous imprinted hydrogels with cellulose nanocrystals-based precise-designed hyperbranched sites for high-accuracy separation and purification of naringin. *Chem. Eng. J.* **2024**, *493*, 152821. [CrossRef]
97. Luo, J.; Dai, Z.; Feng, M.; Chen, X.; Sun, C.; Xu, Y. Hierarchically porous carbon derived from natural Porphyra for excellent electromagnetic wave absorption. *J. Mater. Sci. Technol.* **2022**, *129*, 206–214. [CrossRef]
98. Mudassir, M.A.; Aslam, H.Z.; Ansari, T.M.; Zhang, H.; Hussain, I. Fundamentals and Design-Led Synthesis of Emulsion-Templated Porous Materials for Environmental Applications. *Adv. Sci.* **2021**, *8*, 2102540. [CrossRef] [PubMed]
99. Mudassir, M.A.; Kousar, S.; Ehsan, M.; Usama, M.; Sattar, U.; Aleem, M.; Naheed, I.; Saeed, O.B.; Ahmad, M.; Akbar, H.F.; et al. Emulsion-derived porous carbon-based materials for energy and environmental applications. *Renew. Sustain. Energy Rev.* **2023**, *185*, 113594. [CrossRef]
100. Wang, J.; Yang, J.; Zhu, H.; Li, B.-G.; Zhu, S. In-situ construction of hierarchically porous MOF monoliths using high internal phase emulsion templates. *Chem. Eng. J.* **2023**, *456*, 141026. [CrossRef]
101. Yang, G.; Wu, F.; Wei, Z.; Yang, K.; Zhang, C.; Ma, Y.; Pan, J. Capturing lithium using functional macroporous microspheres with multiple chambers from one-step double emulsion via a tailoring supramolecular route and postsynthetic interface modification. *Chem. Eng. J.* **2020**, *389*, 124372. [CrossRef]
102. Zhao, W.; Jia, H.; Qu, J.; Yang, C.; Wang, Y.; Zhu, J.; Wu, H.; Liu, G. Sol-gel synthesis of TiO2-SiO2 hybrid films with tunable refractive index for broadband antireflective coatings covering the visible range. *J. Sol Gel Sci. Technol.* **2022**, *107*, 105–121. [CrossRef]
103. Chen, Z.; Wang, T.; Zhang, M.; Cao, G. A Phase-Separation Route to Synthesize Porous CNTs with Excellent Stability for Na + Storage. *Small* **2017**, *13*, 1604045. [CrossRef] [PubMed]
104. Sato, Y.; Kanamori, K.; Nakanishi, K. Preparation of Hierarchically Porous Niobium (V) Oxide and Alkaline Niobate Monoliths via Sol–Gel Accompanied by Phase Separation. *Chem. Mater.* **2023**, *35*, 5177–5184. [CrossRef]
105. Lin, Y.; Wang, R.; Xu, Y.; Li, D.; Ge, H. Synthesis of Porous MgF2 Coating by a Sol–Gel Method Accompanied by Phase Separation. *Coatings* **2023**, *13*, 1083. [CrossRef]
106. Jiao, F.; Shaju, K.M.; Bruce, P.G. Synthesis of Nanowire and Mesoporous Low-Temperature LiCoO2 by a Post-Templating Reaction. *Angew. Chem. Int. Ed.* **2005**, *44*, 6550–6553. [CrossRef] [PubMed]
107. Bai, Z.; Jia, K.; Zhang, S.; Lin, G.; Huang, Y.; Liu, X. Surface Segregation-Induced Superwetting Separation Membranes with Hierarchical Surface Structures and Internalized Gel Networks. *Adv. Funct. Mater.* **2022**, *32*, 2204612. [CrossRef]
108. Liu, W.; Wang, Z.; Serna, J.A.; Debastiani, R.; Gomez, J.E.U.; Lu, L.; Yang, W.; Dong, Z.; Levkin, P.A. Enhancing Temperature Responsiveness of PNIPAM Through 3D-Printed Hierarchical Porosity. *Adv. Funct. Mater.* **2024**, *34*, 2403794. [CrossRef]
109. Pradyasti, A.; Kim, H.J.; Hyun, W.J.; Kim, M.H. Cellulose/GO monolith covered with Pd–Pt bimetallic nanocrystals for continuous-flow catalytic reduction of hexavalent chromium. *Carbohydr. Polym.* **2024**, *330*, 121837. [CrossRef] [PubMed]
110. Yang, C.-y.; Zhu, G.-d.; Yi, Z.; Zhou, Y.; Gao, C.-j. Critical contributions of additives on the fabrication of asymmetric isoporous membranes from block copolymers: A review. *Chem. Eng. J.* **2021**, *424*, 128912. [CrossRef]
111. Yin, S.; Song, L.; Xia, S.; Cheng, Y.; Hohn, N.; Chen, W.; Wang, K.; Cao, W.; Hou, S.; Müller-Buschbaum, P. Key Factors for Template-Oriented Porous Titania Synthesis: Solvents and Catalysts. *Small Methods* **2020**, *4*, 1900689. [CrossRef]
112. Zheng, W.; Wang, X.; Che, R.; Li, D.; Zeng, X.; Kong, F.; Shao, L.; Li, X.; Xu, F. 3D cellulose scaffold with gradient pore structure controlled by hydrogen bond competition: Super-strength and multifunctional oil/water separation. *Carbohydr. Polym.* **2024**, *344*, 122544. [CrossRef] [PubMed]
113. Zhu, L.; Su, Y.; Liu, Z.; Fang, Y. Shape-Controlled Synthesis of Covalent Organic Frameworks Enabled by Polymerization-Induced Phase Separation. *Small* **2022**, *19*, 2205501. [CrossRef]
114. Hye Kwon, Y.; Kiang, C.; Benjamin, E.; Crawford, P.; Nair, S.; Bhave, R. Krypton-xenon separation properties of SAPO-34 zeolite materials and membranes. *AIChE J.* **2016**, *63*, 761–769. [CrossRef]
115. Yang, X.-Y.; Chen, L.-H.; Li, Y.; Rooke, J.C.; Sanchez, C.; Su, B.-L. Hierarchically porous materials: Synthesis strategies and structure design. *Chem. Soc. Rev.* **2017**, *46*, 481–558. [CrossRef] [PubMed]
116. Liu, X.; Ge, P.; Zhang, Y.; Zhang, B.; Yao, Z.; Wang, Z.; Li, X.; Hu, M. Highly Oriented Thin Membrane Fabrication with Hierarchically Porous Zeolite Seed. *Cryst. Growth Des.* **2018**, *18*, 4544–4554. [CrossRef]
117. Chen, X.; Zhou, S.; Zhang, X.; Chen, S.; Wang, L.; Zhang, C.; Gao, S.; Yu, D.; Fan, X.; Cheng, Y.; et al. Research progress on the preparation of transition metal-modified zeolite catalysts and their catalytic performance for the purification of engine exhausts. *J. Mater. Chem. A* **2024**, *12*, 16293–16328. [CrossRef]
118. Choi, O.; Veetil, K.A.; Park, C.H.; Kim, H.; Kim, T.-H. Fabrication of a high-performance MOF-COP-based porous hollow fiber membrane for carbon dioxide separation. *Chem. Eng. J.* **2024**, *497*, 154746. [CrossRef]

119. Kweon, S.; Cho, Y.; Park, J.S.; Ryu, J.; Yoo, C.G.; Min, H.-K.; Park, M.B. A nickel silicate MFI-type zeolite catalyst prepared by interzeolite transformation: Tailoring the catalytic active sites for glucose conversion. *J. Mater. Chem. A* **2024**, *12*, 20894–20909. [CrossRef]
120. Lee, S.; Park, Y.; Choi, M. Cooperative Interplay of Micropores/Mesopores of Hierarchical Zeolite in Chemical Production. *ACS Catal.* **2024**, *14*, 2031–2048. [CrossRef]
121. Lee, S.; Thuan Khiet Nguyen, T.; Kweon, S.; Park, M.B. Nickel silicate CHA-type zeolite prepared by interzeolite transformation and its catalytic activity in dry reforming of methane. *Chem. Eng. J.* **2024**, *498*, 155602. [CrossRef]
122. Liu, Z.; Cheng, X.; Muhammad, F.; Zhang, J. Preparation of hierarchically porous zeolite templated carbon from fly ash with investigation into the adsorption behavior towards volatile organic compound. *J. Environ. Chem. Eng.* **2024**, *12*, 112254. [CrossRef]
123. Lu, J.; Xu, Z.; Yue, Y.; Bao, X.; Lin, M.; Zhu, H. Pt-Zn clusters encapsulated in hierarchical MFI zeolite for efficient propane dehydrogenation. *Chem. Eng. J.* **2024**, *484*, 149369. [CrossRef]
124. Xu, W.; Chen, Y.; Niederberger, M.; Tervoort, E.; Mei, J.; Peng, D.L. Self-Assembled Preparation of Porous Nickel Phosphide Superparticles with Tunable Phase and Porosity for Efficient Hydrogen Evolution. *Small* **2024**, *20*, 2309435. [CrossRef] [PubMed]
125. Xue, W.-L.; Kolodzeiski, P.; Aucharova, H.; Vasa, S.; Koutsianos, A.; Pallach, R.; Song, J.; Frentzel-Beyme, L.; Linser, R.; Henke, S. Highly porous metal-organic framework liquids and glasses via a solvent-assisted linker exchange strategy of ZIF-8. *Nat. Commun.* **2024**, *15*, 4420. [CrossRef]
126. Zhang, Y.; Ren, Y.; Zu, Y.; Yan, K.; Luo, Y.; Xing, E.; Qin, Y.; Mei, Y.; Shu, X. Disassembly-reassembly-phosphating strategy to fabricate hydrothermally-stable hierarchical P@ZSM-5 zeolite for efficient methanol-to-propylene. *Chem. Eng. J.* **2024**, *497*, 154755. [CrossRef]
127. Sheng, N.; Xu, H.; Liu, X.; Chu, Y.; Han, S.; Meng, X.; Liu, Y.; Liu, C.; Xiao, F.-S. Self-formation of hierarchical SAPO-11 molecular sieves as an efficient hydroisomerization support. *Catal. Today* **2020**, *350*, 165–170. [CrossRef]
128. Zhang, X.; Cheng, Y.; Wang, S.; Fang, C.; Chen, J.; Li, M.; Zhao, W. Self-assembly of porous cellulose fibers and the incorporation of graphene carbon quantum dots for stable luminescence. *Carbohydr. Polym.* **2023**, *314*, 120928. [CrossRef] [PubMed]
129. Kim, S.; Ju, M.; Lee, J.; Hwang, J.; Lee, J. Polymer Interfacial Self-Assembly Guided Two-Dimensional Engineering of Hierarchically Porous Carbon Nanosheets. *J. Am. Chem. Soc.* **2020**, *142*, 9250–9257. [CrossRef]
130. Chang, H.; Liu, X.; Zhao, S.; Liu, Z.; Lv, R.; Zhang, Q.; Yi, T.F. Self-Assembled 3D N/P/S-Tridoped Carbon Nanoflower with Highly Branched Carbon Nanotubes as Efficient Bifunctional Oxygen Electrocatalyst Toward High-Performance Rechargeable Zn-Air Batteries. *Adv. Funct. Mater.* **2023**, *34*, 2313491. [CrossRef]
131. Guo, Y.; de Vasconcelos, L.S.; Manohar, N.; Geng, J.; Johnston, K.P.; Yu, G. Highly Elastic Interconnected Porous Hydrogels through Self-Assembled Templating for Solar Water Purification. *Angew. Chem. Int. Ed.* **2021**, *61*, 2114074. [CrossRef]
132. Li, C.; Li, Q.; Kaneti, Y.V.; Hou, D.; Yamauchi, Y.; Mai, Y. Self-assembly of block copolymers towards mesoporous materials for energy storage and conversion systems. *Chem. Soc. Rev.* **2020**, *49*, 4681–4736. [CrossRef] [PubMed]
133. Liu, M.; Hudson, Z.M. Macro-/mesoporous Metal–Organic Frameworks Templated by Amphiphilic Block Copolymers Enable Enhanced Uptake of Large Molecules. *Adv. Funct. Mater.* **2023**, *33*, 2214262. [CrossRef]
134. Liu, Z.; Chen, Z.; Li, M.; Li, J.; Zhuang, W.; Yang, X.; Wu, S.; Zhang, J. Construction of Single Ni Atom-Immobilized ZIF-8 with Ordered Hierarchical Pore Structures for Selective CO_2 Photoreduction. *ACS Catal.* **2023**, *13*, 6630–6640. [CrossRef]
135. Su, X.; Sun, Y.; Jin, L.; Zhang, L.; Yang, Y.; Kerns, P.; Liu, B.; Li, S.; He, J. Hierarchically porous Cu/Zn bimetallic catalysts for highly selective CO_2 electroreduction to liquid C2 products. *Appl. Catal. B Environ.* **2020**, *269*, 118800. [CrossRef]
136. Sun, H.; Tang, F.; Bi, Y.; Sun, H.; Huang, L.; Jiang, F.; Chen, L.; Li, J. Hierarchically Porous Cellulose Membrane via Self-Assembly Engineering for Ultra High-Power Thermoelectrical Generation in Natural Convection. *Adv. Funct. Mater.* **2023**, *33*, 2307960. [CrossRef]
137. Tu, S.; Su, H.; Sui, D.; He, Y.; Cheng, M.; Bai, P.; Zhang, C.; Sun, P.; Wang, C.; Jiang, J.; et al. Mesoporous carbon nanomaterials with tunable geometries and porous structures fabricated by a surface-induced assembly strategy. *Energy Storage Mater.* **2021**, *35*, 602–609. [CrossRef]
138. Zhang, T.; Li, T.; Gao, M.; Lu, W.; Chen, Z.; Ong, W.L.; Wong, A.S.W.; Yang, L.; Kawi, S.; Ho, G.W. Ligand Mediated Assembly of CdS Colloids in 3D Porous Metal–Organic Framework Derived Scaffold with Multi-Sites Heterojunctions for Efficient CO_2 Photoreduction. *Adv. Energy Mater.* **2024**, *14*, 2400388. [CrossRef]
139. Kapilov-Buchman, K.; Portal, L.; Zhang, Y.; Fechler, N.; Antonietti, M.; Silverstein, M.S. Hierarchically porous carbons from an emulsion-templated, urea-based deep eutectic. *J. Mater. Chem. A* **2017**, *5*, 16376–16385. [CrossRef]
140. Gros, Q.; Duval, J.; West, C.; Lesellier, E. On-line supercritical fluid extraction-supercritical fluid chromatography (SFE-SFC) at a glance: A coupling story. *TrAC Trends Anal. Chem.* **2021**, *144*, 116433. [CrossRef]
141. Zhuang, Z.; Liu, Y.; Wei, W.; Shi, J.; Jin, H. Preparation of biochar adsorption material from walnut shell by supercritical CO_2 pretreatment. *Biochar* **2024**, *6*, 11. [CrossRef]
142. Bousige, C.; Levitz, P.; Coasne, B. Bridging scales in disordered porous media by mapping molecular dynamics onto intermittent Brownian motion. *Nat. Commun.* **2021**, *12*, 1043. [CrossRef] [PubMed]
143. Jun, Y.-S.; Hyun, B.G.; Hamidinejad, M.; Habibpour, S.; Yu, A.; Park, C.B. Maintaining electrical conductivity of microcellular MWCNT/TPU composites after deformation. *Compos. Part B Eng.* **2021**, *223*, 109113. [CrossRef]

144. Bai, J.; Chu, J.; Yin, X.; Wang, J.; Tian, W.; Huang, Q.; Jia, Z.; Wu, X.; Guo, H.; Qin, Z. Synthesis of amidoximated polyacrylonitrile nanoparticle/graphene composite hydrogel for selective uranium sorption from saline lake brine. *Chem. Eng. J.* **2020**, *391*, 123553. [CrossRef]
145. Ju, P.; Liu, Q.; Zhang, H.; Chen, R.; Liu, J.; Yu, J.; Liu, P.; Zhang, M.; Wang, J. Hyperbranched topological swollen-layer constructs of multi-active sites polyacrylonitrile (PAN) adsorbent for uranium (VI) extraction from seawater. *Chem. Eng. J.* **2019**, *374*, 1204–1213. [CrossRef]
146. Li, X.-H.; Liu, Y.-W.; Liu, S.-M.; Wang, S.; Xu, L.; Zhang, Z.; Luo, F.; Lu, Y.; Liu, S.-X. A gel-like/freeze-drying strategy to construct hierarchically porous polyoxometalate-based metal–organic framework catalysts. *J. Mater. Chem. A* **2018**, *6*, 4678–4685. [CrossRef]
147. Li, C.; Yang, J.; Pachfule, P.; Li, S.; Ye, M.-Y.; Schmidt, J.; Thomas, A. Ultralight covalent organic framework/graphene aerogels with hierarchical porosity. *Nat. Commun.* **2020**, *11*, 4712. [CrossRef] [PubMed]
148. Gu, W.; Sheng, J.; Huang, Q.; Wang, G.; Chen, J.; Ji, G. Environmentally Friendly and Multifunctional Shaddock Peel-Based Carbon Aerogel for Thermal-Insulation and Microwave Absorption. *Nano-Micro Lett.* **2021**, *13*, 102. [CrossRef] [PubMed]
149. Liu, L.; Huang, H.; Tai, J.; Wu, X.; Guo, Z.; Shen, X.; Cui, S.; Chen, X. The catalytic activity of reduced graphene aerogel anchored with CoFe2O4 spinel via self-assembly technique for enhanced oxygen evolution reaction. *Carbon* **2024**, *219*, 118847. [CrossRef]
150. Shao, S.; Guo, C.; Wang, H.; Wang, S.; Zhao, T.; Tang, Y.; Liu, J.; Wang, F. Multifunctional graphene/Ti3C2T MXene aerogel inlaid with Ni@TiO2 core-shell microspheres for high-efficiency electromagnetic wave absorption and thermal insulation. *Chem. Eng. J.* **2024**, *488*, 150918. [CrossRef]
151. Song, Y.; Bao, J.; Hu, Y.; Xu, M.; Yang, Z.; Liu, Y.; Yang, Q.; Xiong, C.; Shi, Z. Ultra-porous cellulose nanofibril aerogel films as excellent triboelectric positive materials via direct freeze-drying of dispersion. *Nano Energy* **2022**, *103*, 107832. [CrossRef]
152. Wang, A.; Zhang, Z.; Liu, Y.; Li, Z.; Leng, J. Lightweight carbon nanotube/aramid nanofiber aerogel with superior electromagnetic wave absorption, thermal insulation, and flame resistance. *Carbon* **2024**, *225*, 119105. [CrossRef]
153. Wang, Q.; Li, L.; Tian, Y.; Kong, L.; Cai, G.; Zhang, H.; Zhang, J.; Zuo, W.; Wen, B. Shapeable amino-functionalized sodium alginate aerogel for high-performance adsorption of Cr (VI) and Cd (II): Experimental and theoretical investigations. *Chem. Eng. J.* **2022**, *446*, 137430. [CrossRef]
154. Wang, X.; Yuan, Y.; Sun, X.; Qiang, R.; Xu, Y.; Ma, Y.; Zhang, E.; Li, Y. Lightweight, Flexible, and Thermal Insulating Carbon/SiO2@CNTs Composite Aerogel for High-Efficiency Microwave Absorption. *Small* **2024**, *20*, 2311657. [CrossRef] [PubMed]
155. Xiao, H.; Lv, J.-b.; Tan, W.; He, X.; Chen, M.-h.; Zeng, K.; Hu, J.-h.; Yang, G. Ultrasound-assisted freeze-drying process for polyimide aerogels. *Chem. Eng. J.* **2022**, *450*, 138344. [CrossRef]
156. Yang, T.; Ma, C.; Lin, C.; Wang, J.; Qiao, W.; Ling, L.; Yu, Z.; Zhang, Y. Innovative fabrication of ultrasensitive and durable graphene fiber aerogel for flexible pressure sensors. *Carbon* **2024**, *229*, 119484. [CrossRef]
157. Zhou, J.; Hu, X.; Luo, Z.; Li, X.; Zhang, W.-x.; Deng, Z. Nanocellulose encapsulated nZVI@UiO-66-NH2 aerogel for high-efficiency p-chloronitrobenzene removal with selective reduction. *J. Hazard. Mater.* **2025**, *481*, 136520. [CrossRef] [PubMed]
158. Lee, G.-B.; Joo, W.-H.; Kang, H.-Y.; Lee, J.-C.; Ahn, I.-K.; Kim, J.-Y.; Kim, H.G.; Kim, M.; Nam, D.-H.; Joo, Y.-C. Fabrication of Ni Nanoparticle-Embedded Porous Carbon Nanofibers Through Selective Etching of Selectively Oxidized MgO. *Electron. Mater. Lett.* **2022**, *18*, 198–204. [CrossRef]
159. Miyake, M.; Tanaka, Y.; Ikenoue, T.; Hirato, T. Fabrication of micron-sized three-dimensional porous Al from an Al–Zn monotectoid alloy via selective etching and Al passivation. *J. Mater. Sci.* **2023**, *58*, 8169–8177. [CrossRef]
160. Yamada, S. Nanoporous Cu Prepared through Dealloying by Selectively Etching an Alkaline Metal with Saline. *ACS Appl. Nano Mater.* **2023**, *6*, 7229–7233. [CrossRef]
161. Jeoung, S.; Ju, I.T.; Kim, J.H.; Joo, S.H.; Moon, H.R. Hierarchically porous adamantane-shaped carbon nanoframes. *J. Mater. Chem. A* **2018**, *6*, 18906–18911. [CrossRef]
162. Jung, S.; Lee, J.-R.; Won, Y.; Lee, D.-H.; Park, Y.C.; Bae, Y.-S.; Kim, H. Hierarchical porous carbon beads for selective CO_2 capture. *J. CO_2 Util.* **2021**, *51*, 101659. [CrossRef]
163. Yun, Y.H.; Kim, K.; Lee, C.; An, B.-S.; Kwon, J.H.; Lee, S.; Kim, M.; Seo, J.; Park, J.H.; Kim, B.-H.; et al. Electrochemical partial reduction of Ni (OH)2 to Ni (OH)2/Ni via coupled oxidation of an interfacing NiAl intermetallic compound for robust hydrogen evolution. *J. Energy Chem.* **2023**, *82*, 560–571. [CrossRef]
164. Zhang, L.-Y.; Li, L.; Li, M.; Liu, Z.-Q.; Wei, X.-Y.; Ma, H.; Cong, X.-S. Catalytic hydrodeoxygenation of lignin enhanced by selectively etching ZSM-5. *J. Energy Inst.* **2024**, *117*, 101838. [CrossRef]
165. Zheng, K.; Benedetti, M.F.; Jain, R.; Guy, B.M.; Pollmann, K.; van Hullebusch, E.D. Selective leaching of indium from spent LCD screens by siderophore desferrioxamine E. *J. Hazard. Mater.* **2024**, *469*, 134013. [CrossRef] [PubMed]
166. Li, H.-Y.; Li, C.; Wang, Y.-Y.; Dong, W.-D.; Zhang, X.-K.; Sun, M.-H.; Li, Y.; Su, B.-L. Pore structure unveiling effect to boost lithium-selenium batteries: Selenium confined in hierarchically porous carbon derived from aluminum based MOFs. *Chem. Synth.* **2023**, *3*, 30. [CrossRef]
167. Liu, S.Y.; Sun, Q.Q.; Hang, P.Y.; Sun, X.H.; Zhou, C.Q.; Han, J.; Guo, R. β-cyclodextrin mediated construction of porous helical nanoribbons from oligoaniline derivatives. *Chem. Synth.* **2022**, *2*, 18. [CrossRef]
168. Wu, Q.-J.; Liang, J.; Huang, Y.-B.; Cao, R. Thermo-, Electro-, and Photocatalytic CO_2 Conversion to Value-Added Products over Porous Metal/Covalent Organic Frameworks. *Acc. Chem. Res.* **2022**, *55*, 2978–2997. [CrossRef] [PubMed]

169. Li, R.; Liu, F.; Zhang, Y.; Guo, M.; Liu, D. Nitrogen, Sulfur Co-Doped Hierarchically Porous Carbon as a Metal-Free Electrocatalyst for Oxygen Reduction and Carbon Dioxide Reduction Reaction. *ACS Appl. Mater. Interfaces* **2020**, *12*, 44578–44587. [CrossRef] [PubMed]
170. Hou, Y.; Liang, Y.-L.; Shi, P.-C.; Huang, Y.-B.; Cao, R. Atomically dispersed Ni species on N-doped carbon nanotubes for electroreduction of CO_2 with nearly 100% CO selectivity. *Appl. Catal. B Environ.* **2020**, *271*, 118929. [CrossRef]
171. Hou, S.-Z.; Zhang, X.-D.; Yuan, W.-W.; Li, Y.-X.; Gu, Z.-Y. Indium-Based Metal–Organic Framework for High-Performance Electroreduction of CO_2 to Formate. *Inorg. Chem.* **2020**, *59*, 11298–11304. [CrossRef] [PubMed]
172. Li, J.; Wang, C.; Wang, D.; Yang, C.; Cui, X.; Gao, X.J.; Zhang, Z. A hexacoordinated Bi3+-based ellagate MOF with acid/base resistance boosting carbon dioxide electroreduction to formate. *J. Mater. Chem. A* **2022**, *10*, 20018–20023. [CrossRef]
173. Liu, J.; Yang, D.; Zhou, Y.; Zhang, G.; Xing, G.; Liu, Y.; Ma, Y.; Terasaki, O.; Yang, S.; Chen, L. Tricycloquinazoline-Based 2D Conductive Metal–Organic Frameworks as Promising Electrocatalysts for CO_2Reduction. *Angew. Chem. Int. Ed.* **2021**, *60*, 14473–14479. [CrossRef] [PubMed]
174. Shimoni, R.; Shi, Z.; Binyamin, S.; Yang, Y.; Liberman, I.; Ifraemov, R.; Mukhopadhyay, S.; Zhang, L.; Hod, I. Electrostatic Secondary-Sphere Interactions That Facilitate Rapid and Selective Electrocatalytic CO_2 Reduction in a Fe-Porphyrin-Based Metal–Organic Framework. *Angew. Chem. Int. Ed.* **2022**, *61*, 2206085. [CrossRef]
175. Zhang, X.-D.; Huang, L.-R.; Wu, J.-X.; Gu, Z.-Y. Enhancing selectivity through decrypting the uncoordinated zirconium sites in MOF electrocatalysts. *Chem. Commun.* **2021**, *57*, 5191–5194. [CrossRef] [PubMed]
176. Wang, Y.; Feng, L.; Pang, J.; Li, J.; Huang, N.; Day, G.S.; Cheng, L.; Drake, H.F.; Wang, Y.; Lollar, C.; et al. Photosensitizer-Anchored 2D MOF Nanosheets as Highly Stable and Accessible Catalysts toward Artemisinin Production. *Adv. Sci.* **2019**, *6*, 1802059. [CrossRef] [PubMed]
177. Zhu, H.-L.; Chen, H.-Y.; Han, Y.-X.; Zhao, Z.-H.; Liao, P.-Q.; Chen, X.-M. A Porous π–π Stacking Framework with Dicopper (I) Sites and Adjacent Proton Relays for Electroreduction of CO_2 to C2+ Products. *J. Am. Chem. Soc.* **2022**, *144*, 13319–13326. [CrossRef]
178. Zhang, Y.; Zhou, Q.; Qiu, Z.F.; Zhang, X.Y.; Chen, J.Q.; Zhao, Y.; Gong, F.; Sun, W.Y. Tailoring Coordination Microenvironment of Cu (I) in Metal–Organic Frameworks for Enhancing Electroreduction of CO_2 to CH_4. *Adv. Funct. Mater.* **2022**, *32*, 2203677. [CrossRef]
179. Cui, J.-W.; Yang, J.-H.; Sun, J.-K. Organic cage-based frameworks: From synthesis to applications. *Chem. Synth.* **2024**, *4*, 30. [CrossRef]
180. Chen, J.; Abazari, R.; Adegoke, K.A.; Maxakato, N.W.; Bello, O.S.; Tahir, M.; Tasleem, S.; Sanati, S.; Kirillov, A.M.; Zhou, Y. Metal–organic frameworks and derived materials as photocatalysts for water splitting and carbon dioxide reduction. *Coord. Chem. Rev.* **2022**, *469*, 214664. [CrossRef]
181. Huang, J.-M.; Zhang, X.-D.; Huang, J.-Y.; Zheng, D.-S.; Xu, M.; Gu, Z.-Y. MOF-based materials for electrochemical reduction of carbon dioxide. *Coord. Chem. Rev.* **2023**, *494*, 215333. [CrossRef]